Analysis and Performance of Adhesively Bonded Crush Tube Structures

by

Luis Fernando Trimiño Rincon

A thesis
presented to the University of Waterloo
in fulfillment of the
thesis requirement for the degree of
Master of Applied Science
in
Mechanical Engineering

Waterloo, Ontario, Canada, 2012

AUTHOR'S DECLARATION

I hereby declare that I am the sole author of this thesis. This is a true copy of the thesis, including any required final revisions, as accepted by my examiners.

I understand that my thesis may be made electronically available to the public.

Abstract

Lighter structural and energy absorbing materials are essential to increase fuel efficiency in transportation systems and have provided a motivation to investigate the use of new joining techniques based on the use of high strength and high tenacity adhesives. Current joining techniques, such as spot-welding, limit the possible weight reduction that can be achieved if lighter sections, dissimilar materials and/or novel geometries were to be used. Adhesive materials can address many limitations of current joining techniques.

To take advantage of the available numerical codes for the simulation of bonded structures during dynamic crash events, a constitutive model for structural adhesive material using cohesive elements was assembled from the measured properties of two structural adhesives; DP-460NS and EC-2214 (3M, Canada). To verify that the proposed cohesive model accurately describes the behavior of the materials a two stage approach was used. First, a cohesive element formulation of the adhesive material was implemented to investigate a Double Cantilever Beam (DCB) (ASTM test D3433-99). The results of the simulation were compared against available experimental data. Second, using sub-size crush tube structures assembled from steel sections that were adhesively bonded, quasi-static and impact events were performed. The results from the experiment were compared against the numerical simulation of the same structure using cohesive elements to describe the adhesive joint. Later, Tie-Breaks were implemented to reduce computational times. Both types of elements successfully represented the adhesive joint and the numerical model of the crush tube was in good agreement with the overall load-displacement behavior of the experimental crush tubes.

The use and testing of sub-size structures not only permitted the validation of the numerical models; it also investigated the feasibility of adhesive-only joints in automotive structures that may be exposed to crash scenarios. Sub-sized tubes were used due to equipment capacity limits, but an analysis was undertaken to demonstrate appropriate structural scaling. Even though the results between the experiments and the simulations were in very good agreement, it is clear that current cohesive material models and Tie-Breaks cannot incorporate strain rate effects, which may be important under dynamic impact conditions. Although testing in the literature has reported that the mechanical properties of the bond are affected by the properties of the joined materials as well as the geometry of the joint, these effects in the case of crush tube structures seem perhaps negligible in view of the simulation results.

Acknowledgements

The author wishes to acknowledge the important collaboration of various people involved in this work:

Juan Camilo Isaza and Elianna Nossa-Isaza, for encouraging me to go back to an academic environment.

Chris Campbell and Mary Caruso at 3M.

Waterloo University laboratory and Machine shop personnel, without the help of skilful technicians, research and engineering would be quite a titanic task. Thanks to Richard Gordon, Tom Gawel, Norval Wilhelm, Andy Barber and Jeff Wemp.

Phil Lockhart, Chris Tom, Jason Fice and Brock Watson, who helped me, navigate the intricacies and very frustrating idiosyncrasies of LS-DYNA.

Professor Michael Worswick, for trusting that we would not make a pile of rubble out of the drop tower.

And lastly Professor Duane Cronin, who not only gave me the opportunity to join this research project but also helped expand my view of how science can be applied to the engineering profession.

This work would have not been possible without the generous funding of 3M and the Ontario Centers of Excellence (OCE)

Dedication

This work is dedicated to my mother and sister, two very brave women that have succeed in going through life with the responsibility of raising children on their own.……..

Table of Contents

List of Tables

List of Figures

Figures Appendix A

Figures Appendix B

Figures Appendix C

List of Equations

Nomenclature

A	Area of the cross section
A_{TSLC}	Area under Traction Separation Load Curve
C	Width dimension of a square cross section
C_{JC}	Coefficient Johnson-Cook equation
D	Coefficient Cowper-Symonds equation
E	Young's modulus of elasticity
E_s	Secant modulus of a material
E_t	Tangent modulus of a material
F	Force per unit of width
G	Shear modulus of a material
G	Mass during impact
G_{IC}	Energy release rate in mode I
H	Half-length of a folding element
I	Second moment of inertia for the cross section of a member
K_{IC}	Fracture toughness in mode I
L	Characteristic length
L	Perimeter length of the specimen cross' section
P	Axial load
P_m	Mean force
P_{md}	Mean force during a dynamic event
T	Traction force
T^*	Homologous temperature

V	Velocity
V_0	Impact velocity
b	Radius of the toroidal shell element in a folding element
m	Exponent in Johnson-Cook equation
q	Exponent in Cowper-Symonds equation
t	Thickness of the material
β	Scale factor
β_{VO}	Scale factor for impact velocity
δ	Displacement
ε	Strain
$\dot{\varepsilon}$	Strain rate
σ	Stress
σ_o,	Flow stress of material, is define as $\frac{\sigma_{y+}\sigma_{UTS}}{2}$
σ_y	Yield strength of material
σ_{UTS}	Ultimate strength of material
σ^D	Dynamic stress at specified strain rate (Cowper-Symonds equation)
σ^*	Normal Stress in an adhesive layer
τ_a	Shear stress in an adhesive layer
ν	Poisson's ratio

Chapter 1
Introduction

Innovation in the transportation industry is primarily driven by ever increasing requirements for improved fuel efficiency and safety standards, requiring vehicle manufacturers to incorporate light weight materials into their structural components and explore new joining methods to hold them together. Light weight structural and energy absorbing materials are essential to achieve these goals in transportation systems and have stimulated research on the use of new joining techniques based on high strength and high tenacity adhesives. Adhesive technologies are not new to human endeavors but modern adhesives were not developed until the aircraft industry sought alternatives for weight reduction. An early example is the WWII de Havilland DH.98 Mosquito airplane. War era metal shortages forced the Mosquito manufacturers to explore alternative material options; this airplane was built out of wood, and adhesives were used to bond some of its components. First using Casein resin and later "Aerolite", a more durable synthetic urea-formaldehyde compound.

Over time, adhesive technologies were introduced to the automotive industry where they first appeared in race cars (circa 1970's). Vehicle weight reduction enhances speed, handling, and braking; all key factors to success in this very competitive environment and hence the natural adoption of adhesives to improve performance. Since then, adhesives have been incorporated into street production exotic cars, like the Lotus Elise (Figure 1). The Lotus chassis included aluminum components that were bonded and riveted together to obtain substantial weight savings [25]. Unfortunately costs have been a deterrent for the introduction of this technology, at least in the level use in Lotus Elise, in main stream vehicle fleets.

Figure 1: Lotus Elise final production vehicle [6] **and chassis** [12]

The interest paid to adhesives stems primarily from the strength and stiffness that bonded structures can offer, in addition to improved weight savings. Added benefits can also be realized through enhanced corrosion protection, sealing of the body, and the ability to produce multi-material assemblies. Current joining techniques, such as spot-welding, do limit the total weight reduction that can be achieved. It does not allow for the use of lighter sections, dissimilar materials and/or novel geometries therefore reducing the available design options for more efficient next generation main stream vehicles. Adhesive materials can address many of the limitations of current joining techniques.

Several researchers [7, 16, 28, 37, 40] have investigated adhesively bonded structures for automotive applications. For example, adhesives have been used to bond energy absorbing structures for crash energy management, such as crush tubes and s-rails (Figure 2). These studies demonstrated limited success; the primary limitations being the weakness of the adhesives and the need to include self-piercing rivets to augment the adhesive strength against debonding in some cases, and in others early failure of the adhesive under dynamic loading conditions. Besides these early problems; the testing of such structures in the expected range of strain rates for automotive crash scenarios is also challenging:

1) Testing actual representative structures in automotive crash scenarios requires equipment that can deliver high speeds, in the order of 15 m/s, during the impact
2) The iterative testing required to obtain some degree of statistical confidence in the experiment could be economically prohibitive if one to one (1:1) scale prototype samples are used.

As an alternative to the use of expensive experimental equipment that can mimic dynamic impact conditions, numerical simulation has emerged as a solution that can replace the more expensive process of assembly and subsequently destruct prototype samples during testing.

Figure 2: Energy absorption components in automotive structures [38]

Explicit numerical modeling has evolved into a resourceful tool to understand and predict the response of different physical phenomena during dynamic events. As such, it is an invaluable tool for the design engineer, especially in the automotive field where there is dire need to accurately predict, with tight time constrains, the response of a given design or component subjected to a crash scenario. To address this need, numerical modeling techniques that can be used to design and evaluate adhesive joints in energy absorbing structures were investigated.

As was just mention, one essential aspect for the automotive sector is the time required to complete a numerical solution for a given scenario; the computer model needs to be economical and fast. Traditionally, solid elements pair with the appropriate constitutive model are used to accurately describe components and its material properties. However, this approach is prohibitive in terms of simulation time and computer resources. A number of schemes have been developed to mimic the behavior of materials and at the same time improve both time and computational efficiencies. The present study explored the feasibility of Tie-breaks and cohesive elements to maintain the accuracy of the model under tight computational constraints to represent adhesive joints.

A significant challenge is the limited information available to assemble constitutive models for structural adhesive materials. Available information typically comprises either general mechanical properties (e.g. Modulus of elasticity, yield stress and density) or the behavior of particular joint configurations (e.g. T-peel, T -joint, etc); this information may not be sufficient for reliable damage models of adhesive materials. In order to obtain accurate material information and to define material parameters for numerical simulations using cohesive elements and Tie-Breaks, the present study

addressed the characterization of two structural adhesives, DP-460NS and EC-2214 (3M, Canada), using results from mechanical testing across a range of different strain rates.

A two stage approach was undertaken to verify that the proposed numerical representation of the adhesive accurately described the behavior of the materials. First, each adhesive material was implemented either as a layer of cohesive elements or as Tie-breaks in a Double Cantilever Beam (DCB) simulation (ASTM test D3433-99), which is the standard test method for fracture strength in cleavage of adhesives in bonded metal joints. The results of the simulation were then compared against experimental data produced by the manufacturer of the adhesive material. Second, sub-size adhesively bonded steel crush tube structures were assembled and experimentally tested under quasi-static and dynamic impact conditions. The experimental results were compared against numerical simulations of the same event, which incorporated the numerical representations pointed above to describe the adhesive joint.

The use and testing of sub-size structures not only permitted the validation of the numerical models; it also investigated the feasibility of adhesive-only joints in automotive structures that may be exposed to crash scenarios. Sub-sized tubes were used due to equipment capacity limits, but an analysis was undertaken to demonstrate appropriate structural scaling.

Chapter 2
Background

For this work, the crush behavior of adhesively bonded structural members was investigated under quasi-static and dynamic load conditions. In this chapter, the theory that describes the physical behavior of structures under axial compressive loads is explained. The representation of adhesive materials in numerical codes is also discussed, including a brief explanation of cohesive elements and Tie-breaks as well as a brief introduction to adhesive materials. Finally, the mechanical properties of the adhesives materials used to assemble representative crush tube samples during this work are presented.

2.1 Crush tubes

Modern vehicle structures comprise a series of components that work together to absorb energy and protect occupants in the event of impact [31]. As can be seen in Figure 3, crush tubes are critically important structural members of the frontal crumple zones of cars and other vehicles such as trains, whose sole function is to dissipate energy by plastic axial deformation in a controlled manner during an impact

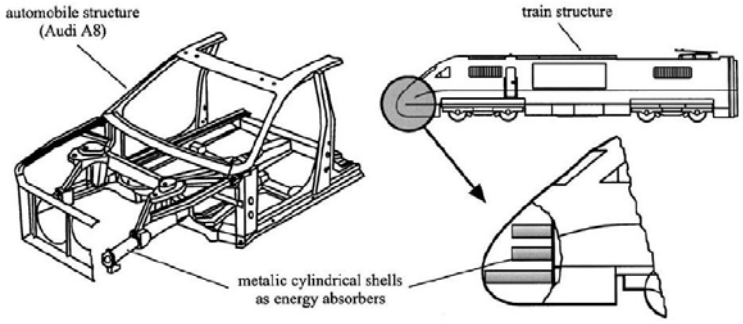

Figure 3: Energy absorption structures in modern vehicles [38]

There are two main modes of deformation typically experienced by axially loaded structures such as the crush tubes, buckling and folding (Figure 4). As explained by Prasad [38] in regards to the requirements for performance of energy absorbing structures in automotive applications:" Provided that the stability of the crush process (folding) is maintained during the event and that the structure does not deviate into a bending mode (buckling), crush tubes are the most appropriate candidates for this task due to the packaging constraints and lightweight requirements present in the modern

automobile". Therefore to understand the behavior of a crush tube, it is important to grasp the basic theory that describes the mechanics of deformation for axially loaded members, both deformation modes are discussed in more detail.

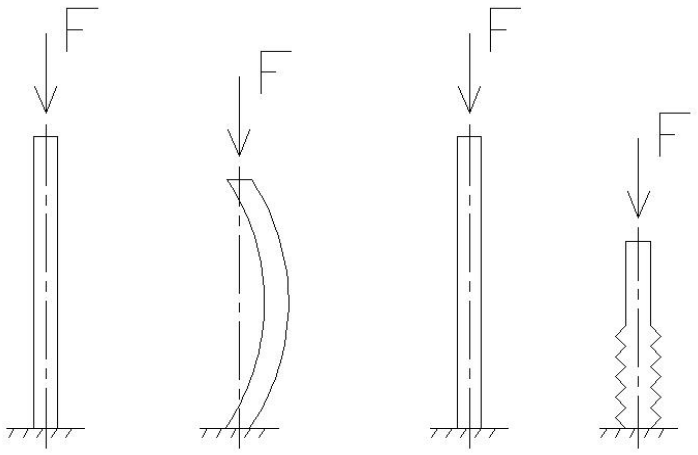

Figure 4: Buckling (left) and folding behavior (right) in axially loaded columns

2.1.1 Euler Buckling

When a structure is axially loaded, depending on its cross section characteristics and material properties; there is a limiting load that will cause the structure to globally buckle (Figure 4, left side). Buckling can be seen then as the point where the structure bends out of shape and fails by excessive deformation as the central axis goes out of plane and a hinge mechanism develops at some point depending on the bracing conditions. Buckling behavior is well described by the classic column theory developed by Euler [26] for long columns. Equation 1, below, describes the critical load at the onset of buckling for a column of length L, cross section with second moment of inertia I, and made of a material with an elasticity modulus E. The deformation mode is defined by boundary conditions and it is described by the parameter n in the equation.

$$\boldsymbol{P_{crit} = (\frac{n\,\pi}{L})^2 E\,I}$$

Equation 1: Euler critical axial load

In terms of energy absorption, Euler buckling is a poor mechanism for this task. During buckling the structure can only absorb energy through bending and through the plastic deformation of the material

wherever a hinge point is developed. Hinge development is highly dependent on the un-braced length and geometry of the structure.

2.1.2 Local buckling (Folding)

Folding is a plastic behavior in which the lateral inertia forces of the cross section are strong enough to prevent any global bending deformation. This is typical of short; stocky sections. The local deformation experienced during the crushing process can be described as a progressive folding type of collapse, resulting in a complicated pattern of folds and wrinkles which is ideal for energy absorption through plastic deformation. This collapse process effectively isolates damage to a narrow region of the column, while the rest of the structure undergoes a rigid body motion. Typically this process is described with the aid of plate theory, since plates can be used at small scale to describe a portion of the cross section of the member.

From a practical point of view, the initiation of folding can be defined by the crushing strength of the section, as presented in Equation 2. The critical load is defined by the cross section area of the member A and the yield stress of the material σ_y.

$$\boldsymbol{P_{crush} = A\,\sigma_y}$$

Equation 2: Crush load for a cross section

Although Equation 2 is very simple, it is an over simplification if one wants to describe the local buckling process. Wierzbicki [45] provided a very good local level description of the mechanics of this process; by considering that the deformation can be described by a basic folding mechanism. Figure 5 shows the folding of a sheet metal structure, consisting initially of planar surfaces and made out of a rigid-perfectly plastic material.

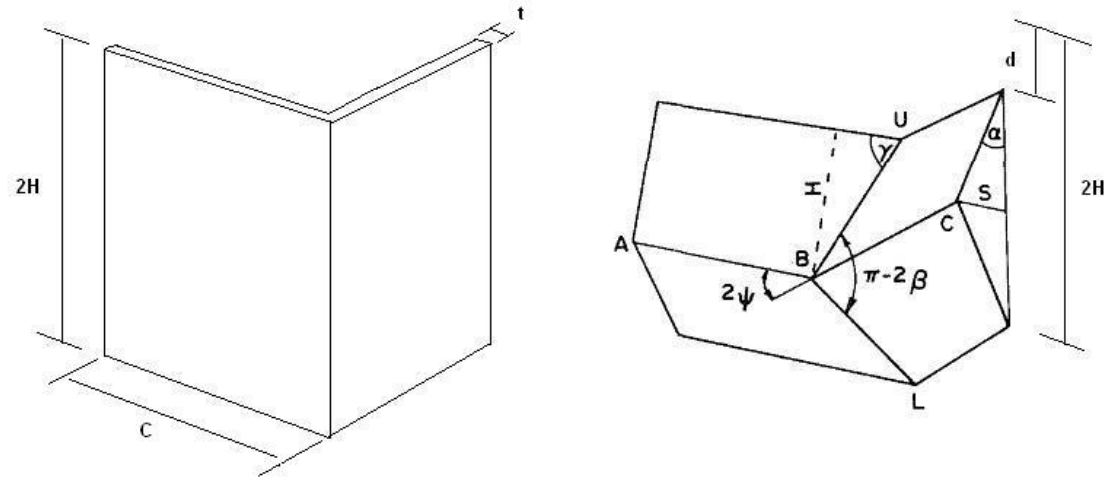

Figure 5: Basic folding mechanism [45]

By assuming that the local buckling wave of length 2H remains constant during the formation of each fold, one can describe the motion of the element by the relative velocities of the upper and lower edges. Then, by equating the rate of energy dissipation during the crushing process between the internal strain field and the rate of external work one can find an expression for the applied force during the process. For a square section of cross section dimension C, wall thickness t and made out of a material with flow stress σ_o, the mean force during the crushing process can be calculated from Equation 3. The derivation detail is presented in [45].

$$P_m = 9.56\ \sigma_o t^{5/3} C^{1/3}$$

Equation 3: Mean force for crushing in a square section

Experimental data has shown that there are different modes of collapse, as explained by Abramowicz [4]. For example, collapse (Figure 6) can be symmetric, asymmetric with modes A or B, or extensional. Variations of the formula presented in Equation 3 can be used to describe the average force in each process. It is important to note that the work presented by this author is not limited to square or round sections, it can be generalized to other types of geometries.

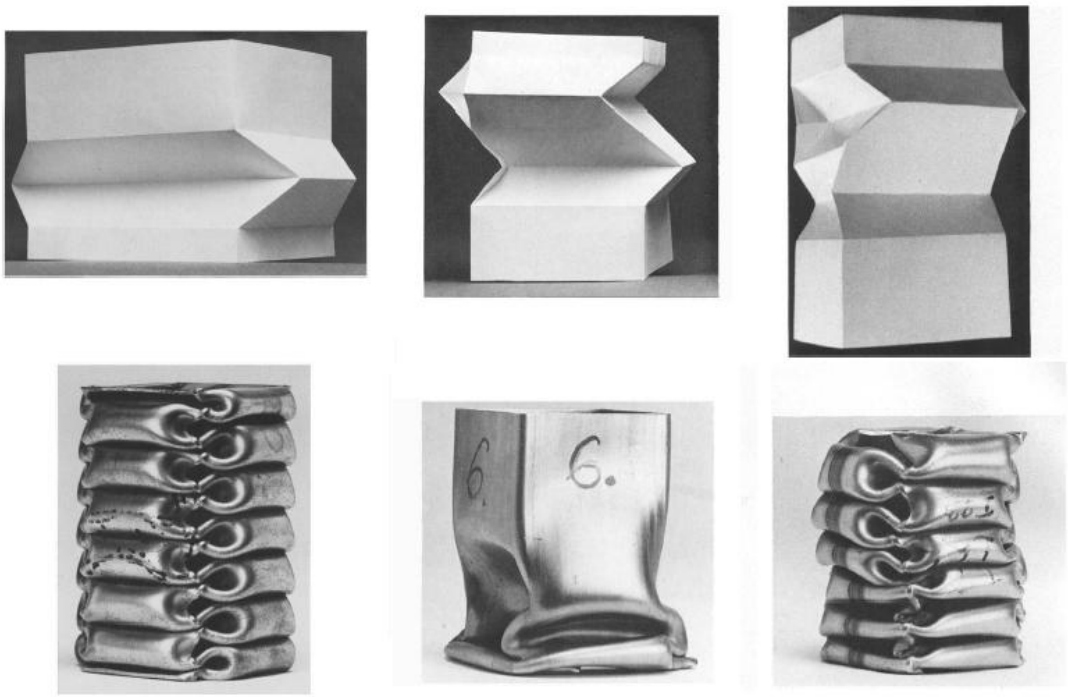

Figure 6: Collapse modes; Symmetric (left), asymmetric mode A (center), asymmetric mode B (right) [4]

2.1.3 Transition from global buckling to folding

Understanding the factors that determine whether global buckling or folding will occur as well as the transition point between the two behaviors; is critical for the proper design of structural members intended to safely absorb energy during impact scenarios. Consider a crash event were a bending mechanism (Euler buckling) is triggered, in this case the energy absorption of the structure would be seriously compromised, endangering occupant safety.

As described by Abramowicz [3], both behaviors, buckling and folding, are completely defined by the geometry of the section, its length and the material it is made from. This is not surprising if one considers that both the Euler column and the crush load formulas for the axial capacity of a section are solely dependent on these parameters. For a thin-walled square tube of width C, wall thickness t, length L and made out of a material with tangent modulus E_t and secant modulus E_s. Abramovicz developed the following equation to describe the transition between global buckling and local folding:

$$\left(\frac{L}{C}\right)_{crit} = \sqrt{\frac{6\,E_t/E_s}{2+\sqrt{1+3\,E_t/E_s}}}\left(\frac{C}{t}\right)$$

$$E_t = d\sigma/d\varepsilon$$

$$E_s = \sigma/\varepsilon$$

Equation 4: Transition between global buckling and local folding in square sections

It is clear that the transition is highly dependent on the geometric dimensions of the column as well as the material it is made from. Abramovicz mapped the transition from global bending to progressive folding (Figure 7) for square and circular columns under axial loads. From this figure it is clear that the aspect ratio (L/C or L/2R) and the relationship between the cross section and its thickness (C/t or 2R/t) define if a crush tube will bend or progressive fold during a crushing event.

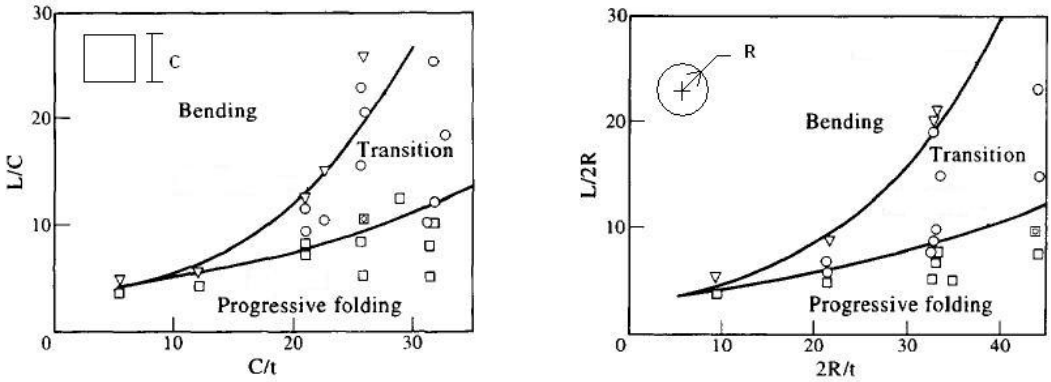

The deformation map for columns subjected to dynamic axial loading. Experimental results: □—progressive collapse; ○—transition from progressive collapse to global bending; and ▽—global bending.

Figure 7: **Deformation maps of axially loaded columns** [3]

2.1.4 Dynamic loading effects

To this point, discussion has been restricted to structures under the assumption that they are subjected to quasi-static loading conditions, where the rates of change in the loads and inertia effects are negligible; however, the scenarios that we are interested in are better described by dynamic conditions. Under dynamic conditions both the loading rate and inertial effects can affect the

observed behavior of a material or structure. As was well explain by Goldsmith: “It has been long recognized that the mechanical behavior of materials under conditions of rapid loading and impact differs significantly from that under static load application” [17]. This behavior is clearly illustrated in Figure 8 for steel materials.

In light of this marked difference in behavior, it is important to characterize the mechanical properties of materials subjected to dynamic loads. A load is defined as “static” or “dynamic” depending on the velocity used to apply it. In general terms, this is characterized by the strain rate, as defined in Equation 5.

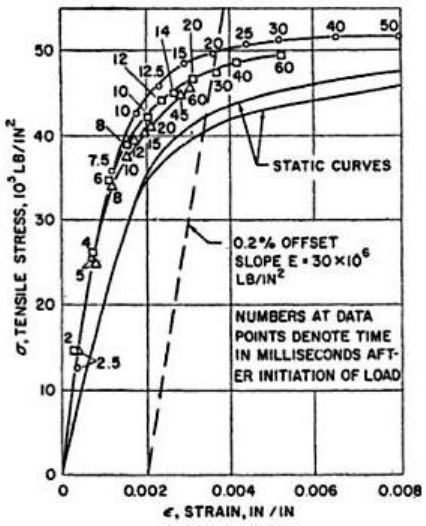

Static and Dynamic Stress–Strain Curves for Type 302 Stainless Steel, as Received [77]

Figure 8: Dynamic curves obtained by rapid loading [17]

$$\dot{\varepsilon} = \frac{d\varepsilon}{dt}$$

Equation 5: Strain rate definition

A common practice is to define the strain rate in terms of the applied velocity and divide it by a characteristic length (Equation 6). This expression only provides an average value for the structure or component and cannot predict local strain rates, which could be higher.

$$\dot{\varepsilon} = \frac{V}{L}$$

Equation 6: Strain rate, practical definition

In general, there are three regions in the spectrum of strain rates: First, the quasi-static region with strain rates in the order of 0.1 1/s or less, typical of most civil structures. The second region; where strain rates are in the realm of 100 1/s, includes forming operations and vehicular impact events; and third region with values exceeding 1000 1 /s, which is not uncommon with high velocity projectiles and explosive detonations [2].

Several approaches can be found in the literature to describe the effects of strain rate on material mechanical properties; however, two of the most commonly material models used to describe the dynamic effects for metals follow.

2.1.4.1 The Cowper-Symonds constitutive model

The Cowper-Symonds equation (Equation 7) is one of the most well known models used to describe strain rate effects on metallic materials [13]. Cowper and Symonds investigated the strain-rate effects in the impact loading of cantilever beams, and from that work derived an expression that predicted the value of the dynamic yield stress for a given strain rate as a function of strain rate and the quasi-static value of the yield stress.

$$\frac{\sigma_o^d}{\sigma_o} = 1 + (\frac{\dot{\varepsilon}}{D})^{1/q}$$

Equation 7: Cowper-Symonds equation

Where: σ_o^d is the dynamic flow stress at an effective strain rate $\dot{\varepsilon}$, σ_o is the associated flow stress at a reference strain rate and both D and q are constants that depend on the particular material. Although this equation is broadly used due to its practicality, it is important to mention that sometimes the Cowper-Symonds equation is not able to predict material behavior over a broad range of strain rates, unless its coefficients change.[5]. Generally this model is used to scale an existing curve of stress-strain or a standard incremental plasticity model.

2.1.4.2 The Johnson-Cook constitutive model

Another common model is described by the Johnson-Cook equation [20]. These authors investigated the fracture characteristics of three different metal materials over a range of strain rates and temperatures, and from that work derived the following expression:

$$\sigma = [\sigma_o + B\varepsilon^n]\left[1 + C_{JC}\ln\frac{\dot{\varepsilon}}{\dot{\varepsilon}_o}\right][1 - T^{*m}]$$

$$T^* = \frac{T - T_{room}}{T_{melt} - T_{room}}$$

Equation 8: Johnson-Cook equation

In this case, the dynamic flow stress σ is not only defined in terms of the actual strain rate $\dot{\varepsilon}$, but also by the reference strain rate, $\dot{\varepsilon}_o$, corresponding to the reference stress strain curve(σ vs. ε.) of the material. The reference stress strain curve is also used to determine the parameters B and n. This equation accounts for adiabatic temperature increases due to plastic heating which can cause material softening by introducing the term [1-T^{*m}].

2.1.5 Force vs. displacement diagrams and results analysis

Forces vs. displacement diagrams are critically important to structural component design; these diagrams convey typical output generated during experimental testing of the structures and provide valuable information for the designer. The diagram is constructed by measuring the force and the displacement of the top of the tube at a given instant during the loading of the structure (Figure 9).

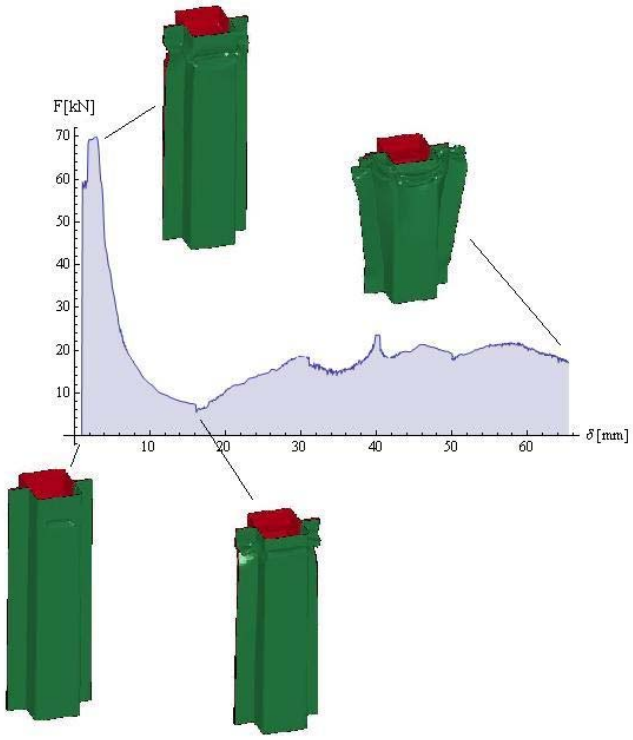

Figure 9: Force displacement diagram construction

Out of the force displacement diagram (Figure 10), the following quantities are of main interest:

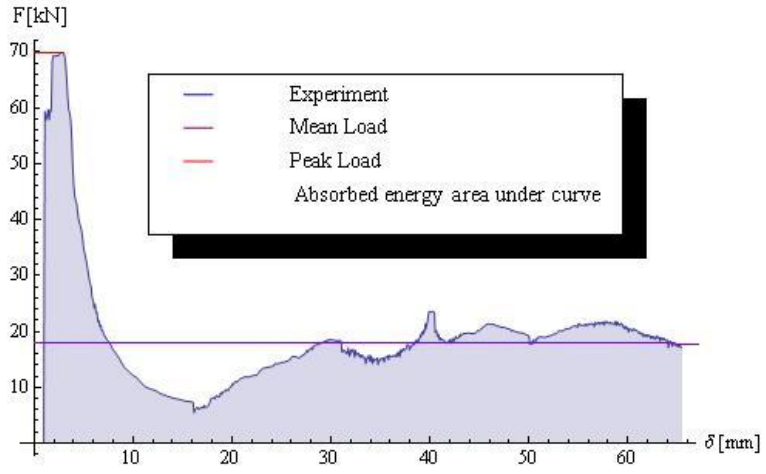

Figure 10: Crush tube force vs. displacement diagram

1. The peak load: This load determines the maximum acceleration during the event, which can be related to the forces exerted on the occupants during the crash. Obviously, it is highly desirable to minimize this force to avoid or mitigate occupant injuries. Peak loads can be mitigated by the introduction of deformations (buckle initiators) that facilitate the initiation of the deformation process.
2. Mean load: This is the average load during the deformation process. It is calculated as:

$$P_m = \frac{\int_0^{\delta} F(x)dx}{\delta}$$

3. Fold formation: Each peak in the curve defines the formation of a fold. It can be related to the distance 2H presented in section 2.1.2.
4. Absorbed energy: energy dissipated in the structure through plastic deformation. It is the area under the curve of the load-displacement diagram.
5. Specific energy: By dividing the absorbed energy by the mass of the structure one obtains the specific energy. The specific energy is typically compared against other types of structures or materials to determine which is more efficient.

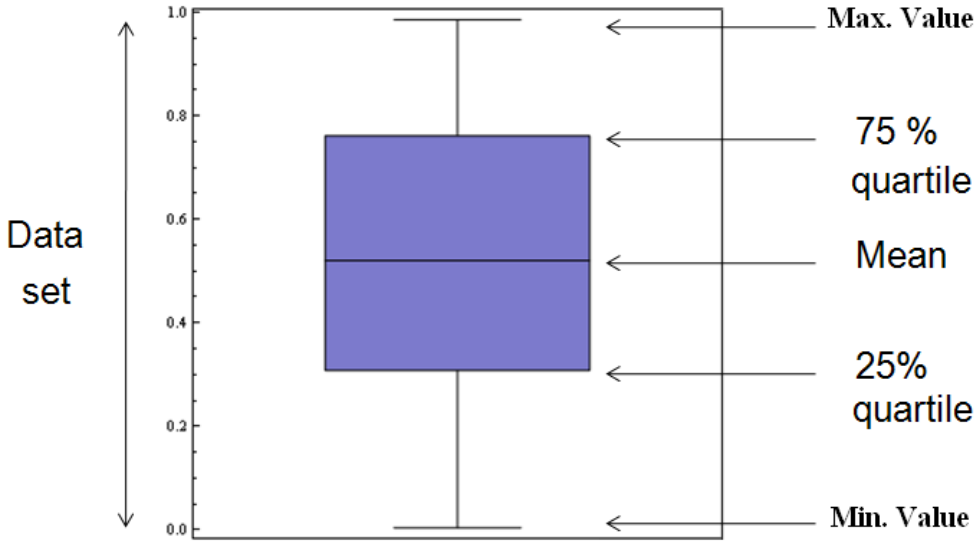

Figure 11: Whisker plot

Whisker plots are used to represent statistical information for a given set of data, representing another important tool for results analysis. A brief description is given in Figure 11. It is easier to analyze the previously mentioned quantities, e.g. specific energy, by using whisker plots than by comparing across load-displacement diagrams.

Although the graphic representation of key quantities can provide insight into structure performance, it is important to have statistical tools that can allow distinguishing if one quantity is indeed different than other when comparing results from experiments. For this purpose hypothesis testing can be used to estimate the difference between two measured mean values. A summary of the procedure consists of:

1. State a null hypothesis H_0 and alternative hypothesis H_1 which we accept if we reject H_0.
2. Set the significance level of the test.
3. Choose the test statistic.
4. Determine the statistical distribution to be use.
5. Collect a random sample and calculate the test statistic and make a decision on H_0.

Following this procedure, we can define a T value from a t-distribution, that is critical and compare against an observed T value. Depending if the observed value is less or more than the critical value, one can determine if the null hypothesis is valid or not.

2.1.6 Crushing behavior for built up sections

As manufacturers strive to reduce overall vehicle weight to comply with demands for increased fuel economy, new structural component designs that incorporate light weight and/or high strength materials are beginning to emerge. This effort not only poses a serious challenge to traditional designs that use regular members like extruded squares and round sections, it also requires new joining techniques such as high tenacity adhesive bonding to replace technologies like spot welding , which cannot be used with very thin materials or multi-material assemblies. Of special importance with the implementation of adhesives is the use of hat and channel sections to build the close sections that can be used as the strcutural components of a transportation structure.

During the following sections, the equations that describe the crushing of built up sections are introduced; it is assumed that failure in the bond or joint does not occur. In general for each equation described below, L_p defines the circumferential length of the specimen cross section. As described in Figure 12; $L_p = (2a + 2b + 4f)$. Also, as Karagiozova [23] pointed out, a much better agreement

between experimental data and the equations that define the crushing load can be reached if the flow stress is defined as:

$$\sigma_0 = \frac{\sigma_y + \sigma_{UTS}}{2}$$

Equation 9: Practical definition of flow stress

2.1.6.1 Top-hat section

A top-hat specimen consists of one section in the shape of a hat closed with a plate in the back as shown in Figure 12. For hat-shaped specimens, White [44] proposed the following equation to describe the average force during a quasi-static axial crushing event for a perfectly plastic material:

$$P_m = 32.89(\frac{L_p}{t})^{1/3}\sigma_o t^2/4$$

Equation 10: Average crushing load for top-hat sections

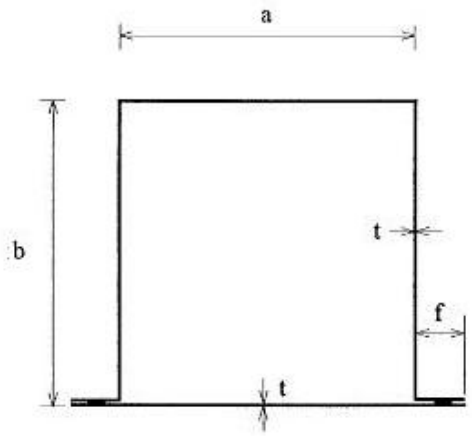

Figure 12: Top-hat geometry

In the case of a dynamic event, the previous equation can be modified by the use of the Cowper-Symonds uniaxial constitutive equation, as presented in 2.1.4.1. Then the dynamic mean crushing load for a non-strain hardening material impacted at a velocity V_o is given by:

$$P_{md} = P_m(1 + (\frac{1.33\ V_o}{L_p\ D})^{1/q})$$

Equation 11: Average crushing load for top-hat section of non-strain hardening and strain rate sensitive material

For a strain hardening and strain rate sensitive material, the equation can be written as:

$$P_{md} = P_m(1 + (\frac{0.87\ V_o}{L_p^{0.96} t^{0.04}\ D})^{1/q})$$

Equation 12: Average crushing load for top-hat section of strain hardening and strain rate sensitive material

2.1.6.2 Double hat section

In the case of double hat sections, shown in Figure 13, a similar procedure is followed by White [44].

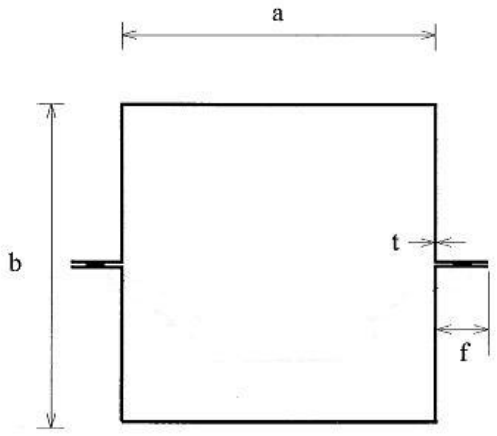

Figure 13: Double-hat section

For a perfectly plastic material under quasi-static load:

$$P_m = 52.20(\frac{L_p}{t})^{1/3}\sigma_o t^2/4$$

Equation 13: Average crushing load for double hat section under quasi-static load conditions

Once again, one can use the Cowper-Symonds relation to obtain an approximation for dynamic load cases. Hence, for a perfectly plastic material and for a strain hardening double-hat specimen the corresponding formulas are:

$$\boldsymbol{P_{md} = P_m(1 + (\frac{2.63\, V_o}{L_p\, D})^{1/q})}$$

Equation 14: Average crushing load for double hat section under dynamic conditions of non-strain hardening and strain rate sensitive material

$$\boldsymbol{P_{md} = P_m(1 + (\frac{0.973\, V_o}{L_p^{0.96} t^{0.04}\, D})^{1/q})}$$

Equation 15: Average crushing load for double hat section under dynamic conditions with strain hardening and strain rate sensitive material

2.1.6.3 Double channels section

To date, few studies have addressed the crush behavior of channel structures, as shown in Figure 14. For this structure, we assume that by using the equation derive for a closed square section we can provide a reasonable approximation of the crushing load for this geometry by using L_p= (2a + 4c) instead of the cross section dimension C of a square tube.

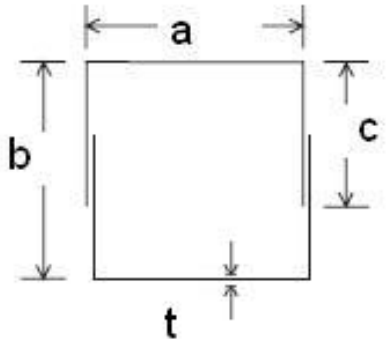

Figure 14: Double channel built-up section

For this purpose Equation 3 can be rewritten as:

$$P_m = 9.56\,\sigma_o t^{5/3} {L_p}^{1/3}$$

Equation 16: Average crushing load for double channel section

In the case of a dynamic event, we simply use the Cowper-Symonds correction as proposed by Abramowicz [4].

$$P_{md} = P_m\left(1 + \left(\frac{0.33\,V_o}{L_p D}\right)^{1/q}\right)$$

Equation 17: Average crushing load for double channel section under dynamic conditions assuming non-strain hardening and strain rate sensitive material

2.1.6.4 Transition from global buckling to folding under dynamic loading

As it can be seen in the equations presented in the previous section, the mean load for a dynamic event can be calculated by using the mean load of the quasi-static event and multiply it by a facto to account for strain rate effects. One has to suspect that the critical load that defines the type of collapse behavior is affected by strain rates too. Under this consideration, one has to reconsider the deformation maps of axially loaded structures (Figure 7). As they were originally presented by the authors, it is not clear how dynamic effects were considered. These maps need to be modified so that they clearly show the effect of the impact velocity or strain rate, which a particular cross section is subjected to during a dynamic event. It is extremely important to ensure that the proposed design for a crush tube is not in the transition region between folding and buckling, since global buckling could be catastrophic for the vehicle's occupants. New maps can easily be constructed for different cross sections by correcting for the strain rate in the equation that describes the transition zones, e.g. Equation 4 can be modified by using either the Cowper-Symonds or the Johnson-Cook equation to introduce strain rate effects.

2.2 Adhesives

The use of adhesives is of great importance in this work; therefore a very brief introduction is provided below.

An adhesive can be defined in layman terms as a substance capable of holding materials together by surface attachment. This is a simple definition for a material that can have many different chemical

compositions and uses. Adhesives are not a recent development in the history of human technology; they have evolved from substances made out of natural compounds, eggs and bones, to the modern substances we find in hardware stores and aircraft manufacturing facilities today. Over time, adhesives have taken on a broad range of functions: bonding pottery, holding the wood laminates of compound arches, furniture construction and modern aircraft structure assembly.

Although adhesives have been around for centuries, real technological advancement has only ramped up over the last 100 years with increased understanding of polymer science, more specifically the development of plastics and elastomers.

2.2.1 Adhesive types

A brief description of some common types of adhesives is presented below, extracted from History of Adhesives [1].

- **Animal glues**- are made from protein extracted from the bones and tissues of animals. The bones are heated to extract a gelatin material. The gelatin can be re-liquefied by applying heat, which gives it quick setting properties. It is primarily used in the carpentry and furniture industries.
- **Starch-** is a carbohydrate extracted from vegetable plants such as corn, rice, wheat or potatoes. A major area of application is the bonding of paper products.
- **Rubber-based solvent cements-** are adhesives made by combining one or more rubbers in a solvent. These solutions can be further modified with additives to improve the tack or stickiness, the degree of peel strength, flexibility, etc. They are used in a wide variety of applications.
- **Epoxies-** are adhesive systems made by a complex chemical reaction. Various resins are made synthetically by reacting two or more chemicals. The resultant resin can be reacted or cured by the addition of another chemical called a hardener or catalyst. The basic epoxy system can be further modified to change its physical properties by the addition of plasticizers for impact resistance and flexibility; dilutents or solvents to reduce the viscosity; fillers and reinforcements such as glass fiber, alumina, silica sand, clay, metal powders to change properties such as heat and electrical resistance, fire retarding, strength and adhesion to certain substrates and materials. Epoxy adhesives can bond a variety of substrates

(particularly metals) with high strength. They have been used to replace more traditional joining methods of joining like nuts and bolts, rivets, welding, crimping, brazing, and soldering.

- **Cyanoacrylates-** are extremely rapid curing adhesives, commonly called “superglue”. They are typically used where there is a need for rapid curing, single component adhesive that provides high adhesion, high tensile strength and easy dispensing.

Although adhesives can present a wide range of compositions, as was shown above, they can be generally treated as polymers. A polymer is a long molecule containing atoms held together by primarily covalent bonds along the molecule. Polymers can be classified into three groups:

- **Thermoplastics-**Linear or branched polymers which melt upon heating. They can be further categorized into crystalline or amorphous depending on the presence or lack of a definite structure, or regular pattern, in their molecular composition.
- **Thermosets-** are rigid, highly cross-linked polymers which degrade rather than melt when exposed to heat.
- **Rubbers-** lightly cross linked polymers which have elastomeric properties.

2.2.2 Deformation of polymers [24]

Polymers exhibit a wide range of mechanical properties depending upon their structure and the testing conditions. Polymers, as many other engineering materials, have elastic behavior, but this response is highly dependent on the structure and chemical composition of the polymeric material. In polymers with semi-crystalline structure, deformation takes place essentially through bending and stretching of aligned polymer backbone bonds, which requires high forces. In the case of some isotropic polymers, the molecules are frozen coiled and randomly oriented in the structure and so elastic deformation induces relatively easier bond rotation which requires lower forces. In general, polymers only tend to obey Hooke's law (linearity between load and displacements) at vanishingly small strains and at high strains their behavior is non-Hookean.

The behavior of many polymers can be thought of as being somewhere between that of elastic solids and viscous liquids. Polymers exhibit a distinctive mechanical behavior in the way they respond to an applied stress or strain depending upon the rate or time period of loading. Elastic materials obey Hooke's law, whereas viscous materials, such as liquids, tend to obey Newton's law where the stress

is proportional to strain-rate and independent of strain. At low temperatures and high rates of strain polymers display elastic behavior, whereas at high temperatures and low rates of strain they behave in a viscous matter. For this reason polymers are termed as viscoelastic.

In terms of deformation and failure, two very distinct phenomena can be observed in polymers, again this being highly dependent in chemical composition and structure. The first one is *Shear yielding*, also known as shear banding. This is an important mechanism that can lead to plastic deformation in polymers; it takes place essentially at constant volume and leads to a permanent change in specimen shape. The second one is *crazing.* It is possible to consider crazes as micro-cracks bridged by fibrils and their formation is accompanied by an increase in specimen volume. Multiple crazing can lead to general yielding and act as a toughening mechanism in polymers.

2.2.3 Adhesive bond analysis

There are two basic approaches to examining adhesive bonds. One criterion is based on the classical stress analysis idea: failure will occur when the maximum stress (or strain) within the material that defines the bonded joint reaches a critical value. The second major approach analyzes adhesive joints by applying fracture mechanics principles.

Although both methods have proponents and detractors, both approaches can prove useful in the understanding of engineering structures and components that include adhesively bonded joints. Both methods will be presented briefly. More details can be found in the mechanics of Adhesion [15].

2.2.3.1 Stress in bonded joints [15]

Fundamental solutions have been developed based on assumptions of uniform stress and strain. They generally are closed form solutions of differential equations and provide fundamental insights into how stress fields develop in the joint. Generally, the classical solutions consider peel and shear stresses as independent quantities. In fact, coupling between shear and normal stresses occurs in many bonded joints and this has to be considered when reviewing the results of such solutions. Two common equations use to represent stresses in adhesive joints are the shear lag model and the butt joint with stiff adherends.

When the load is transferred from one adherend to another, primarily through shear stresses within the adhesive layer (Figure 15), the shear lag model developed by Volkersen (Equation 18) is of common use to describe the stress field in the joint.

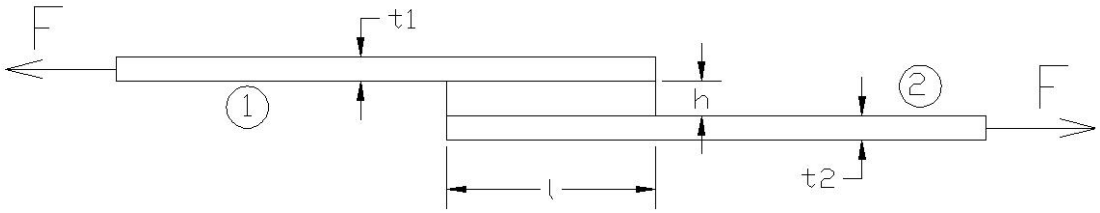

Figure 15: Lap shear joint

$$\tau_a(x) = \frac{F\omega}{2\sinh\left(\frac{\omega l}{2}\right)}\cosh(\omega x) + \frac{F\omega}{2\cosh\left(\frac{\omega l}{2}\right)}\left(\frac{E_2 t_2 - E_1 t_1}{E_2 t_2 + E_1 t_1}\right)$$

$$\omega = \sqrt{\frac{G}{h}\left(\frac{E_2 t_2 + E_1 t_1}{E_2 t_2 E_1 t_1}\right)}$$

Equation 18: Shear stress distribution lap joint

Adhesively bonded butt joints (Figure 16) are one of the simplest idealized joint geometries of practical importance, Equation 19 is used to describe the induced stress σ* in the adhesive in terms of the nominal normal stress, σ, in the joint. This is an even stress distribution across the joint and only considers the constraining effect of the adherends and does not consider stress concentrations generated by the geometry.

$$\sigma^* = \begin{cases} \nu_2\left[1 - \left(\frac{E_2\nu_1}{E_1\nu_2}\right)\right]\sigma & Plane\ stress \\ \left(\frac{\nu_2}{1-\nu_2}\right)\left[1 - \left(\frac{E_2\nu_1(1+\nu_1)}{E_1\nu_2(1+\nu_2)}\right)\right]\sigma & Plane\ strain \end{cases}$$

Equation 19: Normal stress but joint

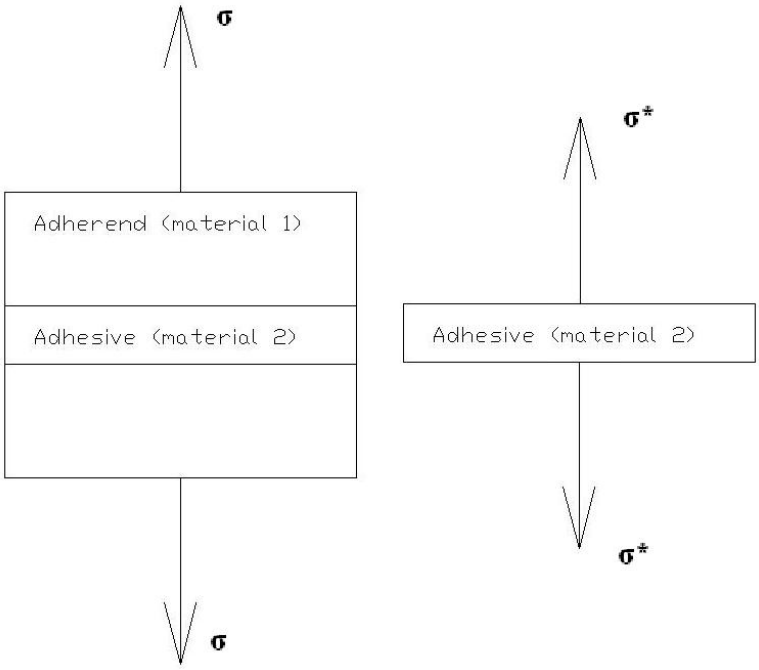

Figure 16: Butt joint

2.2.3.2 Fracture mechanics applied to adhesive bonds [15]

Fracture mechanics has been use to determine the resistance of materials to the growth of cracks, and design damage-tolerant structures. Fracture mechanics is perhaps the best example of how the fiction of stresses at a singularity can be acknowledged, while still providing a framework for a quantitative measure of the severity of cracks.

Several different criteria can be used to understand crack propagation, but the following two seem particularly appropriate to be use with adhesives:

- The stress intensity approach provides a measure of the severity of the stresses in front of a crack or de-bond tip.
- The strain energy release rate provides an intuitively meaningful measure of the energy required to de-bond a unit area of the propagating crack.

Bonded systems are quite rich in their array of potential fracture mechanisms (Figure 17). There can be cohesive cracks that grow entirely within the adhesive layer or a crack can also grow along an

interface to create adhesive fracture. Cracks may branch into substrates or oscillate within the adhesive layer. It is important to clearly define what a crack is, in an adhesive bond:

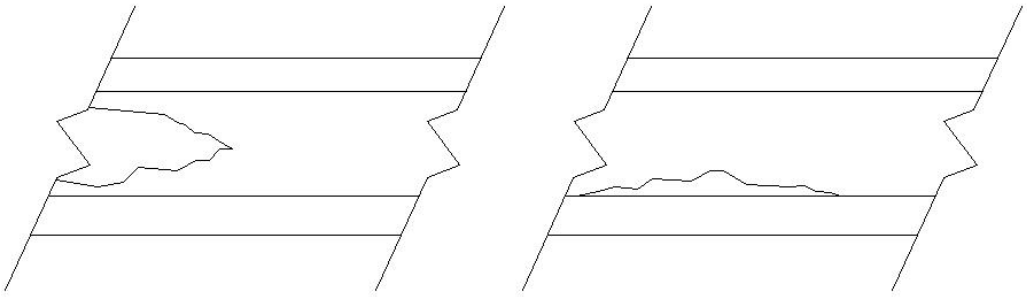

Figure 17: Failure modes in adhesives: Cohesive crack (left) and adhesive crack (right)

- **Cohesive cracks-** cracks are considered to be cohesive when they grow entirely within the adhesive layer. They may also be considered to be cohesive if the adherends are the same and *the adhesive layer is being ignored in the analysis.* This assumption is valid when the bond between the adhesive and adherend is performing well. Cohesive cracking is generally regarded as mode I failure (Figure 18).

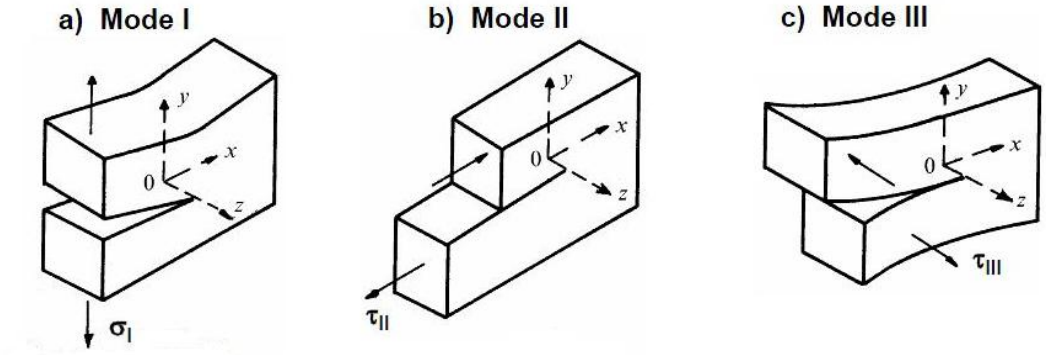

Figure 18: Failure modes in fracture mechanics

- **Adhesive cracking-** cracks run along the interface between the adherend and the adhesive due to interactions between the stress field in the adhesive layer and spatial variations in fracture properties. The cracks are not generally free to evolve as mode I cracks, as was the case for cohesive cracks, and mixed-mode fracture concepts (combinations of tension and shear) have to be considered. Mode II or shear components are induced, even in what appear to be nominally mode I loadings, due to differences in module about the interface. Again, if the presence of the adhesive layer is being ignored and the adherends are dissimilar, then a crack appears to be adhesive (i.e. an adhesion failure) on the macroscopic scale.

2.3 Material properties

Two epoxy adhesive materials (manufactured by 3M) were selected to determine the suitability of adhesive system to be use for the manufacturing of structures subjected to impact loads. The two adhesive materials selected for this study were EC-2214 and DP-460NS. The first material, EC-2214, can be described as a one part epoxy material with high strength and low ductility, while DP-460NS is a two-part epoxy material with high tenacity and high deformation at failure. The measured mechanical properties of the adhesives used are summarized in Table 1.

Mechanical Property	EC-2214	DP-460NS
E [GPa]	5.1	2.2
Poisson Ratio ν	0.38	0.41
Yield Stress [MPa]	52	36
Ultimate Stress [MPa]	72	37.7
Strain to failure	0.061	0.108
Density [kg/m^3]	1545	1200

Table 1: Adhesive mechanical properties of EC-2214 and DP-460NS

Due to the nature of the event that wants to be represented; additional information is required to build the appropriate material model that can accurately describe the adhesive. For this purpose a series of different mechanical tests, uniaxial universal tension and lap shear test using thick steel adherents

were performed at different strain rates by personnel at University of Waterloo. Graphical results from the experimental testing are presented later.

2.3.1 Tensile testing

Tensile testing of the material was performed using an Instron machine for the low strain rates, below 7.7 x 10^{-1} 1/s. Testing at higher strain rates was done using an electromagnetic rig developed at the University of Waterloo; results are provided in Figure 19.

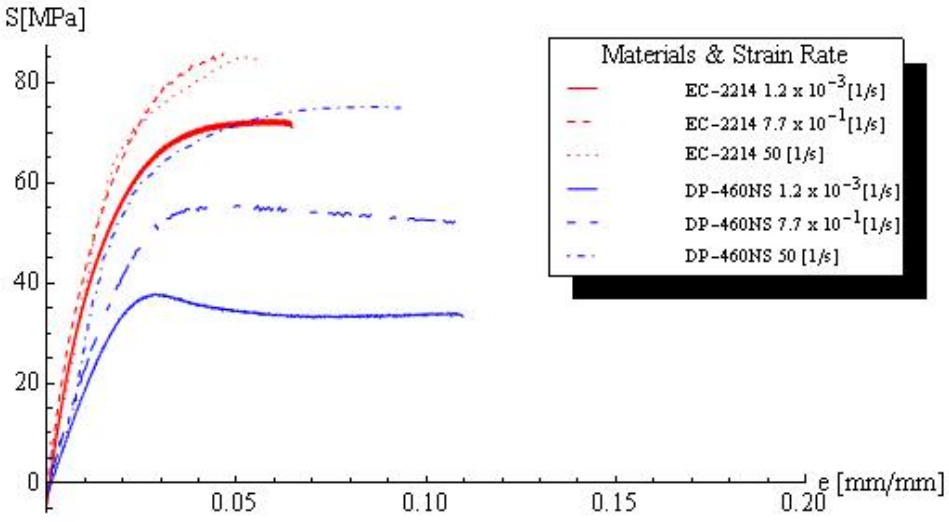

Figure 19: Tensile testing of adhesive materials EC-2214 and DP-460NS

2.3.2 Lap shear testing

Lap shear testing of the materials was performed in accordance with ASTM D1002-05, the standard test method for apparent shear strength of single-lap joint adhesively bonded metal specimens by tension loading. The tests consist of two steel rectangular pieces joined by the adhesive and then subjected to tension in such a way that the adhesive will undergo shear. The measured properties can vary depending on the nature of the adherends, a good example of this behavior and experimental data is provided by [39]. Results presented in the graphics (Figure 20 and Figure 21) are only valid for steel on steel joints.

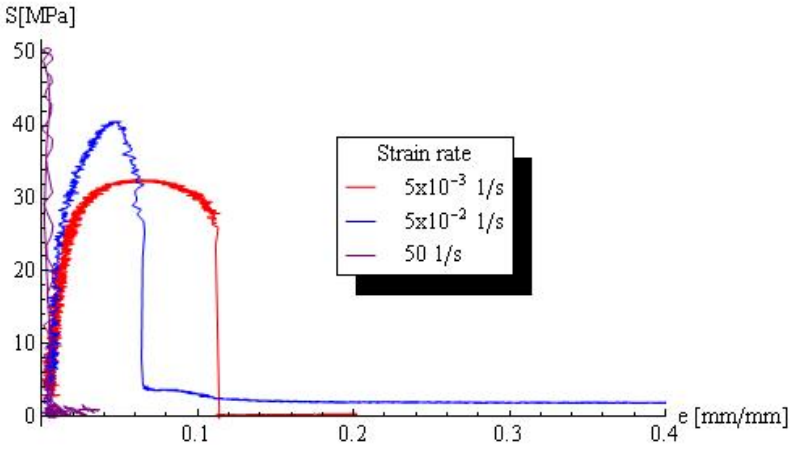

Figure 20: Lap shear test of steel on steel specimens bonded with EC-2214

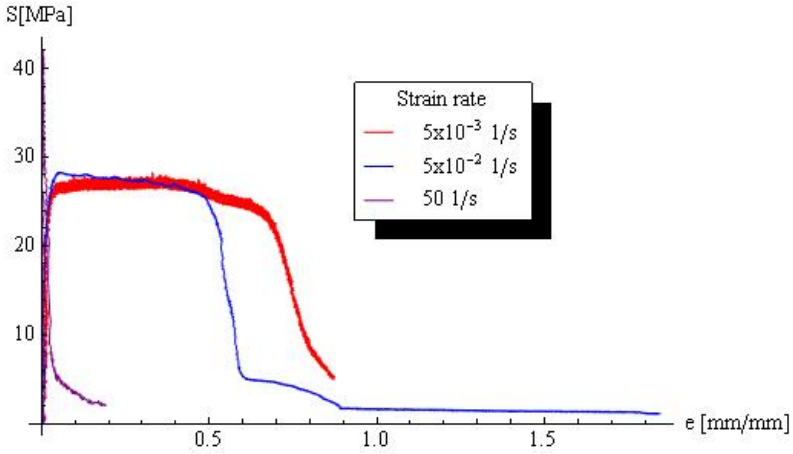

Figure 21: Lap shear test of steel on steel specimens bonded with DP-460NS

2.3.3 Strain rate effects

One of the main factors affecting the strength of any material is the loading rate. Figure 22 illustrates the effects of strain rate on the ultimate strength of EC-2214 and DP-460NS.

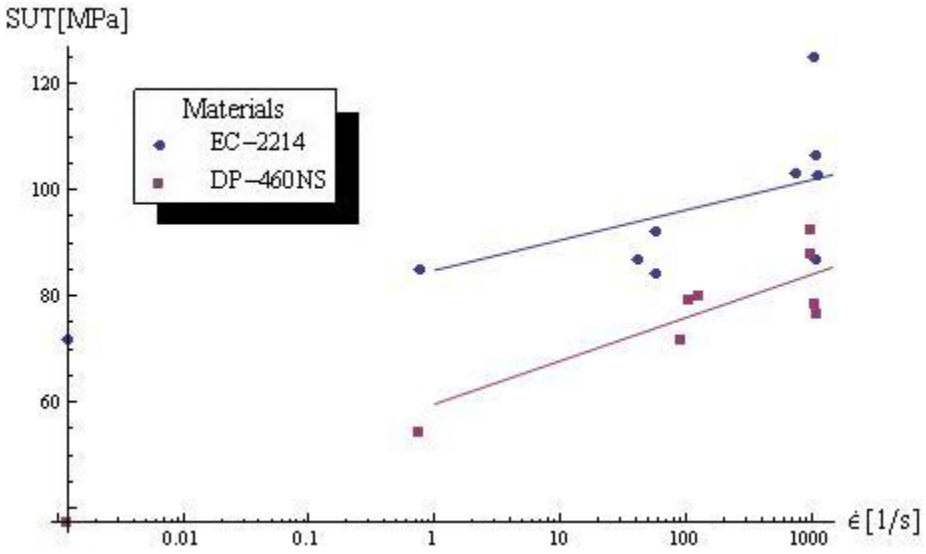

Figure 22: Strain rate effects on adhesive materials EC-2214 and DP-460NS

Generally the effects of strain rates are depicted in terms of the yield stress, in the case of these two materials due to measuring artifacts, it was quite difficult to pinpoint this value accurately in the experimental data gathered by personnel at University of Waterloo. For generality, the strain rate effects were shown in terms of ultimate stress to demonstrate the existence of dynamic effects.

2.4 Numerical representation of joints

One essential aspect for the automotive sector is to understand the behavior of bonded joints subjected to very large impact deformations; this is critical to assemble safe and reliable structural members for the next generation of light weight vehicles. Computer models using explicit finite element analysis are invaluable to this effort, providing manufacturers with fast and cost efficient ways to verify safety requirements in the early stages of design. However, a computer model is only reliable if it can soundly replicate the physical principles involved in the problem. This requires that both the geometry and the material models used to describe the mechanical behavior of the materials involve are accurate, and that the details that describe the event can be replicated by means of numerical simulation.

Traditionally, one could use a series of solid elements to accurately describe the adhesive mechanical behavior. However, this approach is prohibitively expensive in terms of simulation time and computer resources. Many schemes have been developed to mimic material response while at the same time providing reduced solution time and computational efficiencies.

Cohesive elements and Tie-Breaks are two such elements which can be implemented to emulate the behavior of adhesive joints with minimal computational demands.

2.4.1 Cohesive elements

Cohesive elements have emerged as a more sophisticated implementation to overcome the limitations of Tie-Breaks, which are springs joining two nodes in two different surfaces. A more detailed explanation of Tie-Breaks can be found in the following section (2.4.2). Cohesive elements can be described as a series of springs joining two surfaces; three springs are included, one normal and two in the shear directions (Figure 23). Cohesive elements are implemented by defining an element between the joined surfaces and then assigning a material model to it. The material definition requires properties that are dependent on the fracture behavior of the material.

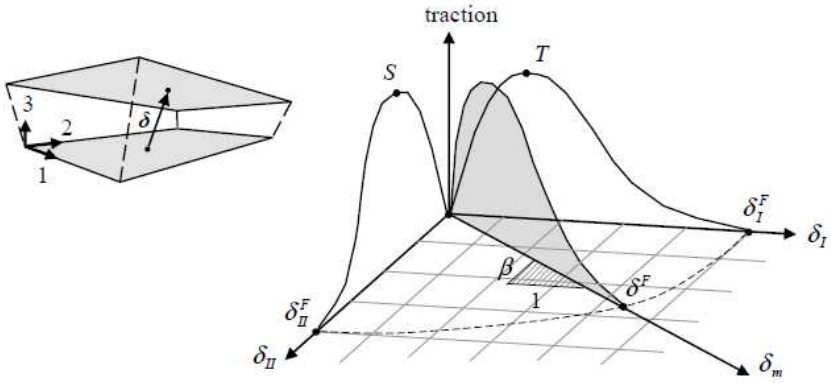

Figure 23: Cohesive element [29]

Specifically, the fracture toughness or energy release rate is required, in addition to a damage curve that defines both traction and displacement. This is a very important difference from the Tie-Break method. The use of an element permits designers to link the energy absorbed during deformation with the volume of the material, which is directly linked with fracture mechanics principles. Also, using a damage curve links the displacements with the initiation of damage in the material.

The cohesive element implementation is based on the work of Tvergaard and Hutchinson [43]. It is important to note that although cohesive elements represent a great advance over the Tie-Break; this method still does not completely capture the physical behavior of the joint. If we come back to the crack propagation problem and look at the crack front, the first element is not capturing the stress concentration that must be present due to the presence of the crack itself which is a major feature of

fracture mechanics that is still missing. Another limitation is the exclusion of strain rate effects in the formulation.

2.4.2 The Tie-Break contact definition

A Tie-Break element can be best described as a spring joining two nodes, where each node belongs to a different body (Figure 24). The Tie-Break constrains how the bodies move relative to each other, and the mechanical response of the Tie-Break can be implemented in several different ways depending on the capabilities of the software. In the case of the explicit finite element code LS-DYNA LSTC, the following characteristics are available:

1. Failure as a function of normal or shear components or a combination of both
2. Stress is limited by a perfectly plastic yield condition, and then it can be scaled by a damage function
3. Damage initiation when the stress reaches a failure criteria

The implementation is typically code dependent, for further information; refer to the LS-DYNA keyword user's manual [30] .

It is clear that the Tie-Break is a very flexible element that can be implemented to emulate many different scenarios such as bonded joints. In the case of adhesives, the Tie-Break is ideal to simulate debonding between two joined surfaces using very few computational resources.

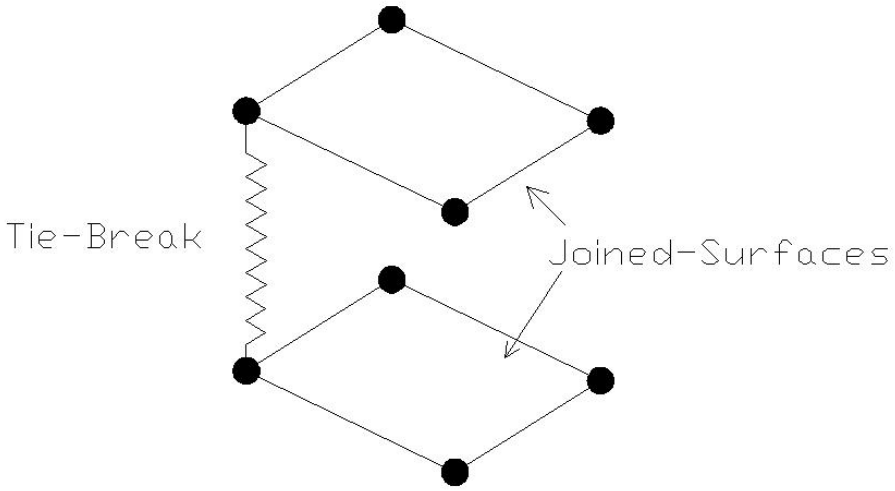

Figure 24: Tie-Break [30]

Although the Tie-Break provides benefits, mostly corresponding to ease of implementation and low computational demands, sometimes the physical response and behavior of the joint is not completely captured. One good scenario to describe this is crack propagation. During crack propagation the first element in the crack front carries a good portion of the load, once it fails that load is immediately passed on to the next element causing a "jolt" that can immediately overload the element. This behavior will continue from one element to the next causing what is termed "numerical unzipping". Depending on the code implementation this behavior can be addressed by the use of a critical opening. Only when the displacement between nodes reaches a critical value the element is deleted preventing sudden changes in load. This type of element also lacks the inclusion of strain-rate effects.

2.5 Using cohesive elements and Tie-Breaks to represent adhesives

As was introduced in section 2.3, two epoxy materials were selected for this study. In order to obtain reliable numerical representation of the adhesives when modeling crush tubes; preliminary work was developed in regards to the numerical representation of these two epoxy materials using cohesive elements and tie-breaks. A series of methods to determine the required parameters necessary for the numerical representation of the adhesive using cohesive elements were investigated. The proposed methods were then verified by comparing the results of numerical simulation using a double cantilever beam (DCB) specimen. The DCB test is primarily use to determine the fracture toughness (K_{IC}) of adhesive materials by relating this property with the load- displacement information generated during the test. Available results for EC-2214 material were used to compare against the response of the different numerical models.

The computer model was implemented using the commercial numerical code LS-DYNA following the ASTM D3433-99 standard, advantage of the symmetry (Figure 25) was use to reduce the size of the model and decrease computational time.

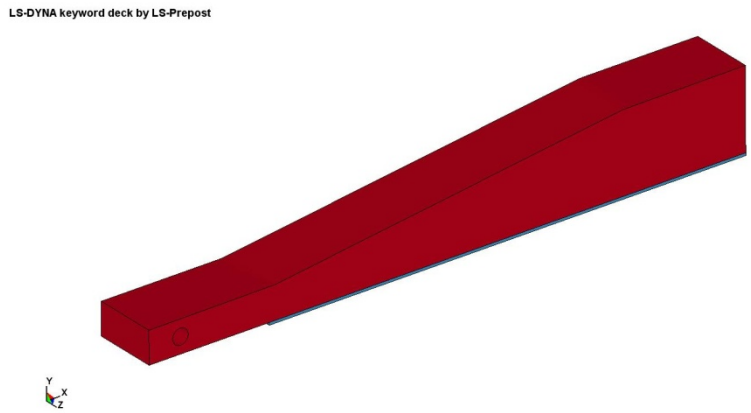

Figure 25: DCB test with symmetry

Cohesive element models are commonly used to describe adhesive material responses in joint configurations. For example, using an idealized traction-separation law, cohesive elements can predict crack growth and subsequent resistance. However, the difficulty with actually implementing a cohesive element lies in how to define the traction-separation law that describes the particular adhesive in question.

Three different implementations were developed for the present study; two responses were selected from a literature survey: a bilinear material response with a plateau [22, 42, 47] and a bilinear constitutive response [41], while the third used results from simple experimental data to generate the required traction-separation law.

2.5.1 Bilinear material response with a plateau

For practical purposes, fracture mechanics relations were used to approximate the required quantities that define the traction-separation law. The shape of the curve, as determined by the parameters δ_1 and δ_2, was assumed arbitrarily as a bilinear with plateau shape (Figure 26).

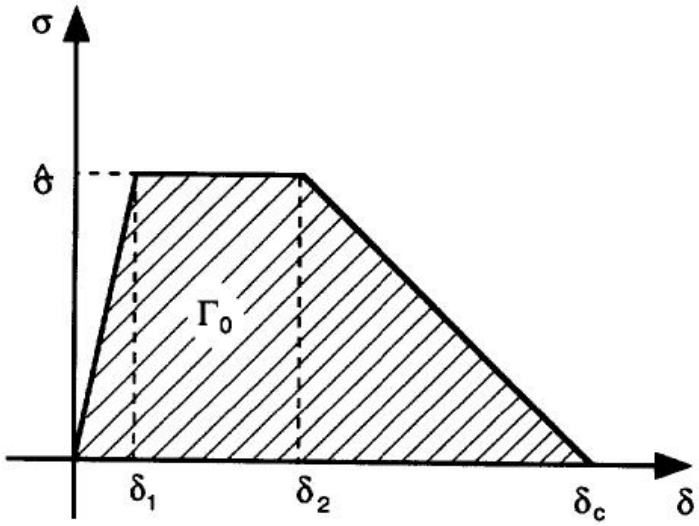

Figure 26: Bilinear with plateau traction-separation curve [47]

The maximum displacement in the joint is assumed to be equal to the crack tip opening, which can be defined as:

$$\delta_{max} = \frac{{K_{IC}}^2}{E\ \sigma_y}$$

Yang [47] noted that, "according to Tvergaard and Hutchinson the dominant parameters in the numerical analysis of fracture are the work of separation per unit area Γ_o and the apparent stress in the joint $\hat{\sigma}$; the precise shape of the traction-separation law is less important." With this in mind, an arbitrary shape can be defined for the model. Values for the inflection points were arbitrarily defined as:

$$\frac{\delta_1}{\delta_{max}} = 10\ \%$$

$$\frac{\delta_2}{\delta_{max}} = 40\ \%$$

The work of separation per unit area Γ_o was approximated using the fracture toughness of the material, such that:

$$\Gamma_o = \frac{{K_{IC}}^2}{E}$$

The apparent stress in the joint can be obtained by equating the area under the traction-separation curve to the work of separation:

$$\int \sigma(\delta)\, d\sigma = \Gamma_o$$

2.5.2 Bilinear constitutive response

A second approach to defining the cohesive model takes into account the constraints imposed on the joint by adhered materials. In this case, experimental data drawn from the available literature was used to determine the peak load that defines the peak of the traction-separation law (Figure 27).

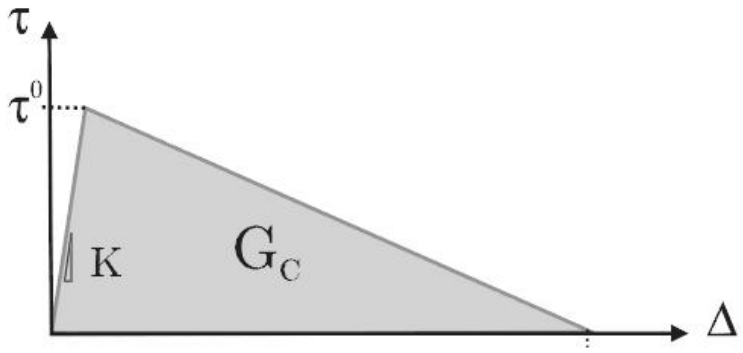

Figure 27: Bilinear traction-separation curve [41]

Several studies [14, 18, 32, 33] point to the fact that the strength in an adhesive layer depends not only on the bonding material (adhesive), but also on the geometry of the joint, the joined materials (adherends), and the mode of loading. To capture these effects, experimental data presented by Kafkalidis [22] was fitted to a non-linear model that predicts the peak traction stress experienced by adhesive joints subjected to peel forces in a DCB experiment. The derived formula incorporates the mechanical properties of the materials, as well as the thicknesses of both the bond and adherends.

$$\tau = \frac{7.95\text{x}10^{-11}\left(\frac{E_l}{\sigma_y}\right)^{0.069}\sigma_y}{\left(\frac{t_l}{t_{ad}}\right)^{0.21}\left(\frac{E_{ad}}{\sigma_y}\right)^{8.45}}$$

Equation 20: Damage initiation traction

Equation 20 describes the strength of an adhesive layer confined by two identical materials; where τ represents the traction strength of the material, E is the elastic modulus of the adhesive layer (sub-index l) and the adherents (sub-index ad). The model considers the geometry of the joint by incorporating the thickness (t) of both the adherent (ad) and the adhesive (l), and uses the yield strength of the adhesive (σ_y). Details of the derivation are presented in Appendix B.

2.5.3 Constitutive response curve from experimental data

Both previously described methods are cumbersome for defining cohesive elements; they require specific knowledge of the material's mechanical properties, such as its fracture toughness, and one requires additional experimental data for curve fitting. However, this information may not be readily available. To simplify the process and to avoid the pitfalls of extensive mechanical testing, a new approach was developed.

From simple mechanical testing we fully define a cohesive element by:

- Using the yield and shear stresses to determine the peak tractions
- Using the ultimate strains to define the critical displacements
- Normalizing the stress-strain curve to provide the shape of the traction-separation curve
- Back calculating the energy release rate from Equation 21

$$\delta = \frac{G^c}{T\, A_{TSLC}}$$

Equation 21: Traction damage [29]

2.5.4 Cohesive models constitutive responses

Since experimental DCB results were available for EC-2214, this epoxy material was implemented as a cohesive element using both bilinear and bilinear with plateau representations. The simulation results, presented as force-displacement diagram (Figure 28) were then compared against the experimental data. A more comprehensible summary of the results for both the simulations and the experiment are shown in Table 2. It is easier to compare the values for different significant parameters that can be extracted from the data such as the fracture toughness (K_{IC}).

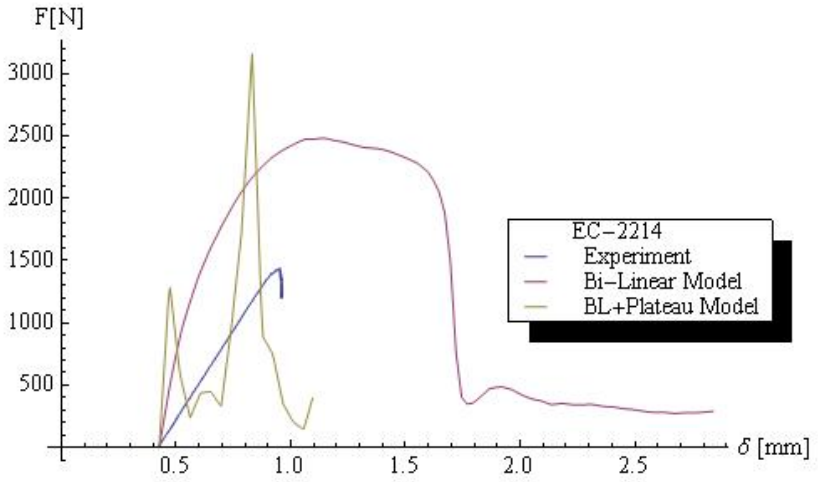

Figure 28: Symmetric model of DCB results for cohesive elements

	LS-DYNA Model Max value	LS-DYNA Model Min. value	LS-DYNA Model Average	Experiment
Load [kN]	2.5	0.5	1.5	1.4
G_{IC} [N/m]	1961	78	1019	615
K_{IC}[MPa $m^{1/2}$]	3.13	0.63	1.88	1.75

Table 2: DCB symmetric simulation results for Bi-linear model

Based on this simulation results, the bilinear model appeared to more accurately describe EC-2214 than the bilinear with plateau model. However, it was also clear that the numerical model required some refinement since the cohesive elements were not good on a symmetry plane; thus, a full model of the DCB test was developed (Figure 29).

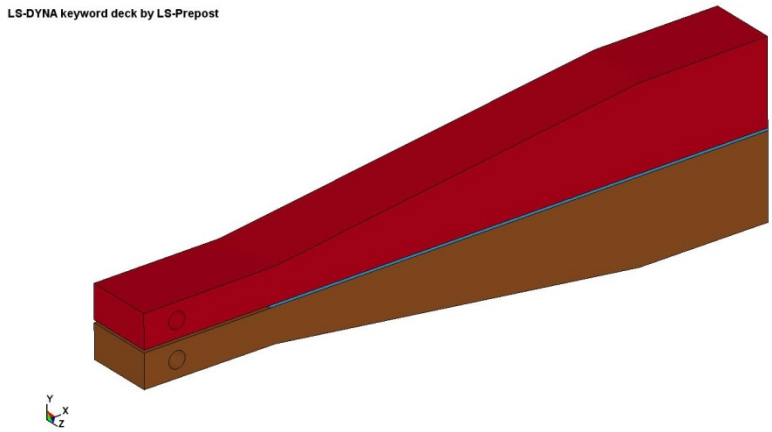

Figure 29: Full implementation of the DCB test

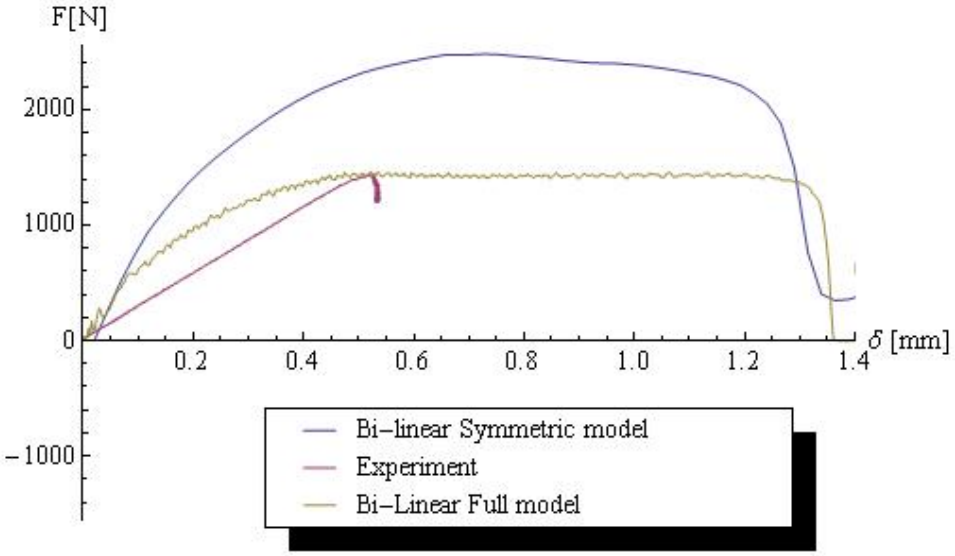

Figure 30: DCB simulation, models comparison for EC-2214

Both epoxy materials were implemented as cohesive elements using curves from the Lap-Shear test (Figure 20). The simulations responses for the DCB test with the cohesive element derived in this manner were compared against the bilinear model (Figure 31). Although both models seem to

correctly predict the force required to drive crack propagation, it is clear that the initial stiffness of the joint is better described by the bi-linear model.

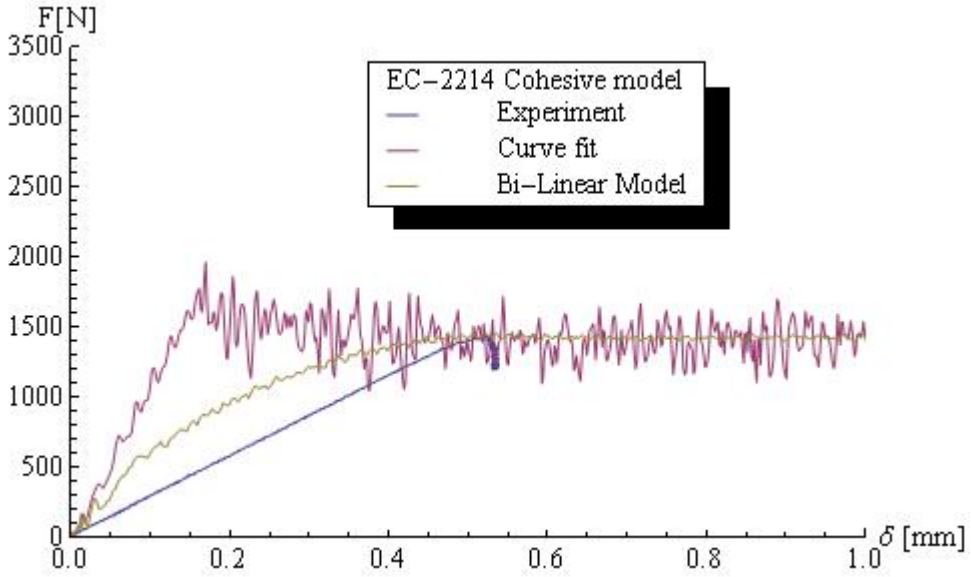

Figure 31: Simulation results - DCB test models vs. experimental results

Although the DCB load-displacement experimental results were not available for DP-460NS, a simulation using cohesive elements constructed by fitting the experimental data from the Lap-Shear test (Figure 21) was implemented. For comparison against materials, the response of the DCB simulation was plotted (Figure 32). As expected, DP-460NS requires a higher load to drive crack propagation; this is in agreement with the quasi-static test results where DP-460NS shows more ductile behavior compare with EC-2214.

Results from this simulation were used to calculate the fracture toughness and compared directly against the material properties (Table 3) and were in good agreement.

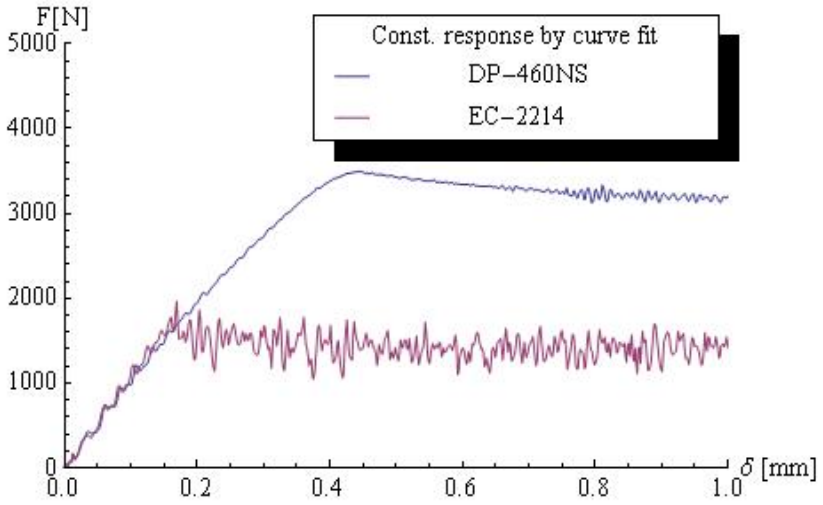

Figure 32: Simulation results of DCB test cohesive model derived from experimental curves

	LS-DYNA Model Max value	LS-DYNA Model Min. value	Ls-DYNA Model Average	DP-460NS approx. values
Load [kN]	3.48	3.03	3.25	
G_{IC} [N/m]	3805	2881	3343	2574
K_{IC}[MPa $m^{1/2}$]	2.89	2.52	2.70	2.38

Table 3: DCB results for DP-460NS

As shown in Figure 31, the bilinear model response differed from that of the constitutive curve obtained by using the lap-shear experimental data, particularly with regard to initial stiffness (as described by the slope of the load-displacement curve). By comparison with the experimental results, the bilinear model appears to more accurately predict EC-2214 behavior; however, there are many drawbacks to this approach. For example, more data is required if the expression presented in Equation 20 is applied to other cases which may include joining dissimilar materials and varying the thickness of the adhesive and/or the adherends.

2.5.5 Using Tie-Breaks to represent adhesives

Tie-Breaks are numerically simple, and therefore have the advantage of requiring fewer computational resources. For this work, two different implementations of the LS-DYNA card

*CONTACT_AUTOMATIC_SURFACE_TO_SURFACE_TIEBREAK were compared against the more complex cohesive material model. Tie-Breaks were used to represent a DP-460NS adhesive joint and results compare against the previously establish cohesive model. Characteristics of each Tie-Break follow after.

2.5.5.1 Implementation 1, spring with failure (TB1)

The first implementation (TB1) defined a Tie-Break between surfaces in contact with the hats, using contact type option #6 offered in LS-DYNA. In this formulation, the Tie-Break is active for nodes initially in contact, and failure is defined by stress values in both the normal and shear directions. After failure, the critical distance defines behavior. In this implementation, failure stress values in the normal direction, as presented in Table 1, are the only data required. For the shear direction based on classical considerations, one can assume these stress values equal to roughly half the tensile value. The critical distance can be defined as the distance at which first yield occurs - in this case 0.1 mm was used. Predicting the critical distance accurately may be essential to achieving meaningful results since it can affect the amount of energy the joint dissipates once the spring fails, and hence change the response of the model. Because the force-displacement curve and modulus of elasticity are not defined, one will think that the spring will behave as a rigid member with no displacement until after the moment of failure; in the case of LS-DYNA, the code automatically calculates the stiffness of the joint by using the properties of the joined materials and considerations in regards to tributary areas assigned to the connected nodes.
Of consideration for users: option #6 only works with thick shells and solid elements; in the case of structures in contact defined by shells, the option must be changed to number 8.

2.5.5.2 Implementation 2, discrete crack model (TB2)

The second implementation (TB2) used the discrete crack model (option #9, in the LS-DYNA card; Option #11 must be used for shell elements). This type of contact aims to provide a better representation of the material by incorporating energy considerations in the failure criteria, while eliminating the numerical burden imposed by cohesive elements. In this case, failure is not only defined by failure stress, it also takes into account energy release rates, which determine when the failure occurs, and a curve, which describes the force displacement behavior. By contrast with TB1, this formulation allows the element to deform the material at any given moment in time as a function

of the load-displacement curve provided. This Tie-Break is very similar to a cohesive element (Figure 33).

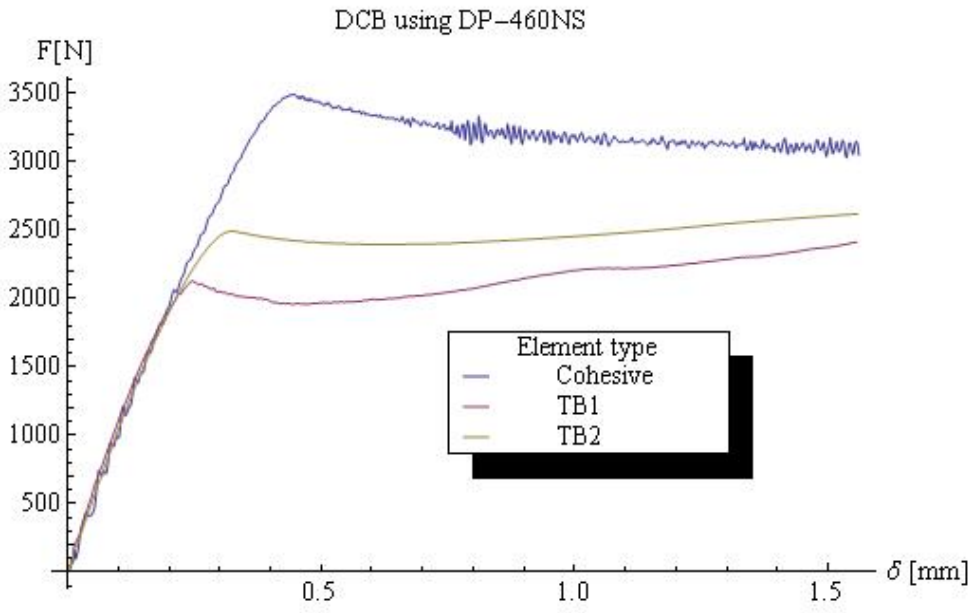

Figure 33: Material model response for a DCB simulation

Tie-Breaks potentially offer major savings in computational time (Figure 34). The use of solid elements can lead to prohibitively long simulation times, particularly if an elaborate material implementation and sufficient elements are used to capture the mechanical behavior properly.

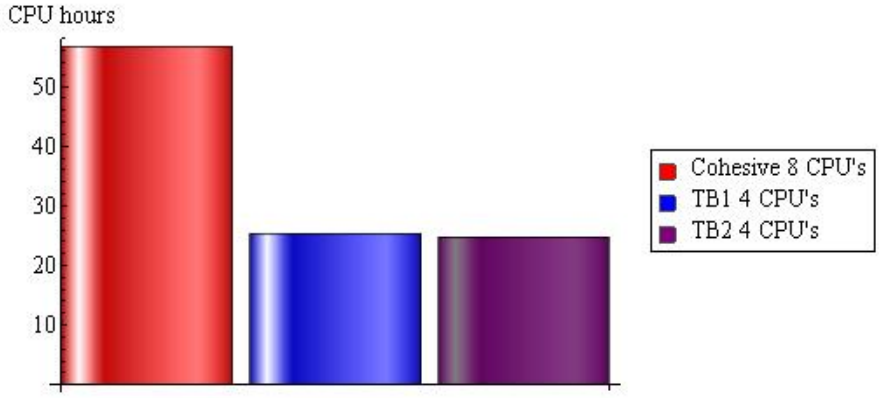

Figure 34: CPU times for DCB simulations using different material implementations

Chapter 3

Sub-Scale crush tubes

Experimental testing is an invaluable, often essential, procedure engineers and scientists use to verify theories, develop a better understanding of structural and/or material behavior, or gain insights into a particular phenomenon. Testing when other means are not available is a way to perform these types of investigations but can be limited by equipment availability, capacity for loading and cost. For example, full-scale impact testing of automotive crash members may be an impossibility for some researchers, and even to some industrial R&D departments, due to equipment size and budget constraints. This work was no different; experimental testing was required to validate proposed numerical methods; however, full-scale impact testing equipment was not available. The most practical solution was to scale the event so laboratory-scale equipment could be used for this task.

3.1 Scaling structures during impact events

As described in Section 2.4, strain-rate sensitive structures cannot be scaled using conventional techniques; traditional scaling laws become distorted when applied to structures subject to dynamic loads, which limits the usefulness of sub-size specimens in analyzing structural behavior under impact scenarios. However, Oshiro and Alves [34, 35, 35] proposed a non-direct similitude technique to overcome these limitations. In this approach, strain rate effects are accounted for by redefining a new base for the set of dimensionless numbers in terms of the impact mass, G, initial impact velocity V_0, and dynamic yielding stress, σ_d, instead of the traditional Mass Length Time (MLT) approach.

3.1.1 Scale correction

Oshiro and Alves set to solve the non-scalability of impacted structures due to strain-rate effects by finding the initial impact velocity for the model such that both the model and prototype are scaled. For this purpose, they manipulated the dimensionless numbers (also known as Π numbers) and defined the following equation to correct the distortion of a model subject to impact loads:

$$\beta_{V0} = \sqrt{\frac{f(\beta_{V0}\dot{\varepsilon}_m^{nc})}{f(\beta\dot{\varepsilon}_m^{nc})}}$$

Equation 22 Correction for scaling impact velocity

Where β_{V0} is the scale factor to determine the proper impact velocity for the model, β is the dimensional scale factor for the experiment, $\dot{\varepsilon}_m^{nc}$ is the strain rate in the non-corrected model, and f is the function that describes the constitutive model that characterizes the material behavior. Further details are provided in [34].

3.2 Non-direct similitude verification

Although Oshiro and Alves successfully applied the non-direct similitude technique to cylindrical shells, demonstrating remarkable similitude between model and prototype [36]; to build further confidence in the technique and to verify the applicability of the procedure to other geometries, an impact scenario described by Tarigopula et al. [40] was replicated using an explicit finite element code (LS-DYNA, LSTC).

3.2.1 Experiment description

Tarigopula's experiment, referred to as the 'prototype', consisted of a thin-walled square tube specimen (60 x 60 mm cross section, 1.2 mm wall thickness and 310 mm length) made out of dual phase high-strength steel alloy, DP800, subjected to a dynamic axial crushing test with an impact mass of 600 kg moving at 5 m/s at the moment of contact.

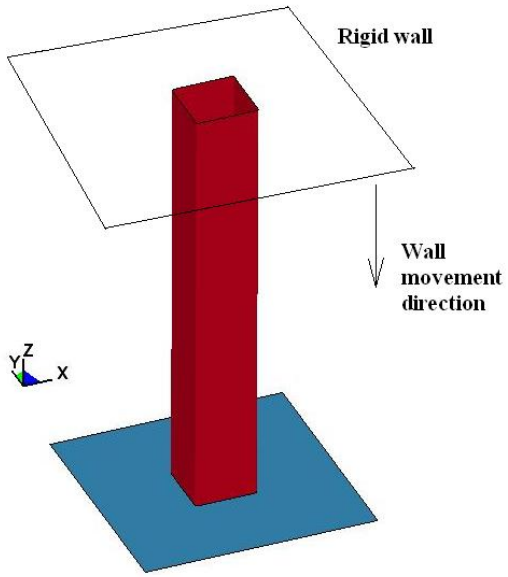

Figure 35: Impact simulation for scaling; 1:1 event

The simulation **(**Figure 35**)** was implemented to be as close as possible to the one described by the author [40] in his paper in terms of geometry of the crush tube as well as boundary conditions and size of element use. The tube was mesh using 3mm elements and the corners were refined by using 3 elements across the corner length as stated on the paper.

3.2.2 Material model

The material model presented by the author to describe the dual phase steel, DP800, was an isotropic (ISO) hardening model corrected for strain rate effects, Equation 23. This material was implemented by Tarigopula in two different ways using the LS-DYNA code: for simulation of quasi-static events by using *MAT_103 and for dynamic events a user defined model. To describe the material and avoid the use of multiple models depending on the type of event, a curve fitting using the Johnson-Cook model (Equation 24), was implemented by fitting the Cook model against data generated using the isotropic hardening model of this material. The difference between the material model responses used for simulation and actual test results is presented in Figure 36. In this figure, the results presented under the ISO-Hardening label and the experimental label, correspond to a digitalization of the curves presented in the literature by the author [40]. The document did not provide enough information to implement the user material model required to execute the actual simulation.

$$\boldsymbol{\sigma = (495 + \left(200\left(1 - e^{-76\varepsilon}\right)\right) + \left(233(1 - e^{-10\varepsilon})\right))\left(1 + \frac{\dot{\varepsilon}}{\dot{\varepsilon_o}}\right)^{0.0116}}$$

Equation 23: Isotropic hardening model for steel material DP800

$$\boldsymbol{\sigma = \left(495 + 1123.08\varepsilon^{0.46}\right)\left(1 + 0.012\ \mathrm{Ln}\left(\frac{\dot{\varepsilon}}{\dot{\varepsilon_o}}\right)\right)}$$

Equation 24: Johnson-Cook model for steel material DP800

In the previous two equations, $\dot{\varepsilon}$ and $\dot{\varepsilon_o}$ denote the effective strain rate and the reference strain rate. For this material $\dot{\varepsilon_o} = 10^{-3}$ 1/s

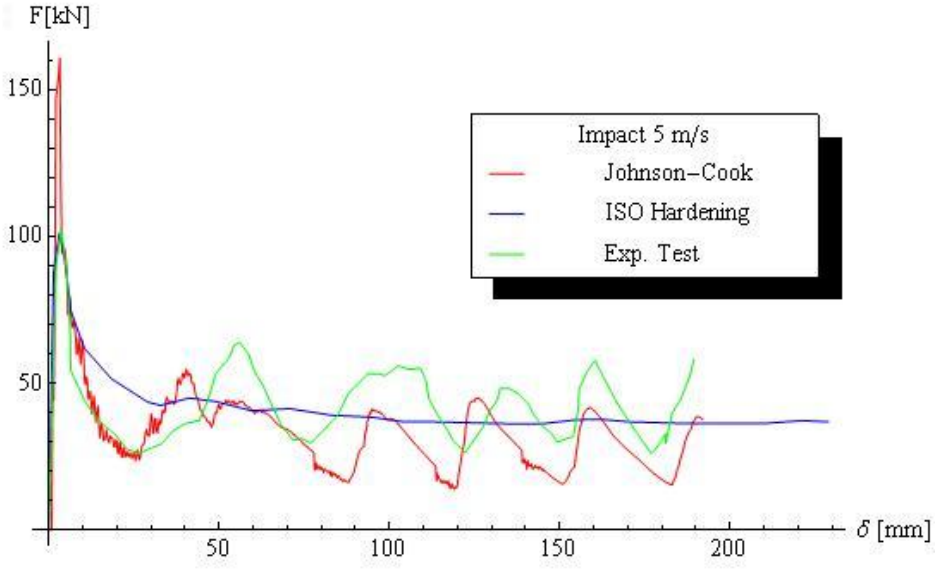

Figure 36: Selected material model vs. literature results

3.2.3 Model parameters, Scale correction factors

To build the model, the prototype was scaled by half (1:2).

3.2.3.1 Scale factor β

As the scale factor for the model is half, the impact mass scales to 600 * $(1/2)^3$= 75 kg. All other geometrical dimensions are also scaled by half. The geometries of both the prototype and model can be seen in Figure 37.

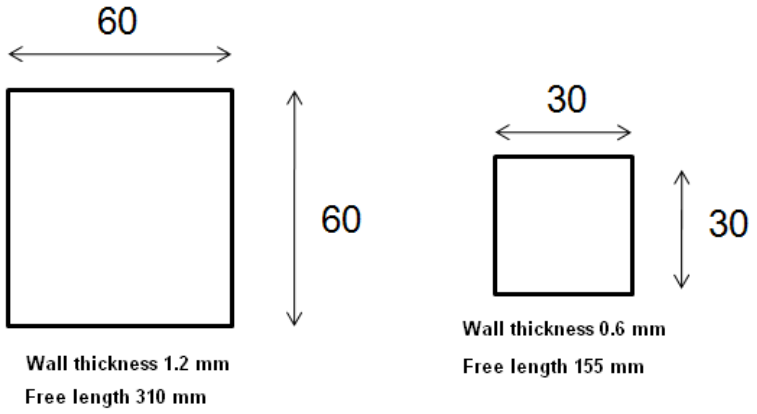

Figure 37: Prototype and model

3.2.3.2 Velocity correction factor β_{V0}

In order to accurately scale the event, the proper correction factor for the impact velocity, β_{V0}, must be determined. To calculate this factor Equation 22 can be combined with Equation 24, as shown below. To determine the strain rate in the non-corrected model, $\dot{\varepsilon}_m^{nc}$, we can use the original impact velocity of 5 m/s and a characteristic length, in this case the length of the tube 150 mm. The base strain rate for the material model, $\epsilon_o{}^*$, is assumed to be 1 1/s for simplicity; since the exact reference strain rate for the material was not known. The reference strain rate value has very little impact in the calculation compare to the other parameters, then the error introduce with this assumption is very small.

$$\beta_{V0} = \sqrt{\frac{(495 + 1123.08\varepsilon^{0.46})\left(1 + 0.012\ \mathrm{Ln}\left(\beta_{V0}\frac{5/0.150}{1}\right)\right)}{(495 + 1123.08\varepsilon^{0.46})\left(1 + 0.012\ \mathrm{Ln}\left(0.5\frac{5/0.150}{1}\right)\right)}}$$

From this calculation, the correction factor is 1.00404 and the corrected impact velocity is 5.02 m/s.

3.2.4 Results

As shown in Figure 38, the similitude between prototype and model is very good; the described deformation and pictured stresses in both structures are in agreement. Furthermore, the energy absorption between prototype and model was accurately described by the non-dimensional number that describes the event (Equation 25). Results in Figure 39 show the agreement between model and prototype according to the predictions of the non-dimensional number at a fix point of displacement close to the end of the event. At 200 mm of the striker stroke the prototype has absorbed 6.5 kJ of energy; on the model this would correspond to half the displacement (100 mm) at this point the model absorbed around 820 J of energy, which was corroborated by the non-dimensional number calculation.

$$\Pi = \frac{\delta^3 \sigma}{G\, V_0^2}$$

Equation 25: non-dimensional number, energy prediction for scaling of dynamic events

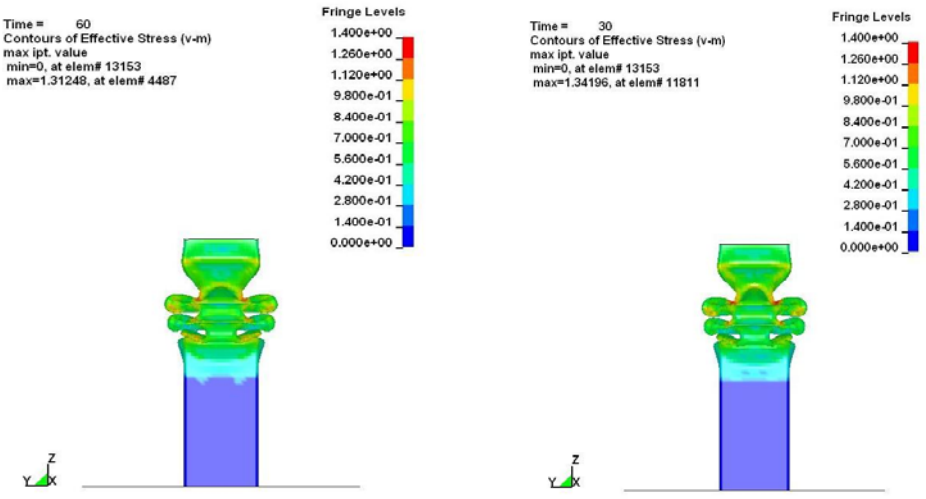

Figure 38: Prototype (right) vs. model (left), stress and deformations results. Model and prototype shown at the same scale.

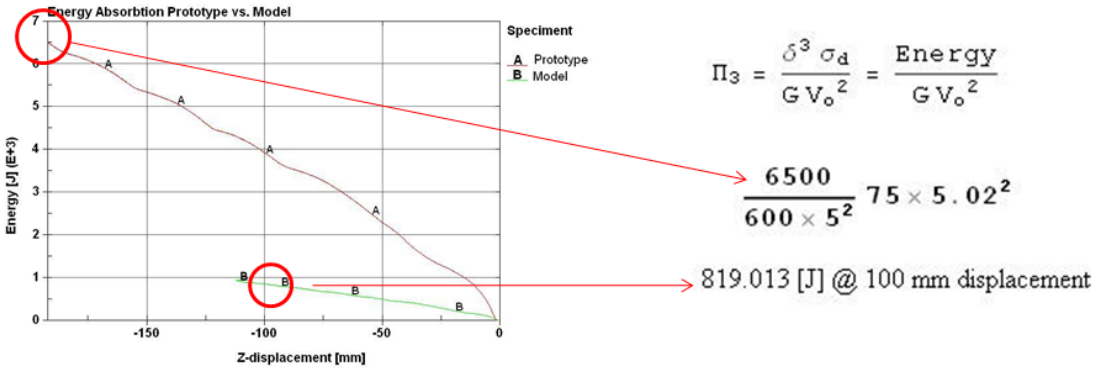

Figure 39 :Non-dimensional number calculation for square tubes

3.3 Validation of sub-size structures with the inclusion of adhesives

Although we can be confident that the scaling procedure works well when only one material is involved in the dynamic event, the incorporation of an additional material, in this case an adhesive layer; introduces a level of uncertainty. To verify that the procedure can successfully be extended to

multi-material structures, a drop tower experiment, described in detail in Chapter 4, was reproduced as a numerical model and the results compared against a scaled up simulated model of the same event. If the scaling procedure is valid, the predicted deformation and stress distributions should be similar between the model and prototype. In addition, the model must accurately predict the energy absorption in the crush tube prototype using non-dimensional numbers.

3.3.1 Experiment description

The experiment selected for verification was performed using an instrumented drop tower. Because the sub-size crush tube used in this experiment is considered a scaled down representation of a bigger event, the experiment is referred to as the 'model'. The sub-size crush tube consisted of thin-walled square tube built by joining two 200mm hats of commercial steel. The crush tube was subjected to a dynamic axial crushing test with an impact mass of 56.18 kg moving at 7.24 m/s at the moment of impact. The simulation described the hat section geometry by using 2mm shell elements and followed the experiment details are described in 4.3.

3.3.2 Material model

The mechanical response of the commercial steel used to build the crush tubes was described using the Cowper-Symonds model. This material model assumes an isotropic material with hardening and accounts for strain rate effects. Details can be found in Chapter 5 for the derived expression (Equation 27) which is repeated below

$$\sigma_o^d = 367.2\ (1 + \left(\frac{\dot{\varepsilon}}{306.31}\right)^{1/3.61})$$

3.3.3 Scale correction factors

To build the prototype, the model was up scale by a factor of two (2:1).

3.3.3.1 Scale factor β

As the scale factor for the prototype is two, the impact mass scales to 56.18 * $(2)^3$= 449.4 kg. All other geometrical dimensions are also scaled by two.

3.3.3.2 Velocity correction factor β_{V0}

In order to accurately scale the event, we need to determine the proper correction factor for the impact velocity, β_{V0}, during the event. To calculate this factor we can combine Equation 22 with Equation 27

$$\beta_{V0} = \sqrt{\frac{1 + (\beta_{V0} \frac{V/_{0.4}}{306.31})^{0.277}}{1 + (0.5 \frac{V/_{0.4}}{306.31})^{0.277}}}$$

Since we know that the impact velocity of the model is related to the impact velocity in the prototype through β_{V0} ,

$$V\,\beta_{V0} = 7.24$$

Then we can replace in the previous equation and solve for the velocity on the prototype.

$$\frac{7.24}{V} = \sqrt{\frac{1 + (7.24 \frac{1/_{0.4}}{306.31})^{0.277}}{1 + (0.5 \frac{V/_{0.4}}{306.31})^{0.277}}}$$

For the prototype the impact velocity was calculated as 7.03 m/s.

3.3.4 Results

As shown in Figure 40 there was a good degree of similitude between prototype and model in terms of stress levels and the described deformation between the structures was also in agreement. Of importance was the energy absorption prediction between prototype and model. When comparing at fix points of the striker stroke, 40 mm for the prototype and 80 mm for the model, the energy absorption, 1.47 KJ and 11.09 kJ respectively, was not accurately predicted (9.39 kJ) by the non-dimensional number (Equation 25) that can be used to correlate model and prototype during the event. Results are shown in Figure 41. Introduction of the adhesive joint had effects on the overall predictions; however, the scaling of bonded structures can be an acceptable procedure, but with limitations.

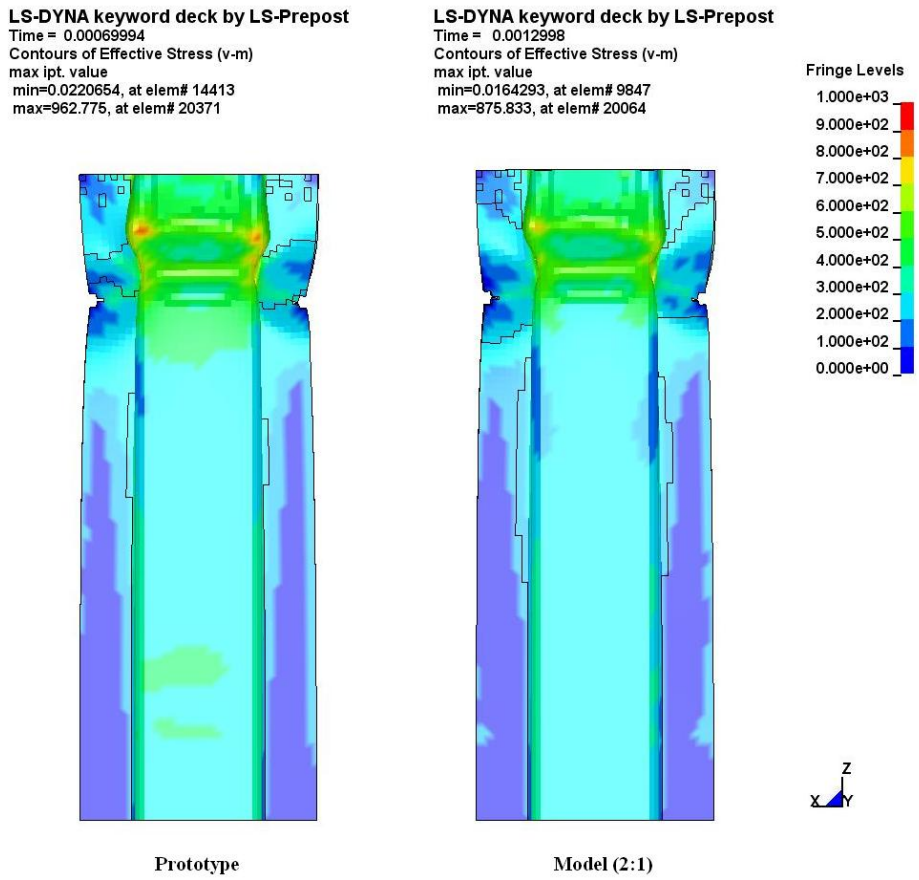

Figure 40: Prototype (left) vs. model (right), stress and deformations results for bonded hats

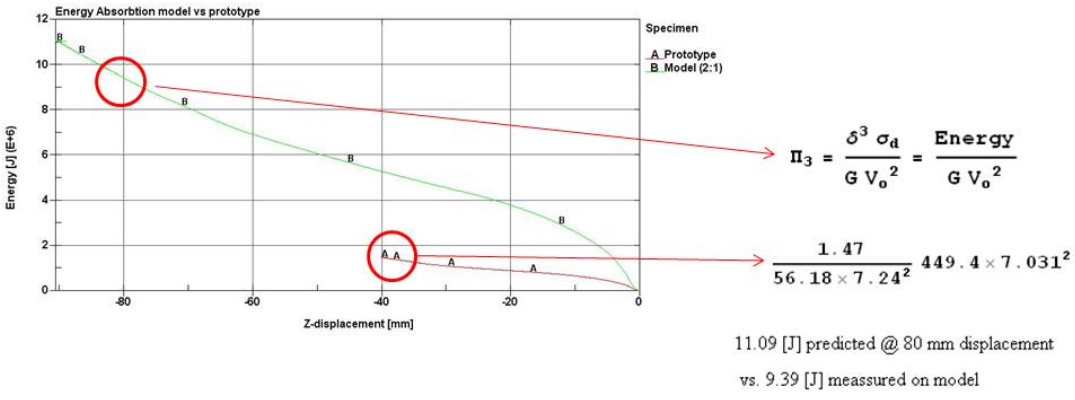

Figure 41: Hats non-dimensional number calculation, energy prediction

The computer model for the prototype was also compared against the experiment performed on the drop tower for certainty in the computer model. Although there are minor differences, the prototype, represented by the computer model and the experiment were in good agreement, Figure 42.

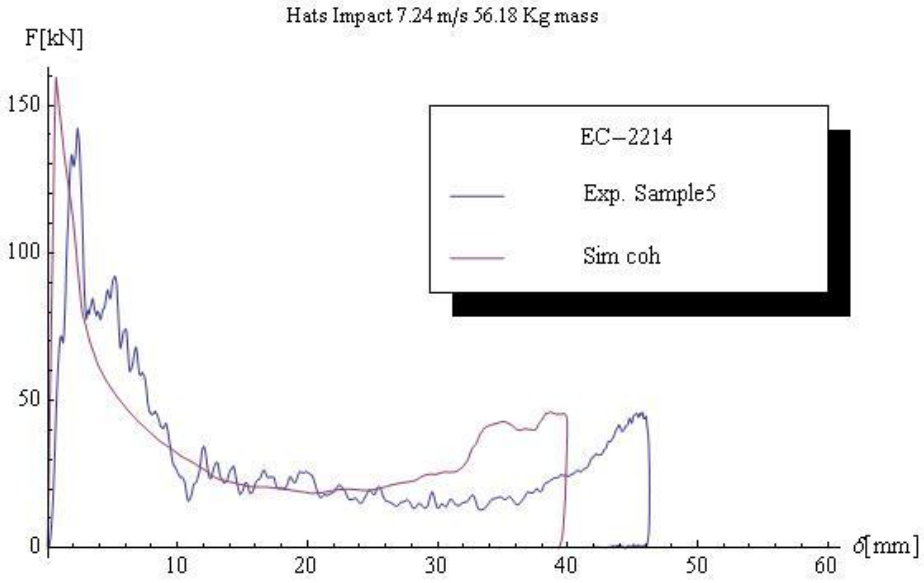

Figure 42 Bonded hats with EC-2214 simulation (prototype) vs. experiment

Chapter 4
Crush tubes experimental testing

Experimental testing was required to gain a better understanding of the mechanical properties of the bulk material used to manufacture the steel sections used in this work as well as the crush behavior in adhesively joined crush tube structures. The experimental testing provided the necessary data to verify the numerical models.

4.1 Steel material mechanical properties

Commercial roll form sections made out of an undefined steel alloy were outsourced to build the crush tubes. To define the material properties, a series of quasi-static and dynamic tensile tests were performed using steel samples (Figure 43) cut off from the material. Two batches of roll form shapes were received from the manufacturer on separate dates. To ensure that the material properties were consistent between batches, a hardness test was performed and the results were statistically compared.

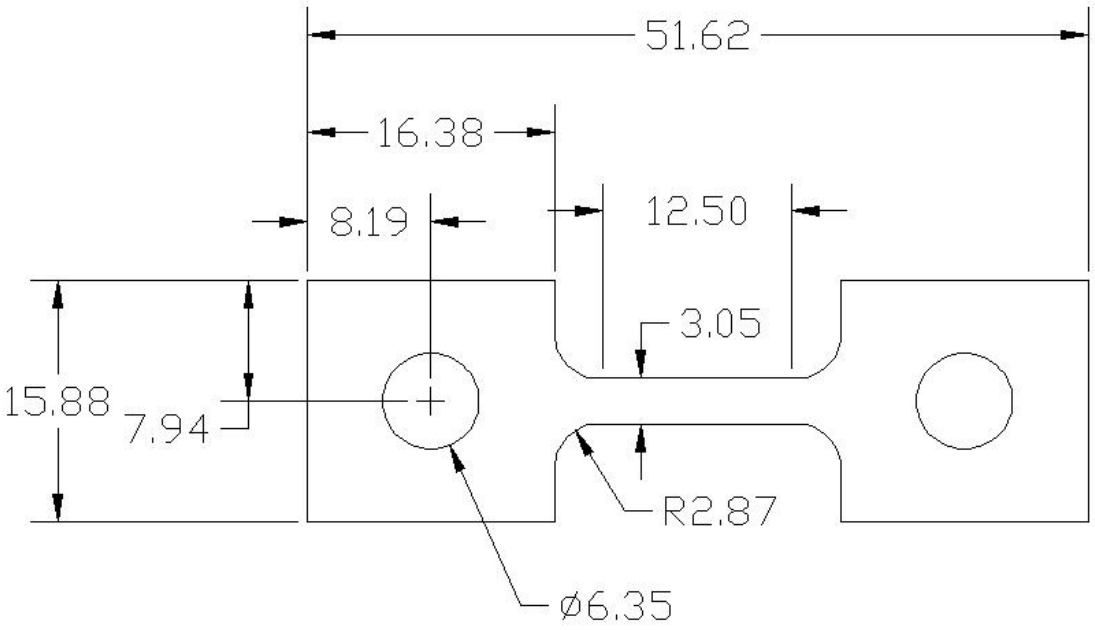

Figure 43: Steel sample for testing cut from material

4.1.1 Tensile testing

The quasi-static test was performed using an Instron universal testing machine. Dynamic tensile testing was performed using a hydraulic machine that permits strain rates from 10 1/s up to 100 1/s. Results of the tensile tests are presented in Figure 44.

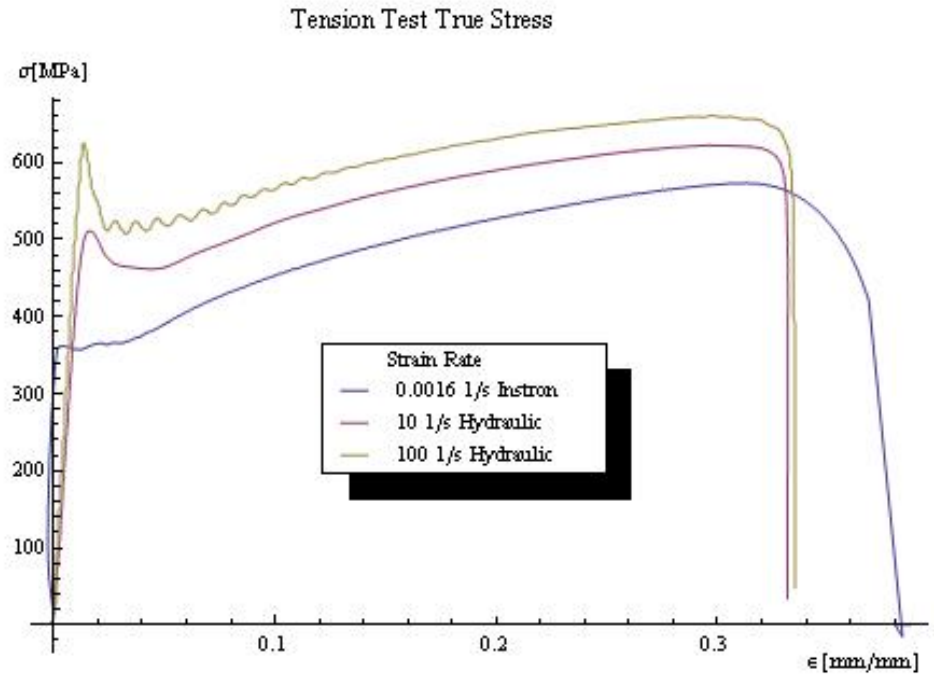

Figure 44: Tensile testing steel material true stress vs. true strain

One particular characteristic of this steel material was the increase of yield value with strain rate and subsequent softening. The effect was not apparent in the quasi-static testing but was more pronounce as the strain rate was increased. Some authors [9, 19] have noted this previously. Itabashi and Kawata [19] explored this phenomenon and related it to carbon content. With lower carbon content, the peak yield effect with subsequent softening is more pronounce and fades out as the carbon content is increased. There are other studies [10, 11] in which alloy type or microstructure seems to reproduce or not the same effect.

Testing at higher rates was not possible with the hydraulic equipment, and the use of split Hopkinson bars was precluded due to availability. Testing in the intermediate range 100 to 1000 1/s was not possible either, due to lack of suitable equipment.

4.1.2 Hardness test

To ensure that the material properties were consistent across the sections received from the manufacturer, a series of hardness tests, Rockwell B (HRB) and Vickers micro-hardness (HV), were performed using random samples. It should be noted that the first batch of material consisted entirely of hat sections, while the second batch included both hats and channels. The Rockwell test was performed directly on the section, while the micro-hardness test required cutting samples out of the material and mounting them on Bakelite (Figure 45). The measurements on this case were made across the thickness of the section material avoiding the galvanization layer. Results are presented in Figure 46 and Figure 47.

Figure 45: Micro-hardness test samples. Cut material (left), mounted material on Bakelite (right)

Hypothesis testing was used to determine if there were significant differences in the measured hardness between batches of material. Four sets of t-test with a 95% confidence level, as presented in Table 4, were used to compare the means from the hardness test measurements. First, hat samples from batches 1 and 2 were compared; then all of the hat samples and channels were compared. It was determine that there was no significant difference for the hat materials between batches 1 and 2 since the value of the observed T (T_{obs}) was less than the value of the critical T (T_{crit}).

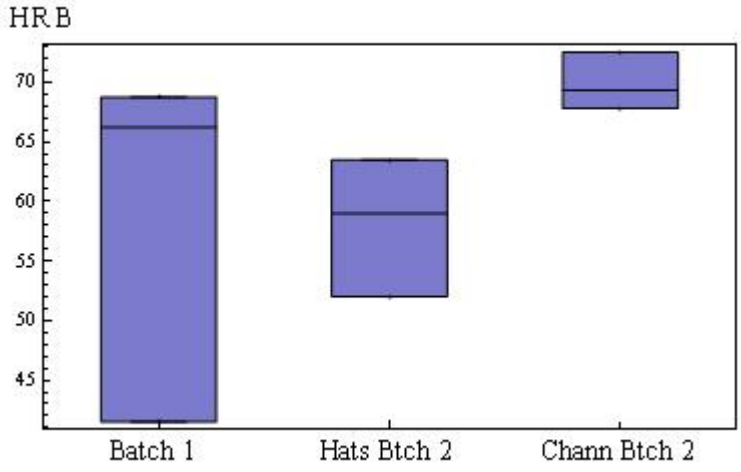

Figure 46: Hardness Rockwell B results

Comparison between the mean value of the hardness for the hats, independent of batch, and for the channels, show discrepancies on results; however this discrepancy was dependent on the hardness test selected for comparison. If results from the HRB test were to be used, the t-test revealed no differences between materials; on the other hand, if the HV test results were considered, there is a clear difference between the materials used to manufacture the two different sections.

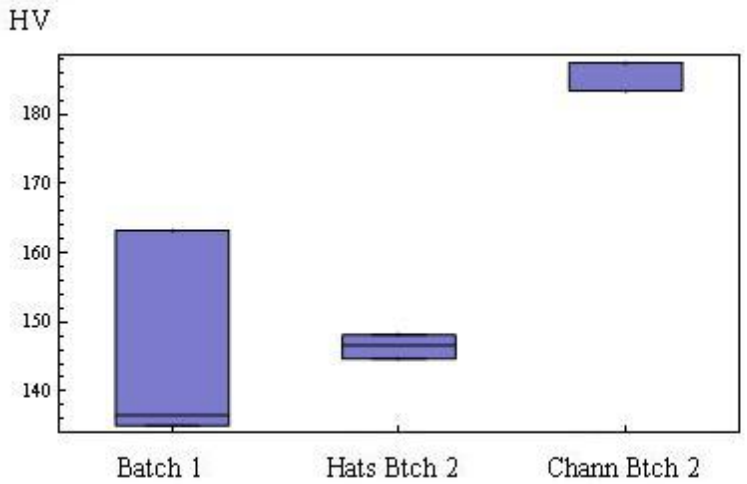

Figure 47: Hardness Vickers's results

Roll Form Section	Rockwell B		Vickers's	
	T_{obs}	T_{crit}	T_{obs}	T_{crit}
Hats 1st batch vs. Hats 2nd batch	1.38	2.09	0.80	2.36
Hats vs. Channels	1.56	2.07	9.14	2.20

Table 4: T-test hardness data results

Roll Form Section	HV	UTS [MPa]
Hats	143.74	490.15
Channels	186.46	635.84

Table 5: Ultimate strength of material from hardness test

Although there is a significant difference between the HV results for hats and channels($T_{obs} >> T_{crit}$), as presented in Table 5, if one looks at the correspondent ultimate tensile strength, calculated from the HV test results also included in the same table and calculated from the Vickers's micro-hardness test results; it is hard to conclude if the variance in the results is part of normal statistical variation inherent to the material or if indeed there was a significant difference in the compositions of the steel among the two shapes. Also there could be effects due to the cold forming during the manufacturing process of the sections.

For practical purposes, the material used to manufacture the hats and channels was considered identical for this study.

4.2 Quasi-static testing of crush tubes

During quasi-static testing, the load is applied at rates slow enough so that the material strain rate effects do not influence the results. Sub-size crush tube structures were tested at quasi-static rates to determine the structure response to axial loads.

4.2.1 Equipment

An Instron universal testing machine model 4206 (Figure 48) was used to generate force-displacement diagrams at a low rate of displacement, 17 mm/min. The machine has a load cell with a

maximum capacity of 150 kN to measure the loads and, at the same time, keep track of resulting displacements by measuring the cross head displacement during the test.

Figure 48: Instron universal testing machine model 4206

4.2.2 Geometry of the samples

Commercial roll formed sections were purchased (Figure 49) to build crush tube structures. Two different cross sections were selected, a hat and a channel. These two shapes allow constructing crush tubes (Figure 50) that would be representative of actual geometries intended for field use in automotive energy absorbing structures.

The sections were assembled into crush tubes maintaining a 1 mm bond thickness at the joining surface by means of spacers and then cured in a convection oven at the recommended temperature for the adhesive as specified by the adhesive manufacturer. The assembled sections were then cut to 200 mm lengths and later indented with a buckle initiator using a manual press. The buckle initiator

reduces the peak load required to initiate the folding process during axial loading. The detailed manufacturing process is documented in Appendix A.

Figure 49: Steel sections as receive material, Hats (Left) Channels (right)

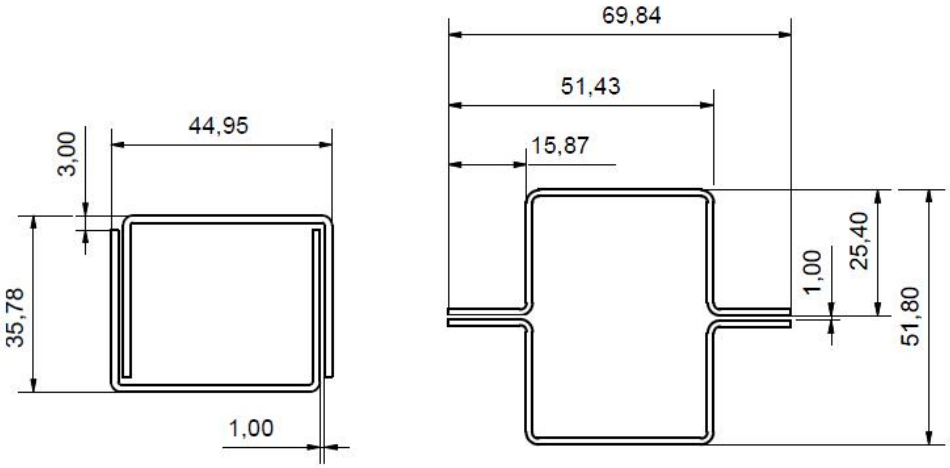

Figure 50: Built-up cross section dimensions

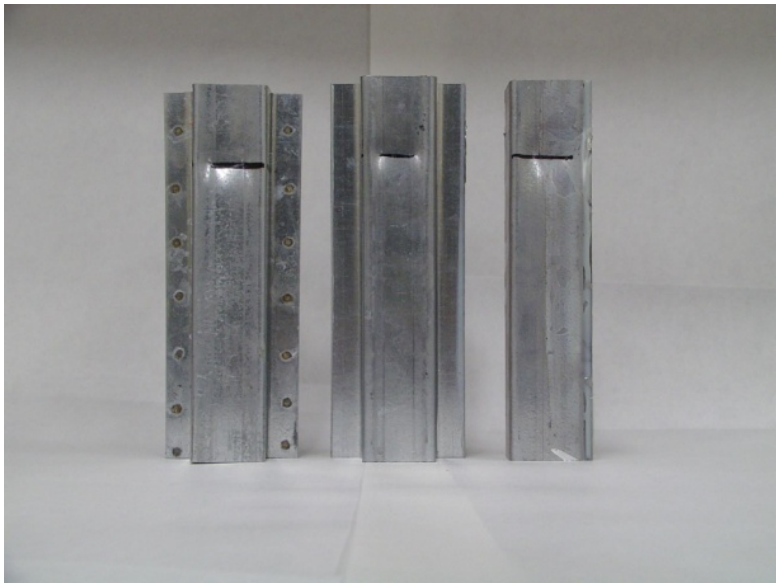

Figure 51: Assembled crush tubes, from left to right: welded hats, bonded hats and bonded channels

Quasi-static and dynamic testing was performed on each of the assemblies shown in Figure 51. Alternate sections joined by traditional spot welding were used to verify the performance of adhesives against traditional joining methods. Three samples of each tube were tested to obtain statistical relevance.

4.2.3 Double hat sections results

Load-displacement curves measured experimentally and images of the final deformed shapes are depicted in Figure 52 to Figure 60.The general characteristics of the deformation for the different structures can be seen through the presented pictures and discussed in more detail below.

Figure 52: Deformed hat sections during QS testing. Welded (left), bonded DP-460NS (center), bonded EC-2214 (right)

Out of the tested samples there was in general good agreement in terms of deformation consistency for the tubes bonded with adhesive (Figure 52, center and right pictures). In the case of the welded hats (Figure 53), the experimental results (Figure 54) do not suggest major differences between the spot welded samples, even though there was some degree of variability in the deformed shape among them (Figure 53). Notice the significant drop on the performance of sample T-11B during a part of the test. This sample is the only one that does not have a consistent folding pattern during the deformation process, evidently not developing folds influence the capacity for energy absorption.

Figure 53: Deformed welded hat sections during QS testing

For the particular case of sample T-11B, after reviewing the test video, the failure was initiated by an opening in the lip in mode I in a location between two spot welds. At this point the lips cave in towards the center of the section propitiating the formation of a fold at the bottom and preventing the fold formation in the upper section of the tube.

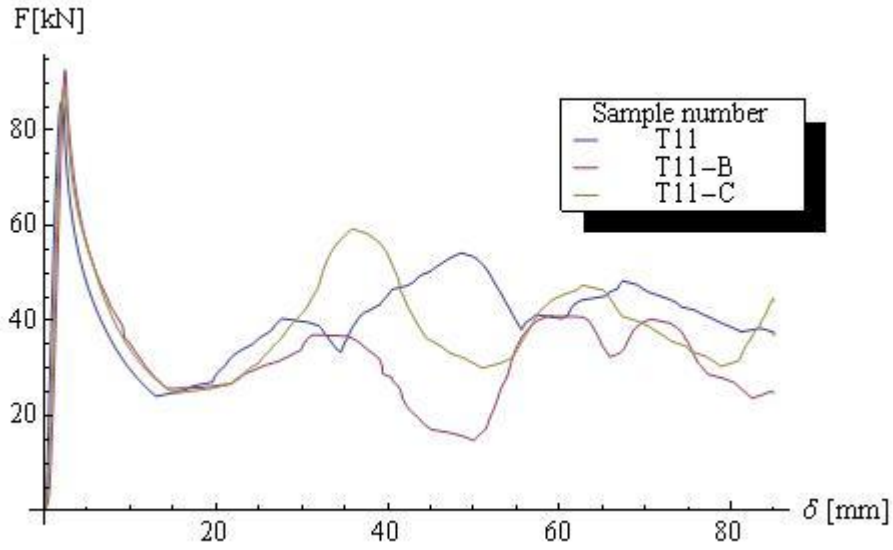

Figure 54: Spot welded hat sections under quasi-static load

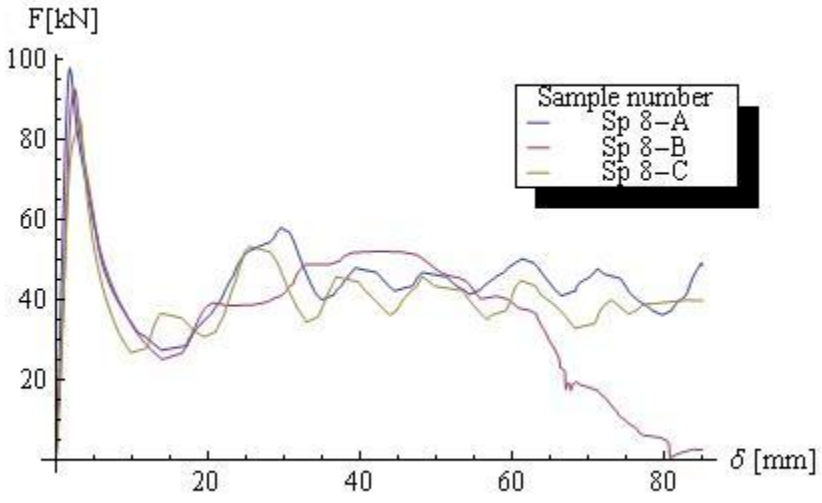

Figure 55: EC-2214 bonded hat sections under quasi-static load

Out of all the tested bonded hats, one important fact must be highlight. For Specimen 8B; the effects on load capacity due to a transition in the deformation from crush to global bending. There was a significant decrease in load carrying capacity (Figure 55) once the global bending mode (Figure 56) was initiated. As was pointed before (Section 2.1) such type of deformation is not only detrimental to the performance of the structure, but could be fatal for the occupants of a vehicle during a crash scenario

Figure 56: Specimen-8B; transition from crushing to global bending during test

Video footage of the test was analyzed and compare to the other tubes to determine why this failure mode developed. During the loading process the tube initially starts a local buckling process at the buckle initiator and progresses to form the first fold, after this the lips of the hats cave in towards the center of the section and propitiate the formation of a second fold at the bottom of the assembly. Once this lower fold initiates the bending moment causes rotation in the section and the load is not going through the central axis any more, introducing eccentricities. At this point the column has started to behave more like a beam. Instants later the induced forces overcome the friction at the bottom causing sliding and increasing the eccentricity of the load even more.

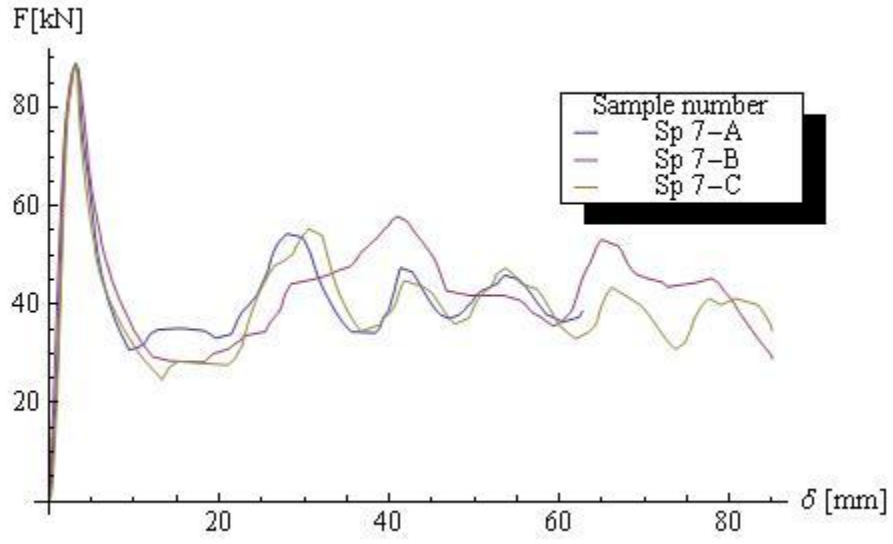

Figure 57: DP-460NS bonded hat sections under quasi-static load

4.2.4 Double channel section results

The tested crush tubes made with channel sections were consistent in the deformation pattern. As it can be seen in Figure 58, there is a clear difference in the overall shape of the crush tube between the ones fabricated using DP-460NS and the ones using EC-2214. The ones using DP-460NS present folds on the top of the tube, asymmetric mode B (Section2.1.2 , Figure 6), while the ones with EC-2214 have the fold pattern developed in the middle length of the tube, asymmetric mode A. The deformation difference was consistent across all the samples and the only explanation has to be tied to the different adhesive material used for the assembly. The stress fields on the joints must be different and therefore the consequent deformation has to be different. To elaborate: On sample C2-A (EC-2214) the adhesive joint failed at both joints at the same distance above the buckle initiator which propitiated the folding process to start on the top. In the case of sample C-7B (DP-460NS), only one of the adhesive seams failed while the other maintained its integrity. Because of this, one of the walls buckled in and propitiated bulging under the buckle initiator were the first fold formed. Once the process was initiated it continued below the first fold.

Figure 58: Deformed channel sections during QS testing. Bonded EC-2214 (right), bonded DP-460NS (left)

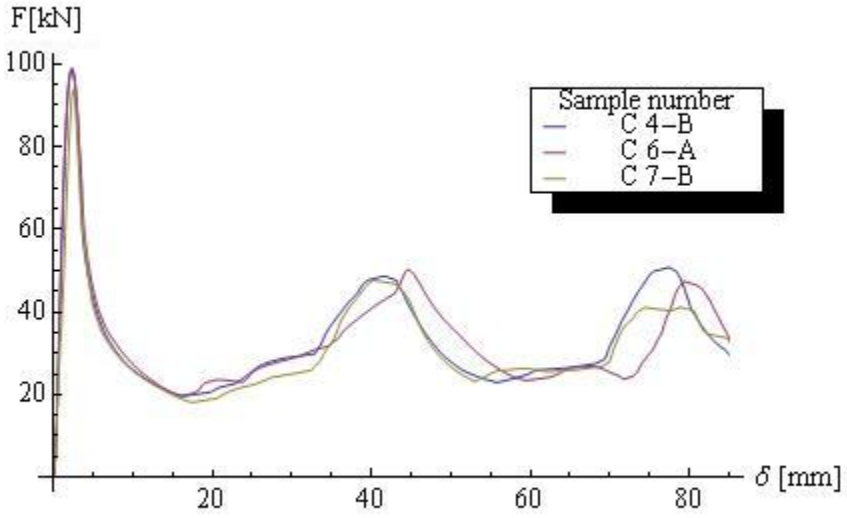

Figure 59: EC-2214 bonded channel sections under quasi-static load

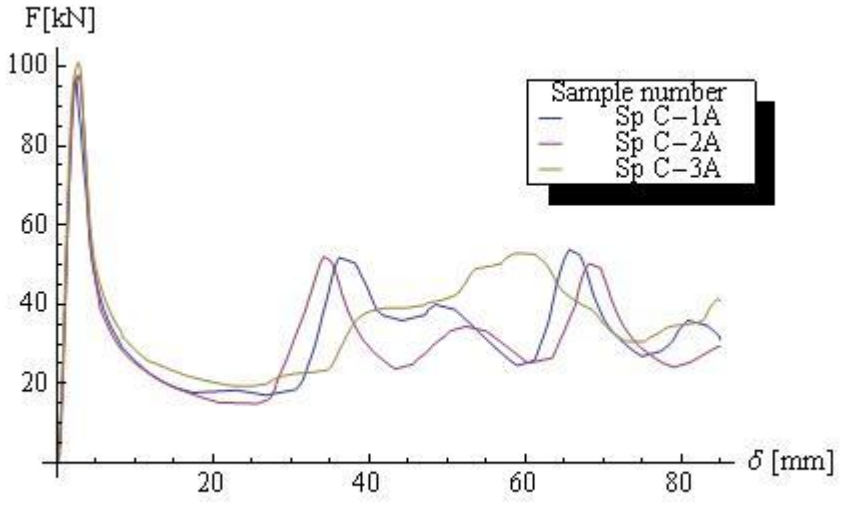

Figure 60: DP-460NS bonded channel sections under quasi-static load

4.2.5 Statistical analysis

In addition to the load-displacement curve, whisker-plot statistical analyses, as first described in 2.1.5, were performed to compare energy absorption, specific energy absorption, mean force, and peak force quantities across structures and bonding adhesive. Information contained in Figure 61 to Figure 64, allows to easily differentiate performance based on section type and adhesive used. Of particular importance is the variability demonstrated by hat sections, notice the spread in the whisker plots in terms of energy absorption and specific energy absorption, regardless of the type of adhesive used.

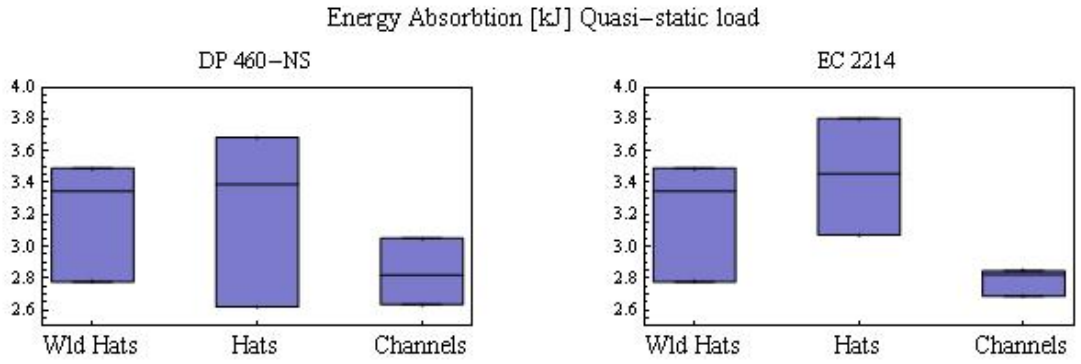

Figure 61: Quasi-static experiment energy absorption whisker plot

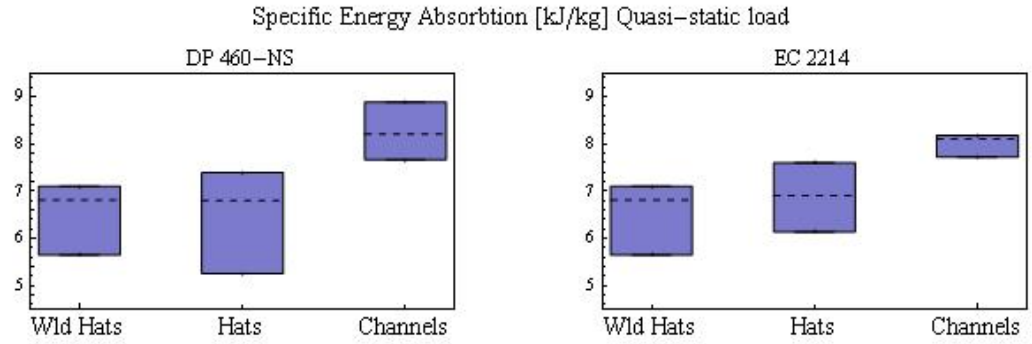

Figure 62: Quasi-static experiment specific energy absorption whisker plot

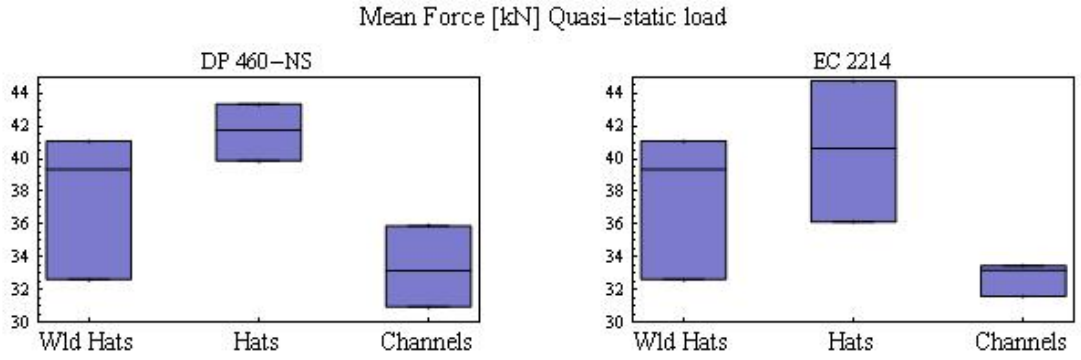

Figure 63: Quasi-static experiment mean force whisker plot

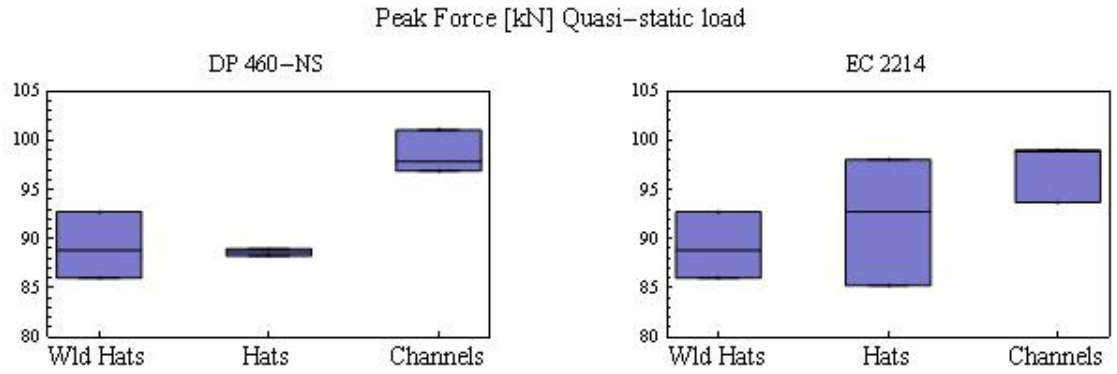

Figure 64: Quasi-static experiment peak force whisker plot

The quasi-static experimental result for the mean load (Figure 63) in the hats (36 to 44 kN) is in good agreement with the calculated mean from theoretical formulas (45.1 kN) using Equation 13. In the case of the channels, the calculated load using the proposed expression (Equation 16) (29.56 kN) seems to slightly under predict the value, using flow stress, if compared to the measured loads (33 kN) in the experiment. The peak loads (Figure 64) fall in the range of the predicted theoretical definition between 2x P_m and 3xP_m, but this relationship seems weak in the case of the channels.
To verify if there were differences between the geometries and joining methods used, a series of t-test were performed using the mean force as value for comparison. Two questions need to be considered:

1. Does one section perform any better than other in terms of the joining method considering welding or bonding (Table 6)?
2. Does a crush tubes made out of hats performs any better than the one made out of channels?

Crush tube joining method	**Hats**		**Channels**	
	T_{obs}	T_{crit}	T_{obs}	T_{crit}
Welded vs.DP-460NS	1.43	2.13	n/a	n/a
Welded vs. EC-2214	0.79	2.13	n/a	n/a
DP-460NS vs. EC-2214	0.43	2.13	0.39	2.13

Table 6: T-test for mean load for differences between joining methods

In the case of the first question, Table 6 illustrates that there were no differences between using a traditional method of joining like spot welding and the use of any of the adhesives used for this work; but if an adhesive were to be selected for the construction of structures under quasi-static loads, the selection of the right structure, hats or channels, is key for the performance of the structure (Figure 62). From Figure 61 to Figure 63is quite clear that there was a performance difference between hats and channels; although the hats developed a higher mean loads, the channels provided the highest specific energy absorption making them a more efficient structure

4.3 Dynamic testing of crush tubes

Crush tube structures as intended to use, are structures subjected to scenarios where strain rate effects cannot be ignored. Dynamic testing of crush tubes using a drop tower was performed to evaluate the structure response during crash scenarios were strain rates are significant.

4.3.1 Equipment

An Instrumented Falling Weight Impact (IFWI) tester, or drop tower, was used to achieve strain rates higher than is possible with an Instron machine.

IFWI dynamic compression testing is used by a number of research groups for a broad range of applications. For example, Abramowicz and Jones [3] used an IFWI to determine the changes in buckling modes for steel tubing subjected to impact velocities. Belingardi [7] used an instrumented drop tower to determine the structural response of built up closed sections to axial impact. For this project, a Rosand (IFWI) drop tower, Figure 65, in conjunction with a high speed video system were used to obtain force-displacement diagrams of crush tube structures subjected to axial dynamic impact.

Figure 65: Waterloo University IFWI

The drop tower consists of a falling weight guided by rails, which ensure that the striker falls completely vertical, and a load cell located below the specimen that measures the load during the event. Specimen deformation can be measured in a number of ways. In this case the displacement was obtained by double integrating the acceleration curve. The acceleration values were obtained out of the force data being divided by the mass of the impactor. Analysis of high speed video footage was used to verify that the displacement data generated by the drop tower and the measured impact velocity prior to impact were accurate. A schematic diagram of the test setup is shown in Figure 66.

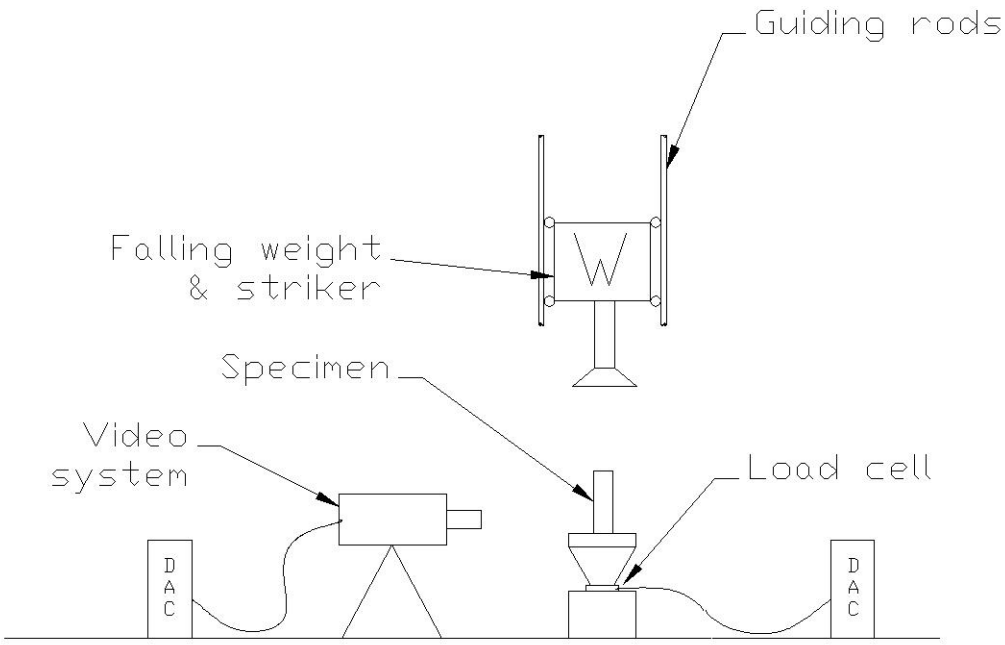

Figure 66: IFIW schematic set up

The IFWI system measures impact velocity using optical laser techniques, in which a gate is positioned to measure the velocity just prior to impact. After the drop is initiated, the falling weight and striker moves down, and the gate crosses the laser. The tower counts the time taken for the laser to become visible again. Since the length of the gate is known, the velocity can be calculated.

4.3.2 Experiment

A fixed mass of 56.18 kg was dropped from a height of 2.73 m to impact the sample. By conservation of energy an impact velocity of 7.31 m/s should be achieved. The IFWI system consistently measured an impact speed of 7.24 m/s, which was corroborated by high speed video.

The samples consisted of crush tubes with the same geometries as described in 4.2.2. The sections build out of hats included an additional notch (Figure 67). This notch was required in the simulations geometry for numerical stability and initiation of the folding process. The experimental samples were modified accordingly so similitude between numerical model and experiments was maintained. No modifications were necessary for the channels.

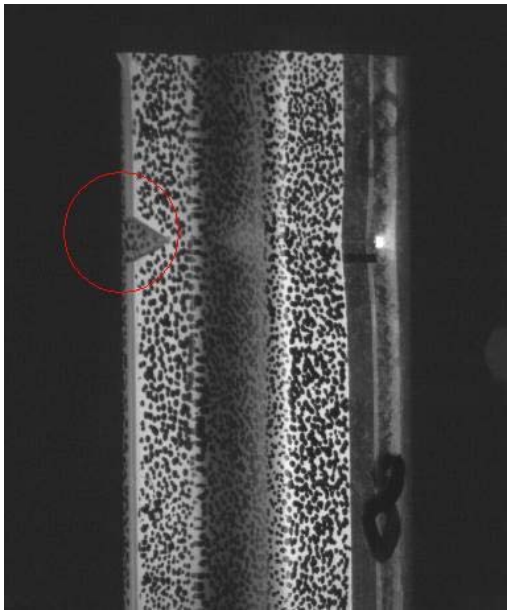

Figure 67: Hats notch detail

4.3.3 Double hat section results

Similar to the quasi-static experiments, dynamic testing results are presented in the form of load-displacement curves, and whisker plot analyses are used to compare absorbed energy, specific energy, mean force, and peak force across samples. Besides the statistical analysis, results for t-test on the mean force are also presented.

Figure 68: Dynamic impact deformed hats. Spot welded (left), bonded DP-460NS (center), and bonded EC-2214 (right)

As with every kind of dynamic testing there was some degree of noise content in the signals, this is reflected in the form of oscillations in the force-displacement diagrams; but across all the range of testing, the response of the crush tubes were very consistent for each geometry.

From Figure 68 it can be seen that the hats did not developed a folding pattern as did happen during the quasi-static testing. This can be explained by:

1. The additional notch that was added in the joined lips of the member to match the geometry of the simulations (Section 4.3).
2. The deformation in the cross section walls (Figure 69) caused by the buckle initiator indentation process. Although this deformation was present during the quasi-static testing, due to the nature of the impact event, the initial deformations in the geometry were more relevant, especially in the case of the hats.

As a consequence of these differences, there must be additional stresses in the bond that impinges the adhesive layer to carry the load causing debonding which in term prevents the development of a traditional folding pattern. There was an incipient fold under the deformed area but the impact event runs out of energy before the formation of this second fold can progress.

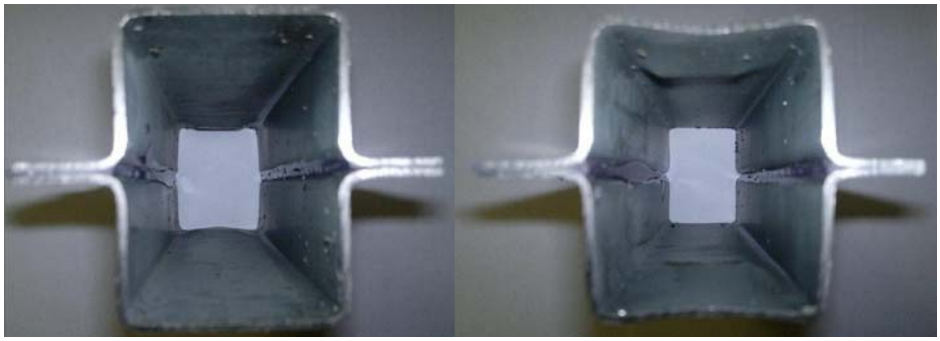

Figure 69: Cross section indentation process deformation, not indented (left), after indentation (right)

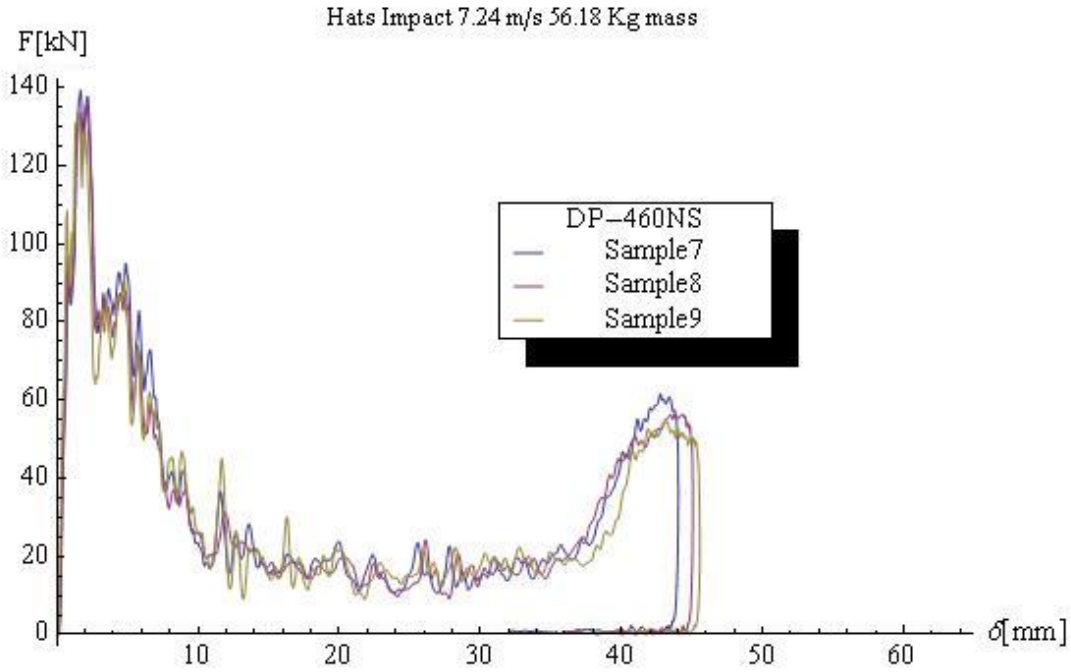

Figure 70: Bonded hat sections DP-460NS

There is a consistent rise at the end of the force-displacement diagram, starting at around 38 mm of compression, in all of the bonded hat sections (Figure 70 and Figure 71) which were barely noticeable in the welded hat sections (Figure 72). This end rise corresponds to the consolidation of the deformed top and the subsequent increase in load to start forming a new fold.

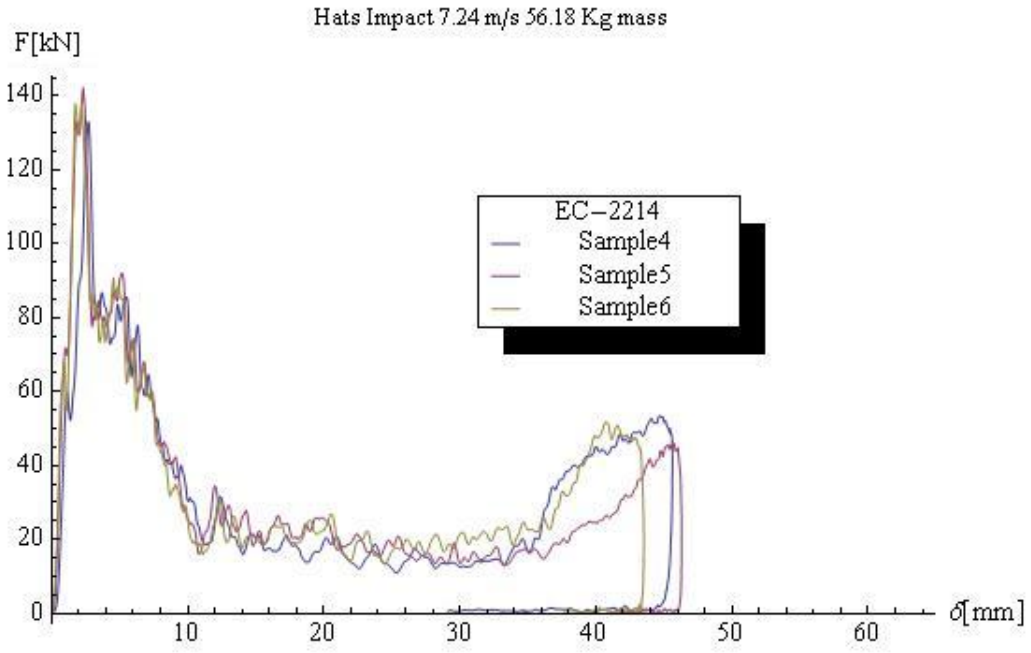

Figure 71: Bonded hat sections EC-2214

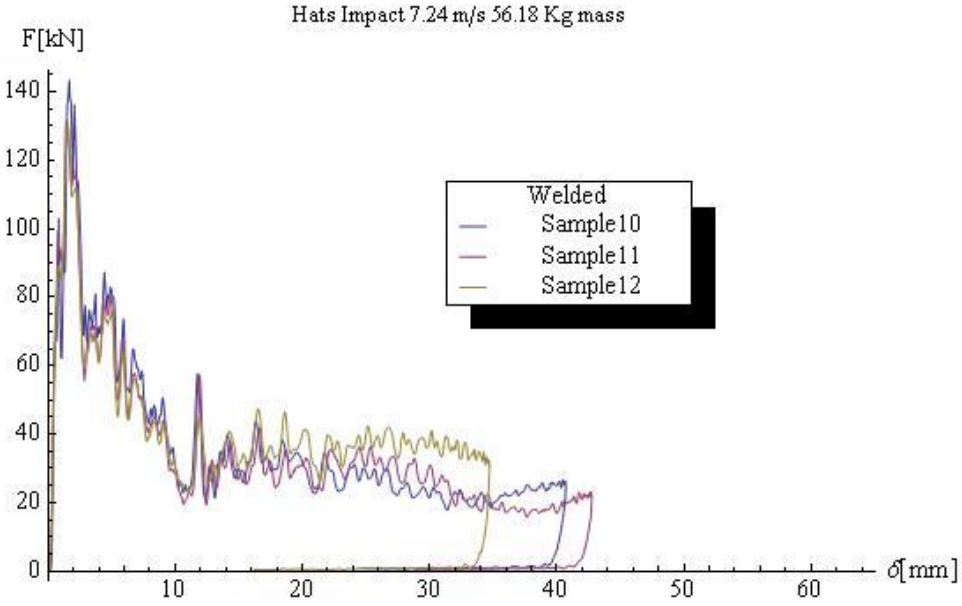

Figure 72: Spot-welded hat sections

In the case of the welded structures the energy was dissipated in a different manner, the lip in the welded structure did not open keeping the integrity of the cross section thus allowing for higher forces during the event (Figure 73), at the end of the striker stroke there was not enough energy to start the formation of a new fold. Compare the force mean value at the valleys between welded hats, around 30 kN, and the bonded structures, approximately 18 kN. We can say that during this time of the deformation process more energy was being dissipated on the welded hats than in the bonded hats.

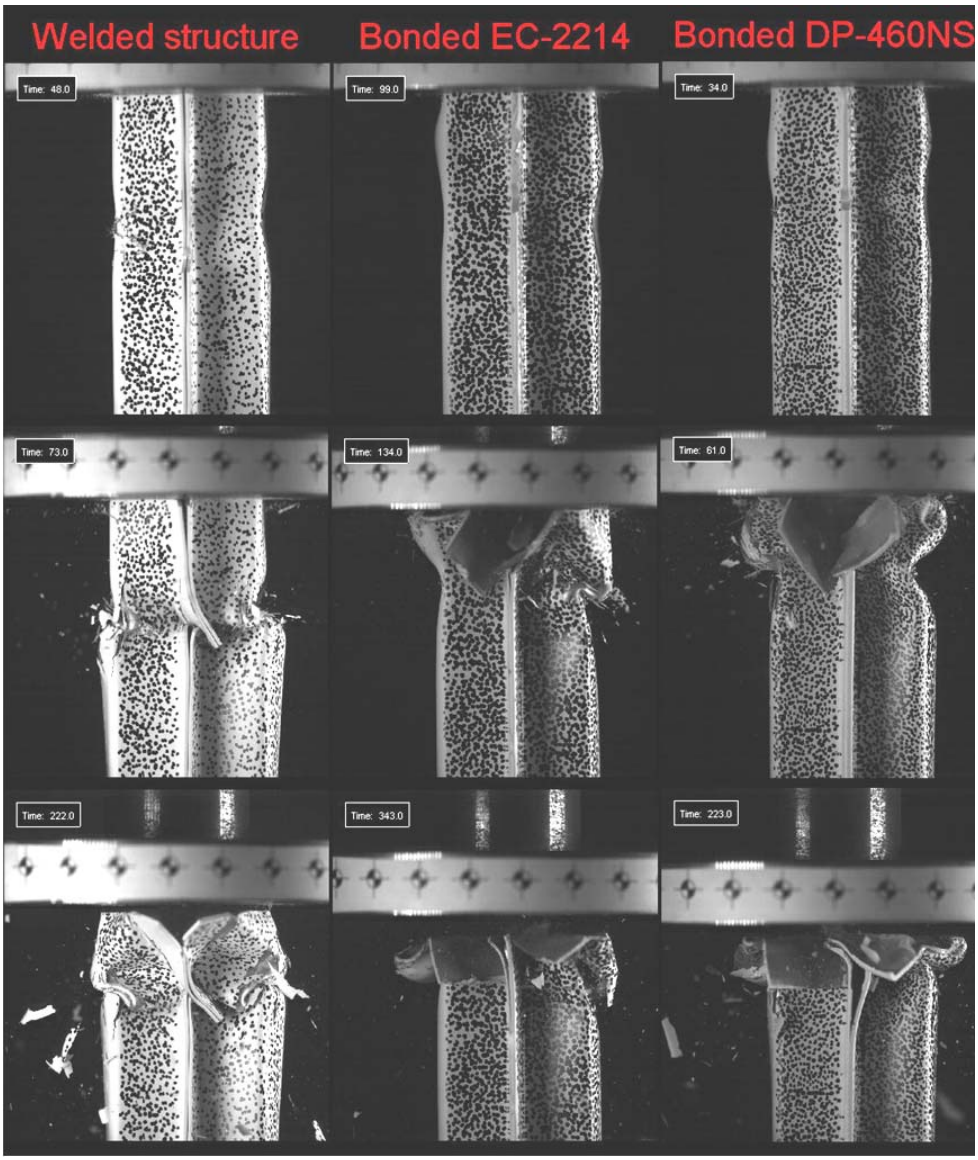

Figure 73: Deformation history of bonded hat sections during impact event (time progresses top to bottom)

4.3.4 Double channel section results

Figure 74and Figure 76 show the expected folding pattern developed in the channels. During the quasi-static testing there was a clear difference in folding modes between the sections constructed with each adhesive. However, in the dynamic testing the response was similar for both adhesives.

.

Figure 74: Dynamic impact, channels bonded with DP-460NS

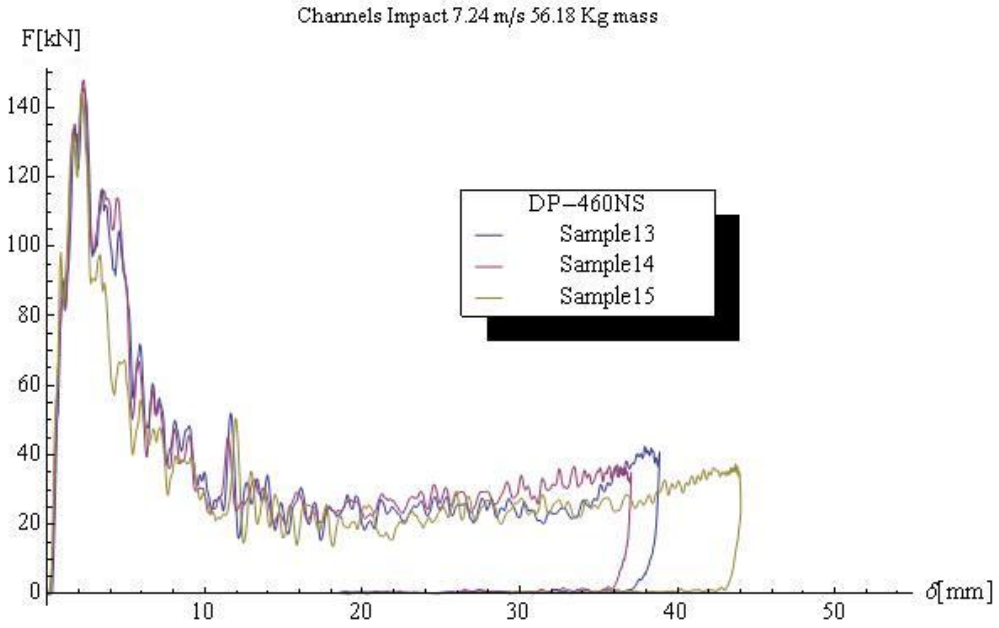

Figure 75: Bonded channel sections DP-460NS

Figure 76: Dynamic impact, channels bonded with EC-2214

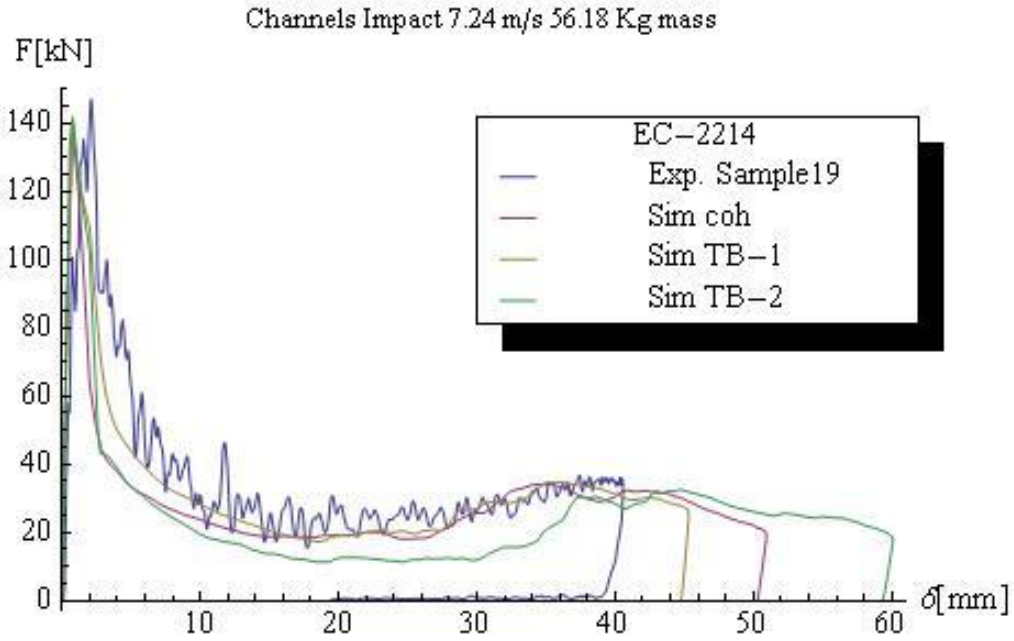

Figure 77: Bonded channel sections EC-2214

From the totality of the double channel crush tubes, sample 13 had a different folding mode, asymmetric mode B (Section 2.1.2), if compared to all the other structures, which developed asymmetric mode A in the folding pattern.

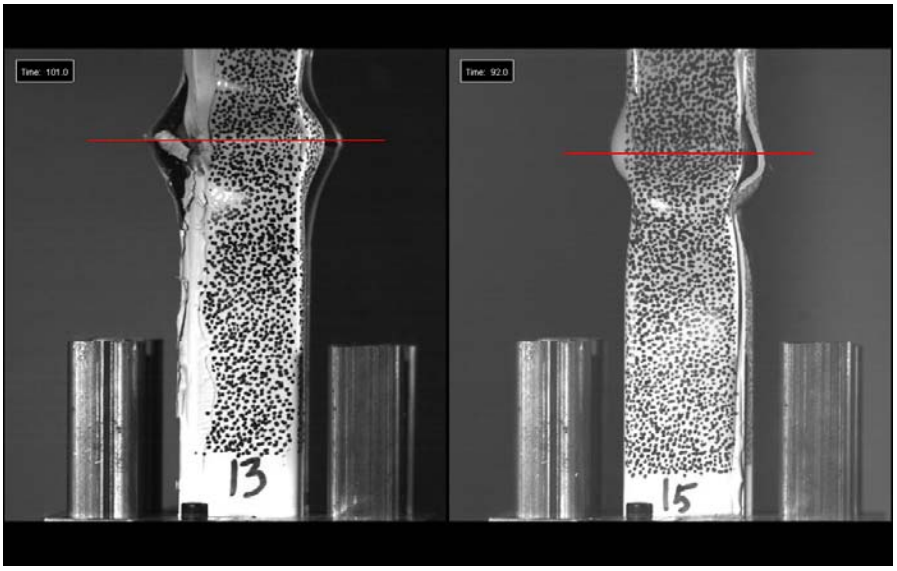

Figure 78: Dynamic impact comparison, sample 13 vs. sample 15

Sample 13 develops a different folding pattern because of symmetry in the deformation, in Figure 78 one can see that for sample 13 the fold hinges on each side and the buckle initiator were on the same plane (red line) while on sample 15 only one fold hinge aligns with the buckle initiator; the other hinge was well below the other one. Since the geometry was quite consistent in the double channel crush tubes, the only possibility to explain this discrepancy lies in the influence of the adhesive joint. Notice that samples 14,15,19,20 and 21 show similar debonding patterns which is not apparent in sample 13.

4.3.5 Statistical analysis

The dynamic experimental result for the mean load (Figure 81) in the hat sections (23 to 33kN) was lower than the predicted mean (53.67 kN) calculated using Equation 14. In the case of the channel sections, no equation was develop for the dynamic case, but if one scales the previously calculated quasi-static mean load (29.56 kN) using the Cowper Symonds relationship described by Equation 17, one can obtain an approximation for the expected mean load. In this case the calculated value (34.72 kN) seems to agree quite well compared to the measured loads (33 to 39 kN) in the experiment. The peak loads (Figure 82) do not fall in the range of the predicted theoretical definition; defined as a value between $2xP_{md}$ and $3xP_{md}$.

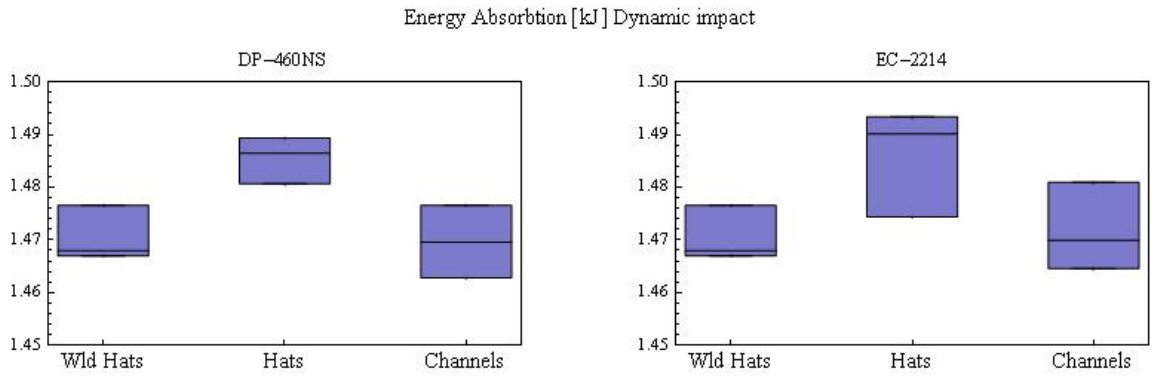

Figure 79: Dynamic impact experiment energy absorption whisker plot

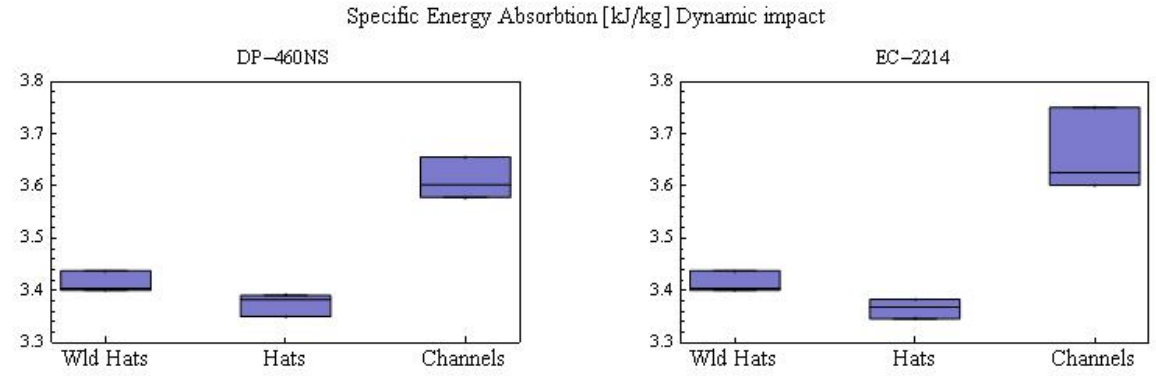

Figure 80: Dynamic impact experiment specific energy absorption whisker plot

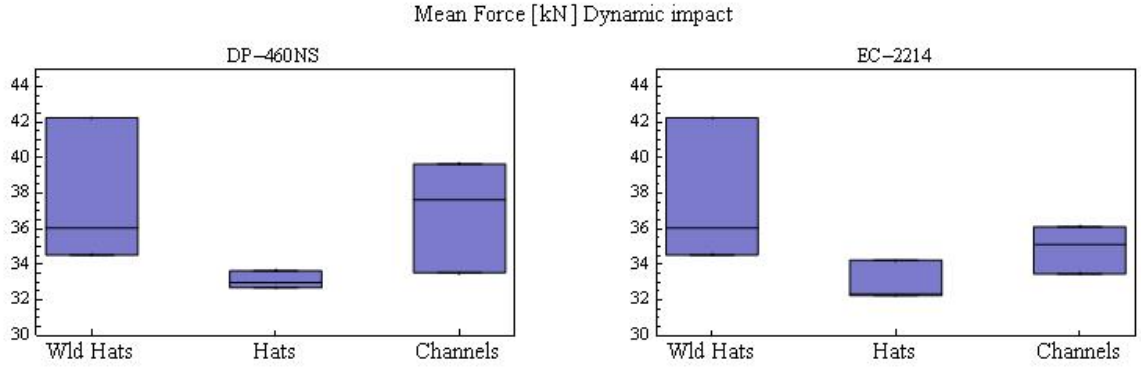

Figure 81: Dynamic impact experiment mean force whisker plot

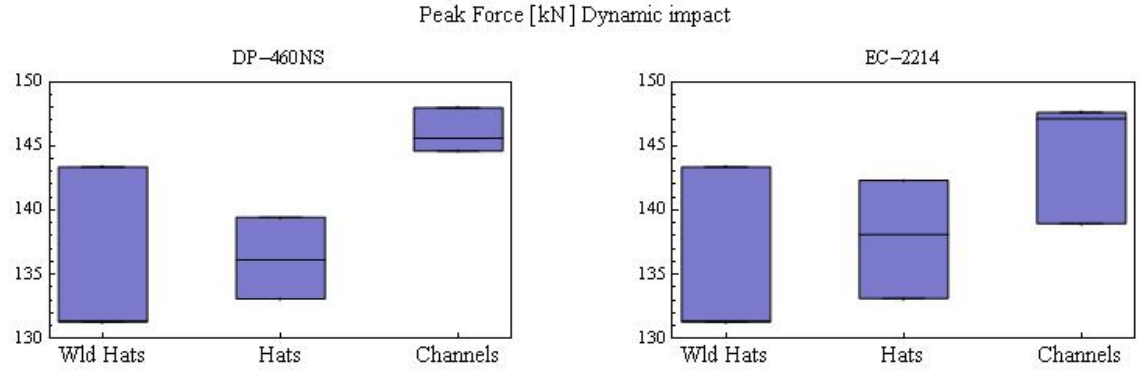

Figure 82: Dynamic impact experiment peak force whisker plot

The measured mean forces for different geometries and joining methods were compared using a t-test. Specifically, the performance of the adhesive (Table 7) and section types (Table 8) were compared.

Crush tube joining method	Hats		Channels	
	T_{obs}	T_{crit}	T_{obs}	T_{crit}
Welded vs.DP-460NS	1.89	2.13	0.23	2.13
Welded vs. EC-2214	1.91	2.13	1.09	2.13
DP-460NS vs. EC-2214	0.23	2.13	1.04	2.13

Table 7: T-test on mean load of dynamic samples for differences between the joining methods

In the case of dynamic events there were no differences between using a traditional method of joining like spot welding and the use of adhesives (Table 7) in terms of mean loads. The welded hats seemed to perform better than the bonded hats according to Figure 81, but statistically there were no significant differences even when compare against the bonded channels.

There were no differences between the use of one adhesive or the other, as shown in the last row of Table 7, but the selection of the right type of geometry seems to be key, since performance differences between hats and channels seem again significant (Figure 79 and Figure 80). Although the calculated values for the T-test as shown in Table 8 confirm that there was no significant statistical difference in terms of mean forces; it could be more useful to look into the specific energy to determine if there were any advantages to use a double hat or a double channel section, clearly the channels seem to outperform the hats manufacture by welding or bonding.

Adhesive	Hats vs. Channels	
	T_{obs}	T_{crit}
DP-460NS	2.11	2.13
EC-2214	1.95	2.13

Table 8: T-test on mean load of dynamic samples for differences between geometry

Adhesive	Hats vs. Channels	
	T_{obs}	T_{crit}
DP-460NS	3.75	2.13
EC-2214	6.18	2.13

Table 9: T-test on specific energy of dynamic samples differences between geometries

From Table 9 it's clear that there were significant differences in the specific energy absorbed between one structure and the other; using channels have a significant advantage if one wants to obtain a lighter overall structure.

Was hard to tell if there was any significant difference between the specific energy for double channels that use one adhesive or the other (Figure 80).This was confirmed by the results of a t-test (Table 10) where the two means are statistically indistinguishable from the other, so there is no clear advantage that can hint that one adhesive outperforms the other.

Adhesive	Channels	
	T_{obs}	T_{crit}
DP-460NS vs. EC-2214	1.15	2.13

Table 10: T-test on specific energy of dynamic samples for differences between adhesives

Unfortunately the equipment used did not have enough energy available to continue the folding process; it is possible that if the deformation process were to be continued a more significant difference in performance between the adhesives could be identified.

4.4 Quasi-static vs. dynamic results

As previously mention there were some differences in the behavior of the structure under quasi-static and dynamic loading. To fully appreciate the differences between one type of test and the other, figures for each case and material are presented and briefly discussed.

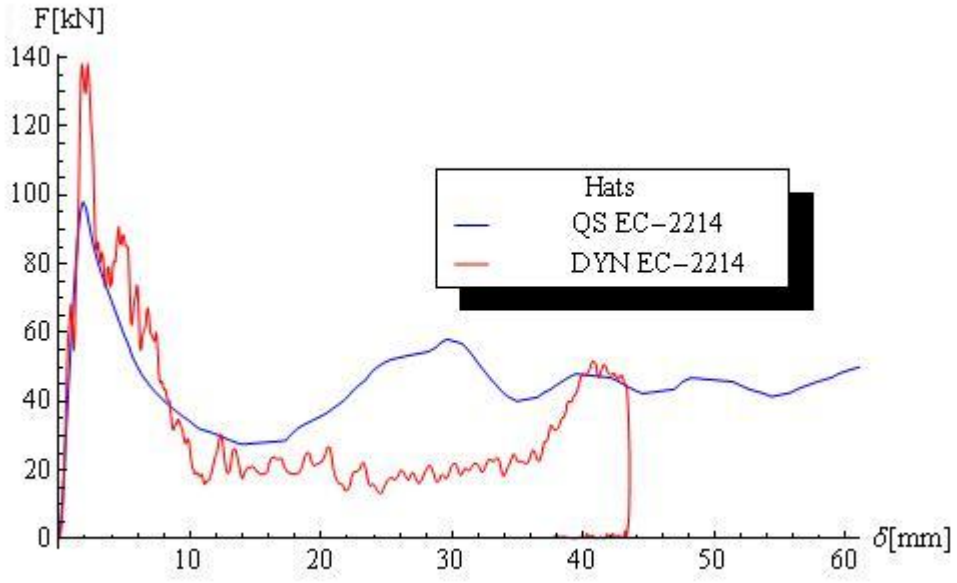

Figure 83: Quasi-static vs. dynamic; hat sections bonded EC-2214

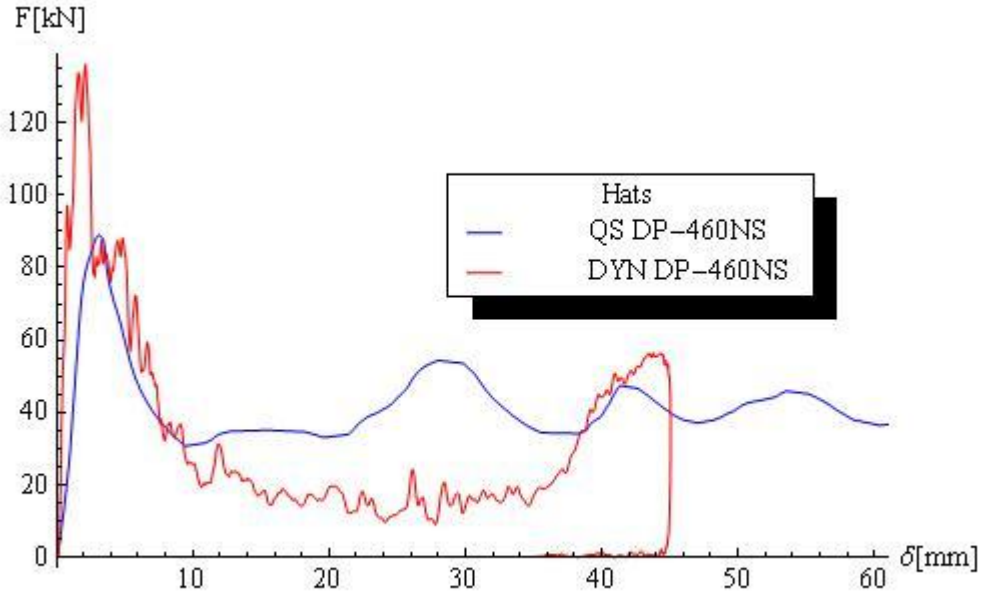

Figure 84: Quasi-static vs. dynamic; hat sections bonded DP-460NS

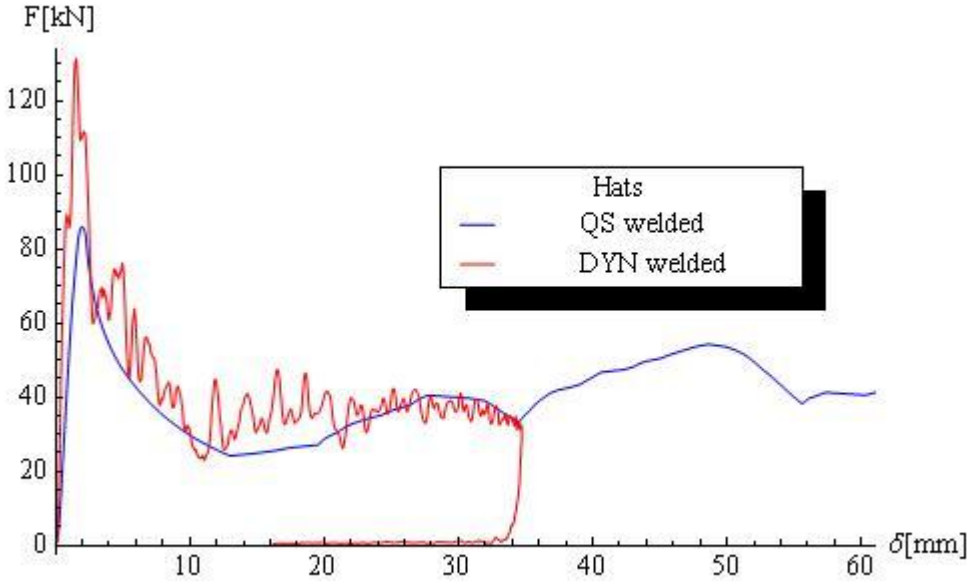

Figure 85: Quasi-static vs. dynamic; welded hats

Under dynamic conditions, the hats force trace do not follow the trace under quasi-static load (Figure 83 and Figure 84), as it was done by the channels (Figure 86 and Figure 87). This discrepancy can be explained by the early failure of the adhesive joint at the top of the hat during the dynamic event. From the figures describing the channels, one can infer that once the peak load was reach the curve should follow a similar trend for both events; but this is only true because there was not much difference in the strain rate between one event and the other. The impact velocity for the dynamic event was not enough to cause a significant shift in the material properties due to strain rates. The peak force is clearly differentiated between one event and the other, which can be explained again by strain rate effects.

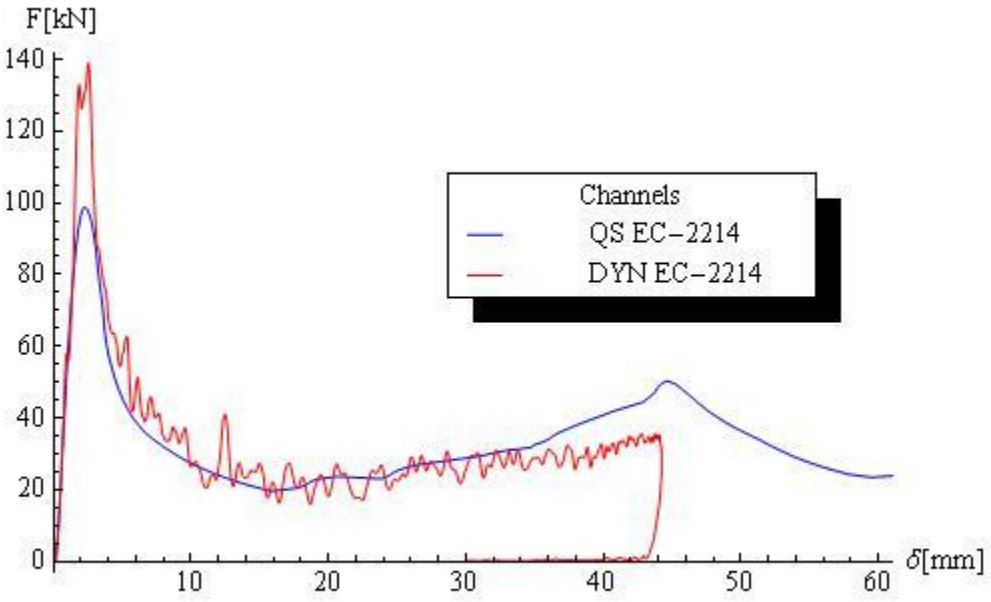

Figure 86: Quasi-static vs. dynamic; channel sections bonded EC-2214

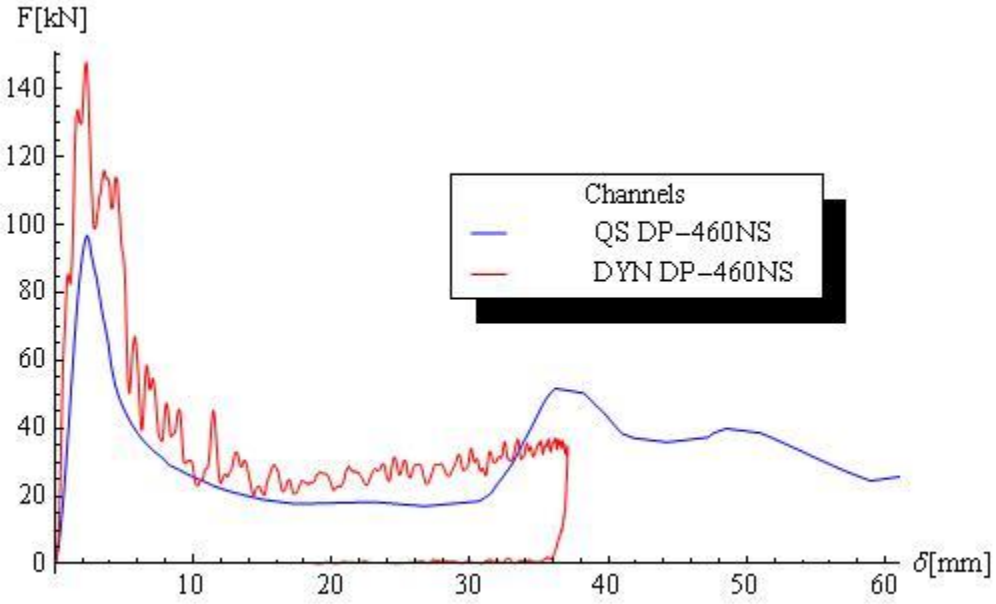

Figure 87: Quasi-static vs. dynamic; channel sections bonded DP-460NS

Another important feature to identify was the formation of the folds. According to the figures one can expect that between the dynamic event, impact at 7.25 m/s, and the quasi-static loading, the formation of the folds and locations of them should be indistinguishable. If one revises the basic folding element for symmetric collapse (Figure 5), the energy absorption (U) can be described by the following equation [4]:

$$U = \sigma_o \frac{t^2}{4}(8.88\, H\, \frac{b}{t} + \, 2\pi C + 4.6\, H^2/b)$$

Equation 26: Energy absorption of a single folding element

As it can be seen the energy absorption is highly dependent on the flow stress and the geometry of the cross section; therefore this generalization is not accurate (location of folds) since the yield stress would be once again a value highly dependent on the strain rates. Another way to see the difference would be to use the same amount of energy for a dynamic event and a quasi-static one and use Equation 26 to find the value of H, the length of the folding element. Since the yield stress for one and the other is not the same, the length of the folding element cannot be the same everything else being equal.

Chapter 5
Simulation of crush tube experiments

Numerical modeling has become an important tool for the design and development of engineering systems and components. With current computational resources, one can implement models powerful enough to accurately predict product performance, and thus minimizing expensive prototype testing. This dramatically reduces design cycle times, and in turn lowers overall development costs.
Several parameters must be defined in order to produce accurate numerical results. On the one hand, a suitable constitutive formulation is required to accurately describe material behavior; while on the other, numerical parameters, such as element formulation and mesh size, must be considered to balance calculation time.
As previously presented in section 2.5, a cohesive element was implemented and then validated by simulating the behavior of each adhesive formulation in a double cantilever beam (DCB) test. The cohesive element model was used to describe crush tube behavior under axial loading. Also the two previously describe Tie-Break elements (section 2.5.5) were implemented to reduce computation time. The simulations emulated the experiments described in Chapter 4.

5.1 Preliminaries

In order to use numerical analysis as a predictive tool, one has to be sure that the model used to describe the intended problem can provide accurate and reliable answers under required load conditions. Not only must the constitutive models that describe the materials be selected correctly, but the implementation of the problem must also approximate the actual physics of the scenario as accurately as possible. In addition, other factors such as mesh size and type of element must be considered to obtain accurate answers. For the present work, square shell elements with mesh sizes of 2 and 3 mm were selected to represent the steel hats and channel sections (respectively) used to assemble the crush tube structures. These element sizes where determined from a convergence analysis (Figure 88) that was performed to predict the behavior of crush tubes under axial impact load as described by Tarigopula et al. [40]. Other authors have previously studied crush tubes under axial impact load. For example, Langseth [27, 28]and Tarigopula et al [40]studied square and welded top hat sections made out of aluminum or steel, and Williams [46] analyzed the numerical model response for hydro-formed aluminum round tubing.

For this work, a square section experiment was first used to determine the main mesh size necessary to accurately describe the problem. This knowledge was then applied to the analysis of adhesively bonded structures. More details can be found in Appendix C

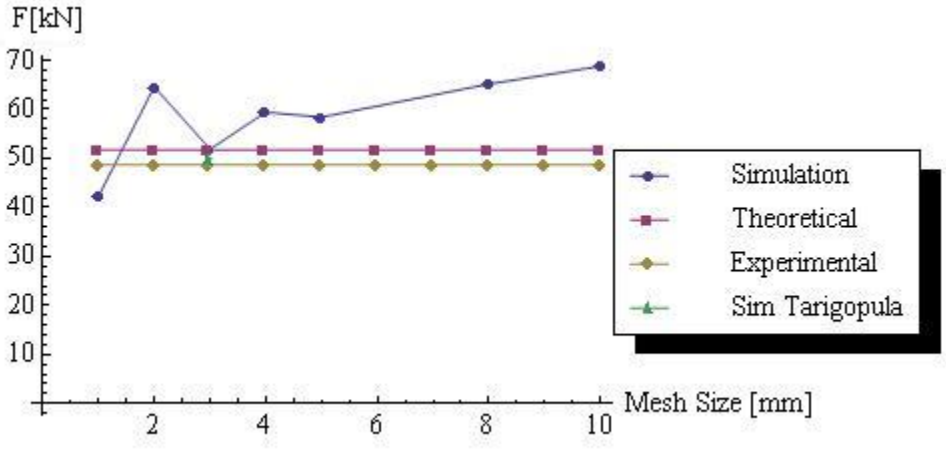

Figure 88: Mesh size effects on simulation calculated mean force

5.1.1.1 Cohesive elements

Cohesive elements were used to represent the behavior of adhesively bonded material in assembled crush tubes. Specifically, the adhesive was represented by a single layer of solid elements, with a general cohesive material. Lap-Shear and tensile test results were used to determine the traction-separation curves (Section 2.5.3), which defined cohesive elements for both DP-460NS and EC-2214 materials. LS-DYNA cohesive element card definitions for each adhesive can be found in Appendix D section D.1.

5.1.1.2 Tie-Breaks

The two Tie-Break implementations (Section 2.5.5) were also used to simulate the quasi-static and dynamic impact scenarios for the crush tubes. The LS-DYNA cards are presented in Appendix D, section D.2

5.1.1.3 Steel material

A material model that can describe linear-elastic deformation at low strains and plastic deformation with strain hardening after yield and at the same time incorporate the effects due to strain rate was needed to represent the steel material in the numerical code. Mat 24 in LS-DYNA was selected for

the task since it can represent materials by the definition of arbitrary stress vs. strain curves at different stress rates or by defining a base curve for the plastic behavior and include strain rate effects by using the Cowper-Symonds model (2.1.4.1). The material model was implemented by defining a base curve for the quasi-static behavior, by selecting points in the true stress vs. plastic strain curve (Figure 89).

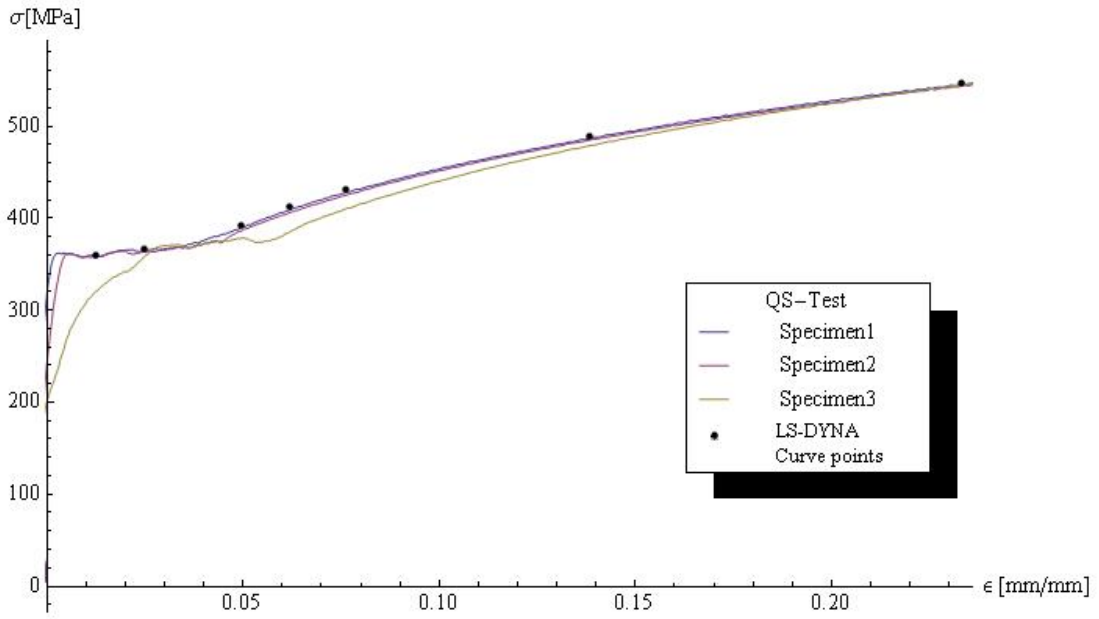

Figure 89: Steel material, true stress vs. plastic strain curve from Quasi-Static testing

As discussed in Section 2.1.4 some materials manifest dynamic effects when subjected to fast loads; testing data was fitted to the Cowper-Symonds model (Equation 7) to capture the strain rate effects. Since this material presents a characteristic high yield point followed by a drop in the load, two different fits to the stress-strain data were performed.

First, a model that was biased towards the yield point (Equation 27) was used to describe the steel material behavior under dynamic loading for this particular steel.

$$\sigma_o^d = 367.2\,(1 + \left(\frac{\dot{\varepsilon}}{306.31}\right)^{1/3.61})$$

Equation 27: Cowper-Symonds equation bias towards yield for steel material (fit #1)

The model was compared against the data obtained by testing as illustrated in Figure 90, with good correlation between model and experimental data for the yield points.

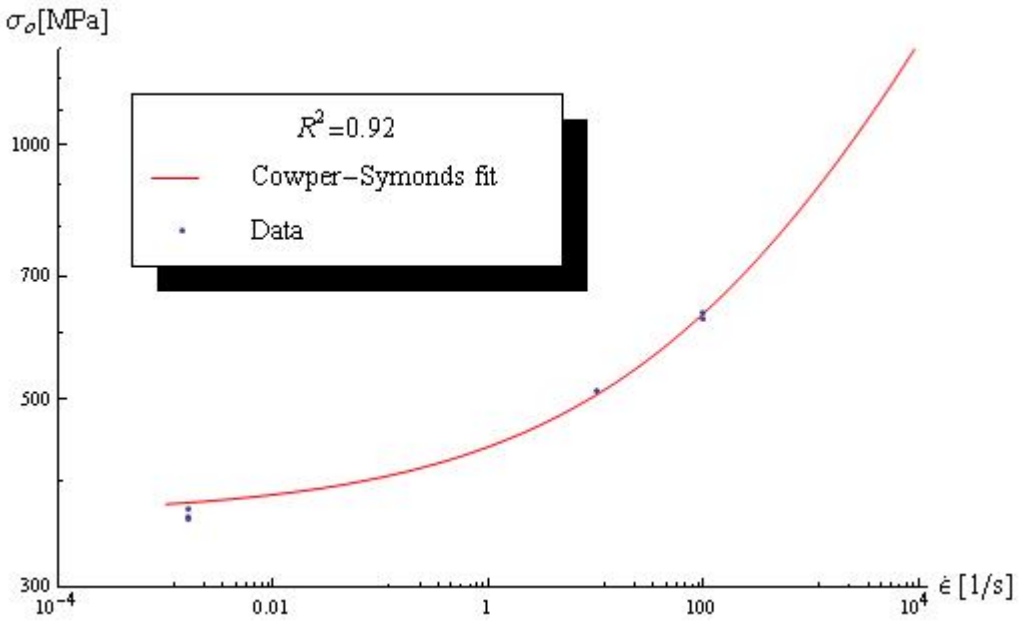

Figure 90: Cowper-Symonds model, fit#1 vs. data

A second fit was performed considering all the information that describes the stress-strain curve at the different strain rates and disregarding the yield peak.

$$\boldsymbol{\sigma_o^d = \sigma(1 + \left(\frac{\dot{\varepsilon}}{77241}\right)^{1/4.14})}$$

Equation 28: Cowper-Symonds equation using all data set for steel material (fit#2)

The R^2 value for this fit was lower (0.53, Figure 91); however the fit was in reasonable agreement with the data.

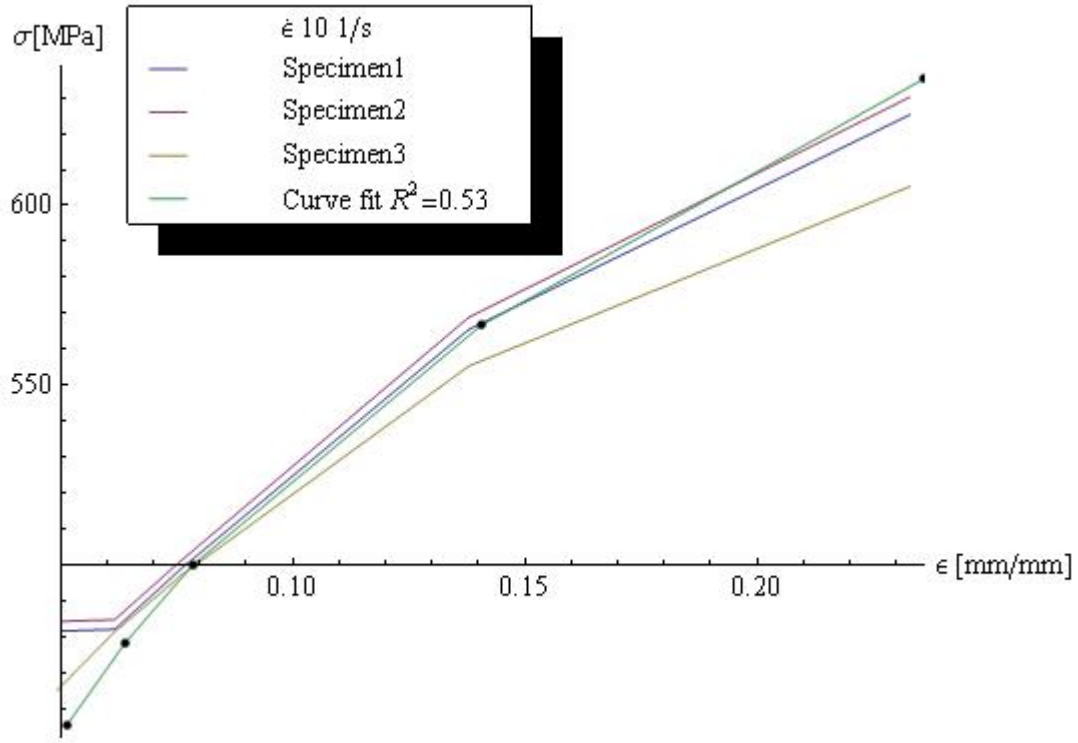

Figure 91: Cowper-Symonds model, fit#2 vs. data

A third option, which will be referred as fit #3, is to provide the material behavior by using a table of strain rates; for each specified strain rate in the table a curve of true stress vs. plastic strain must be provided. Data from the quasi-static test as well as 10 and 100 1/s strain rate was provided to build this option. Data for 1000 1/s was included by extrapolating the Quasi-Static data using curve fit #2.

Each of the models was evaluated using a simulation of the tensile test (Figure 92) at the rate of 10 1/s and the resulting stress-strain curve compared to the experimental data to define which model was best (Figure 93). The selection of the material model is important since it describes the material behavior during deformation. By example, the curve fit#1 can describe very well the peak load generated during an impact, but it may over predict the mean force during the rest of the event. In an energy absorbing structure used during an automotive accident scenario, capturing this peak force is relevant since this will be directly related to the maximum acceleration that an occupant may experience during a crash. A further review of the material model was done by comparing the simulation of a crush tube (Figure 94) using the different curve fits against the experimental results. Curve fit #1 as previously described over predicts the strength of the material but is useful to capture

the peak load, curve fit#2 under predicts the peak load; fit #3 is a good compromise to describe this material.

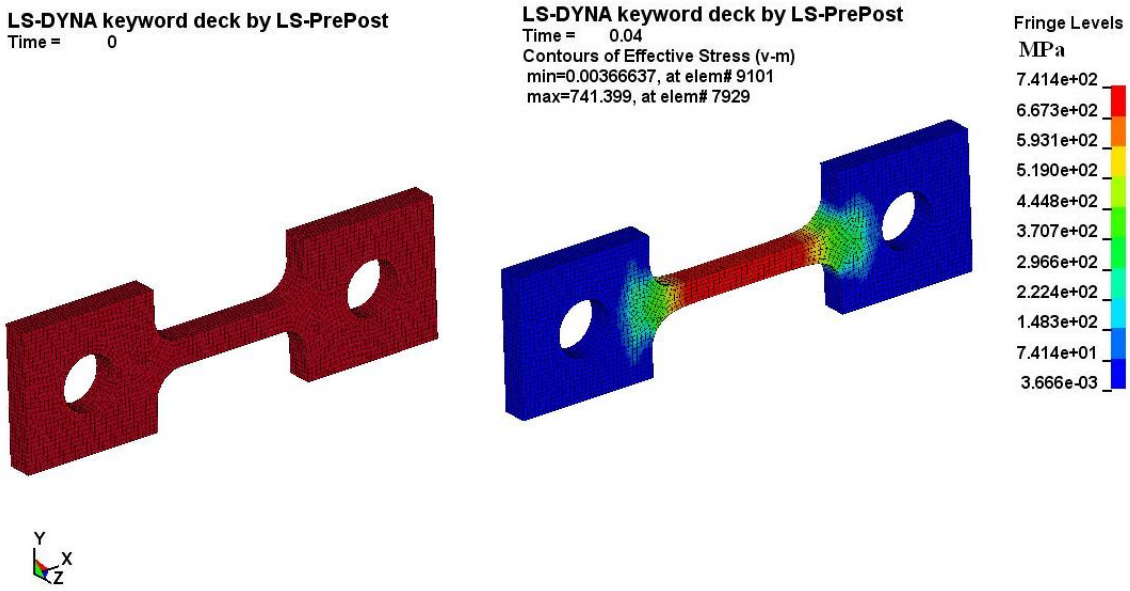

Figure 92: Steel material, tensile test simulation at 10 1/s strain rate

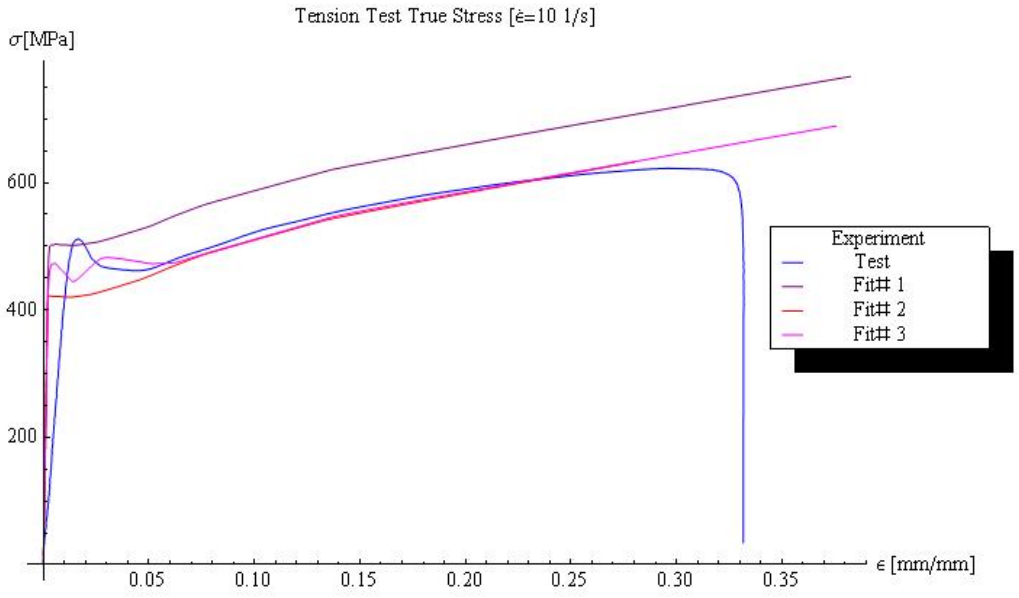

Figure 93: Steel material, material model response vs. experiment at 10 1/s strain rate

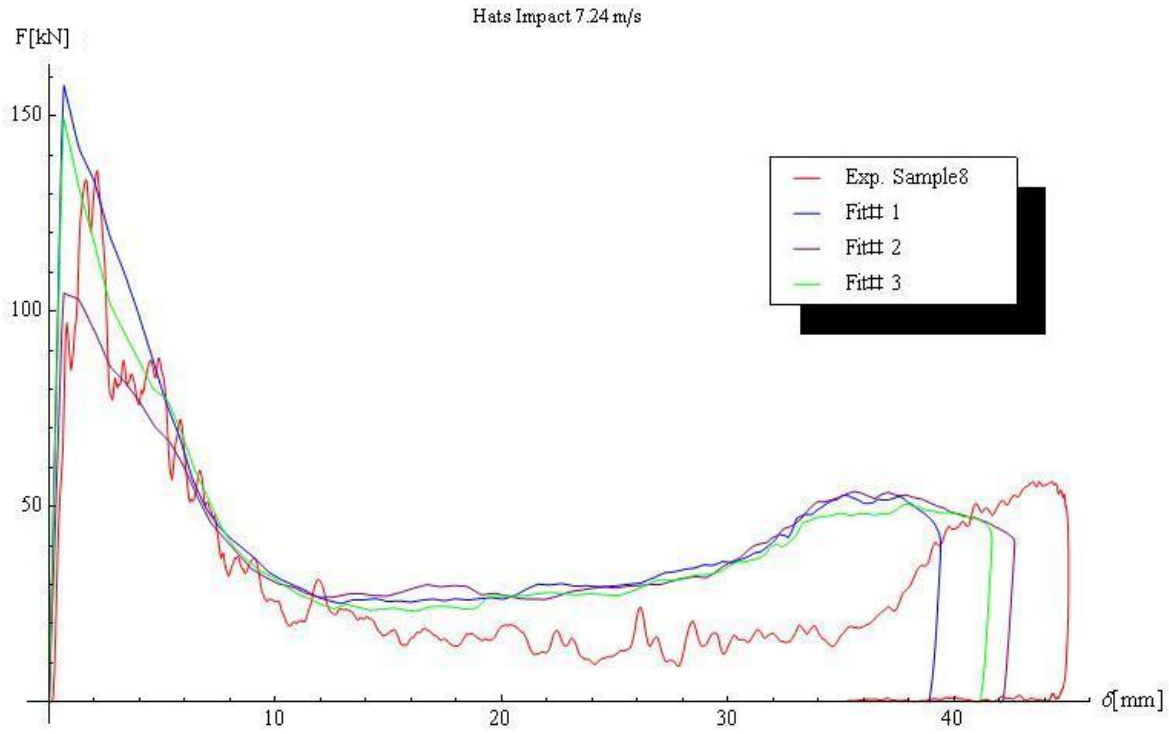

Figure 94: Crush tube simulation vs. experiment using different material models for steel

5.2 Quasi-static simulation results and validation

In this section, experiments that describe the crush behavior of energy absorbing structures under quasi-static load conditions are replicated using LS-DYNA numerical code. Both cohesive elements and tie-break implementations were used to represent the adhesive bond in the crush tubes.

The LS-DYNA numerical model used an artificial time scale and the simulation load rates were multiplied by a factor of 1000 to expedite the simulation time. With this in mind, one must ensure that the material model selected does not include strain rate effects; since the high rates of loading will change the simulation response and the results would not reflect quasi-static conditions. The Instron universal testing machine described in Chapter 4 was represented in the simulation using a rigid plane moving in the vertical direction, as shown in Figure 95. During quasi-static simulation, the plane comes in contact with the tube, which is restricted from movement at its base, and applies compression loading. Eventually the load causes plastic collapse of the section at the buckle initiator, as depicted in Figure 96 to initiate the folding process.

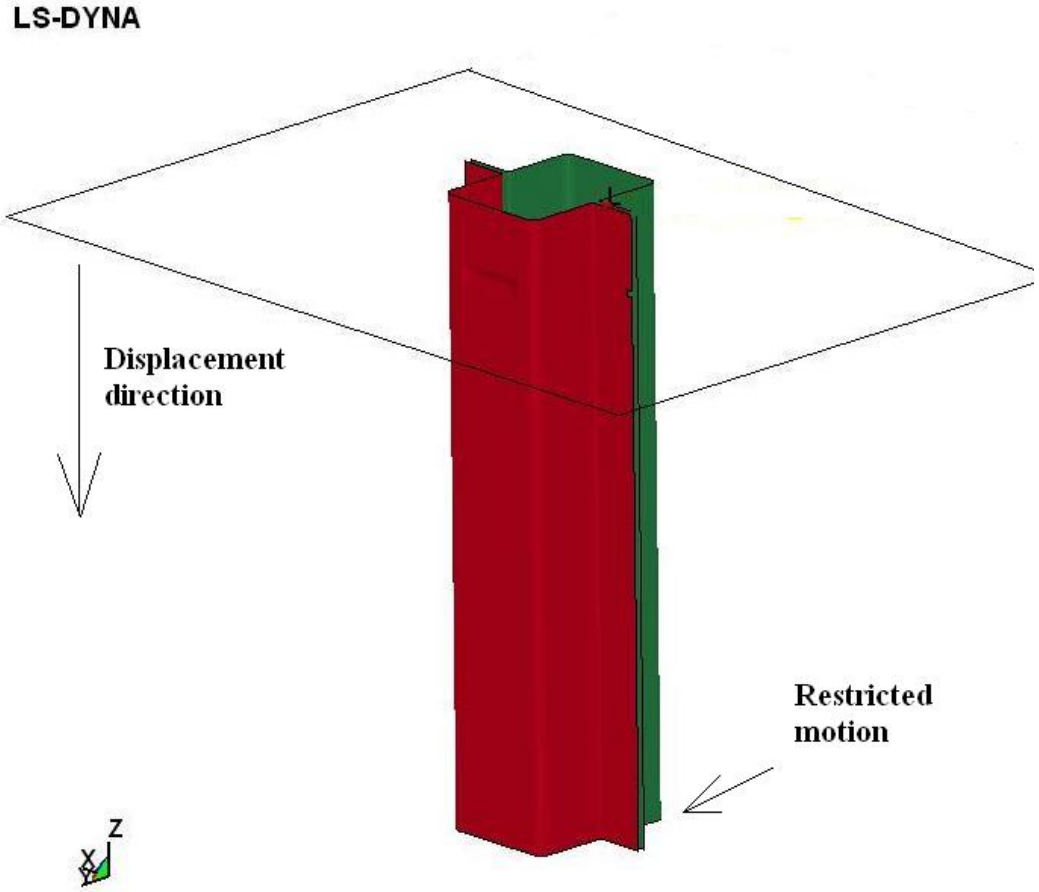

Figure 95: Quasi-static simulation of crush tubes

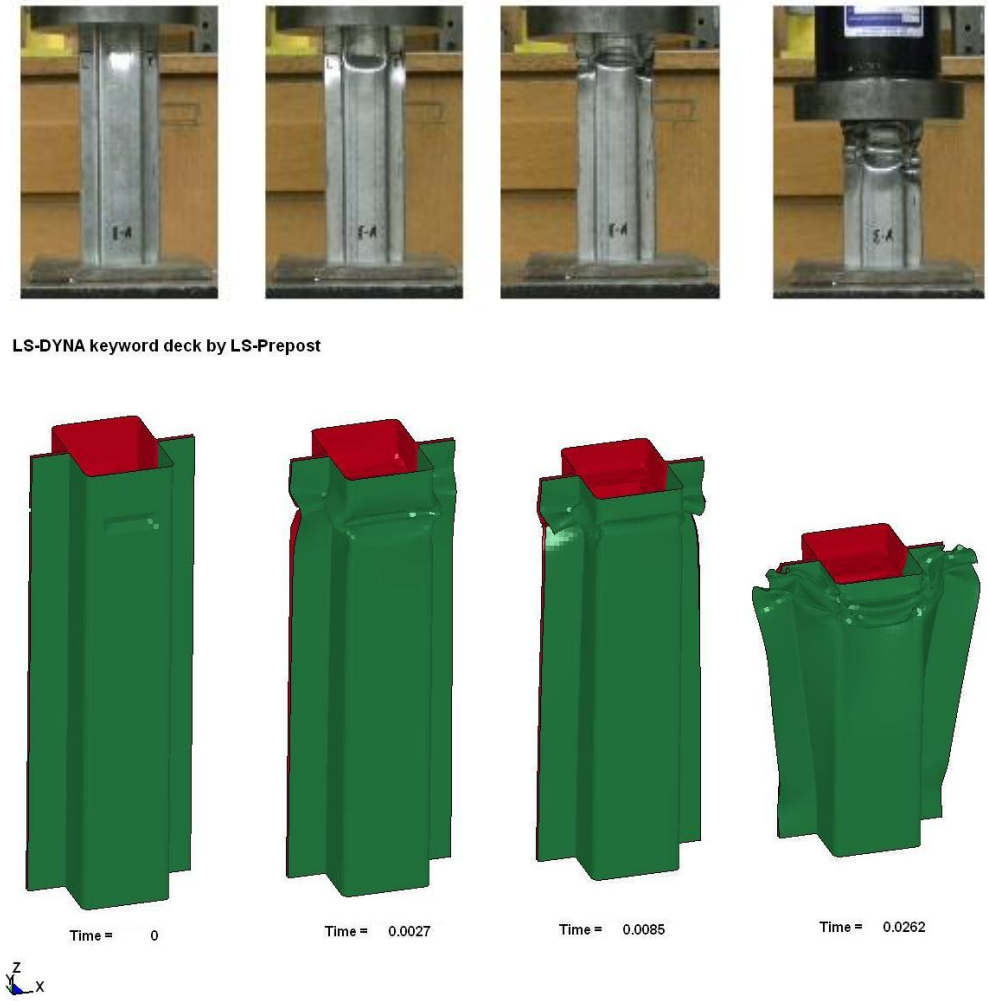

Figure 96: Crushing progression, Quasi-static experiment vs. simulation

Figure 97 through Figure 100 show the axial deformation behavior of hat and channel sections tested under quasi-static conditions. For both geometries, the collapse modes and load-displacement histories developed by the numerical model were in good agreement with the quasi-static test results.

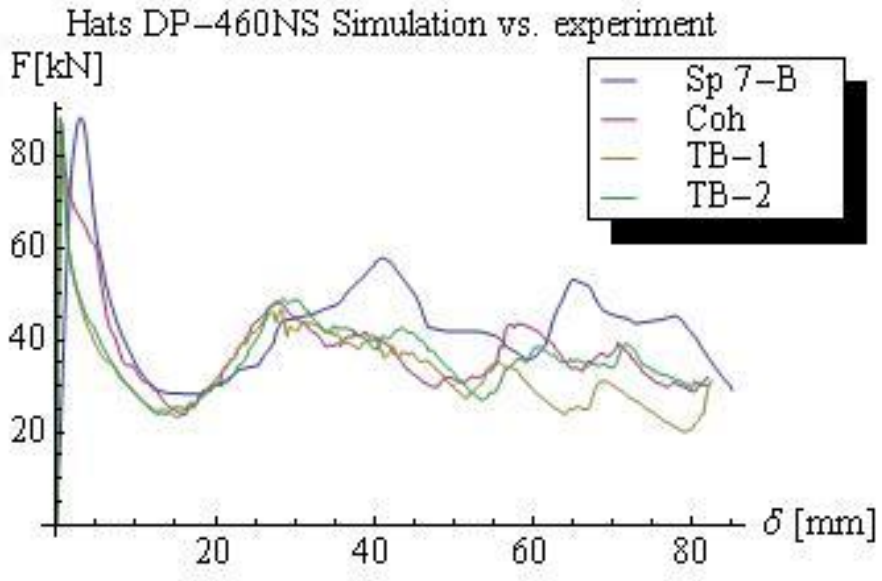

Figure 97: Quasi-static simulation results for hat sections with DP-460NS adhesive joints

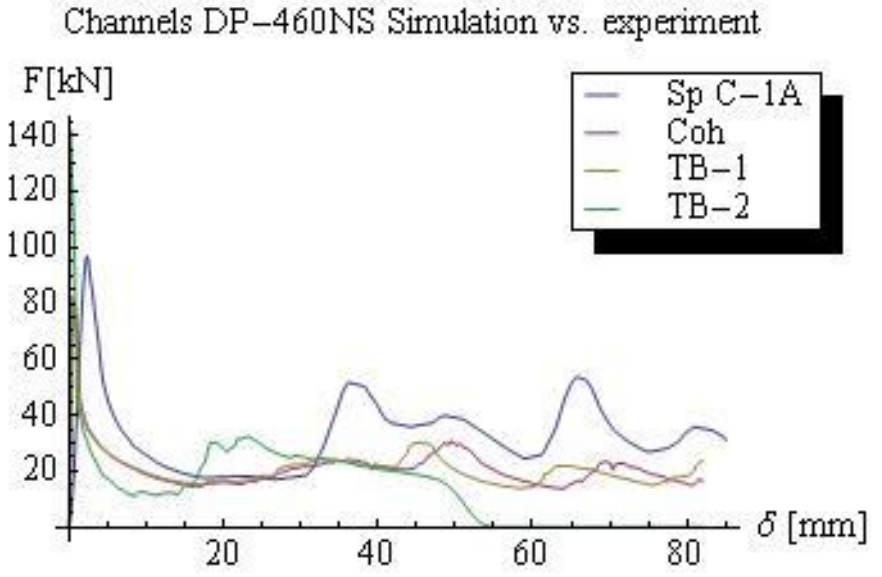

Figure 98: Quasi-static simulation results for channel sections with DP-460NS adhesive joints

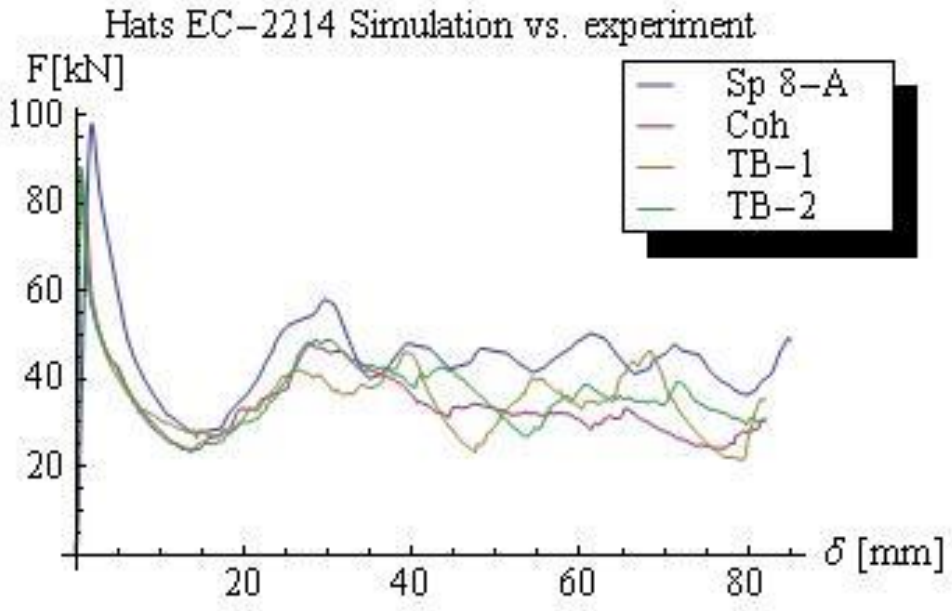

Figure 99: Quasi-static simulation results for hat sections with EC-2214 adhesive joints

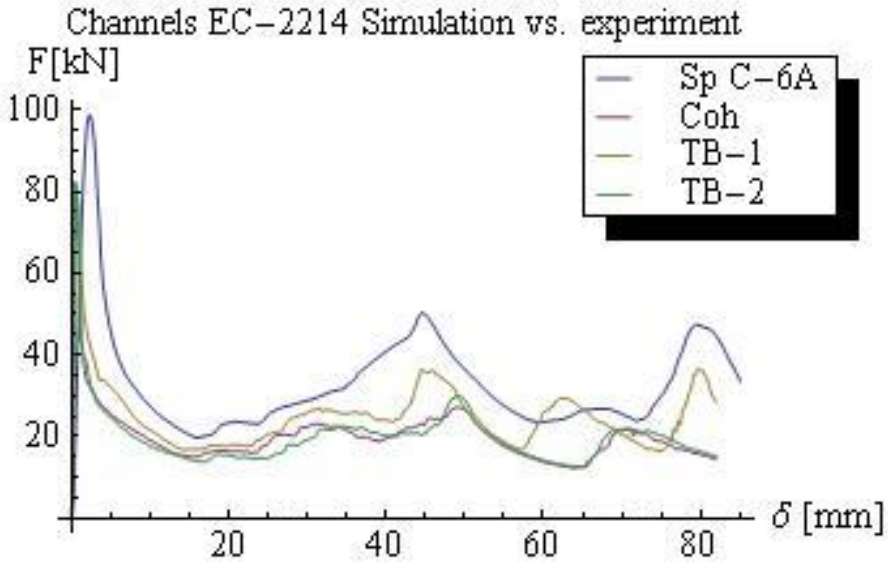

Figure 100: Quasi-static simulation results for channel sections with EC-2214 adhesive joints

Although the results correlate very well, it is important to notice that the predictions in the channel section models seem to be characteristically lower than the experiment (Figure 98 and Figure 100), especially at the peaks that represent the formation of a fold. In the simulations was assumed that the

steel material for both channels and hats was identical but the t-test (Table 4) demonstrated that they were not because the micro-hardness of the channel was higher than that of the hat. Since the simulation used a softer material to describe the steel it is clear where this difference comes from. Quasi-static and dynamic experiment testing results are presented in tables 12 and 13 to compare absorbed energy, specific energy, mean force, and peak force across the mean value of the samples and simulation results for the different models use to represent the adhesive layer.

Measurement	DP-460NS				EC-2214			
	Exp	Coh	TB1	TB2	3.44	2.81	2.89	2.99
Energy absorb [kJ]	3.23	3.11	2.75	2.99	6.88	5.62	5.78	5.98
Specific energy abs [kJ/kg]	6.47	6.23	5.52	5.99	40.51	34.27	35.36	36.53
Mean force [kN]	41.65	37.94	33.38	36.52	92.01	87.98	85.27	88.31
Peak force [kN]	88.63	87.81	85.27	88.31	3.44	2.81	2.89	2.99

Table 11: Simulation vs. experiment summary Quasi-static Hats

Measurement	DP-460NS				EC-2214			
	Exp	Coh	TB1	TB2	Exp	Coh	TB1	TB2
Energy absorb [kJ]	2.83	1.73	1.71	1.17	2.78	1.64	2.05	1.63
Specific energy abs [kJ/kg]	8.23	5.03	4.97	3.4	7.98	4.71	5.88	4.68
Mean force [kN]	33.35	21.13	20.91	14.36	32.76	19.99	25.03	19.86
Peak force [kN]	98.59	82.06	82.30	141.8	97.18	81.73	82.30	82.38

Table 12: Simulation vs. experiment summary Quasi-static Channels

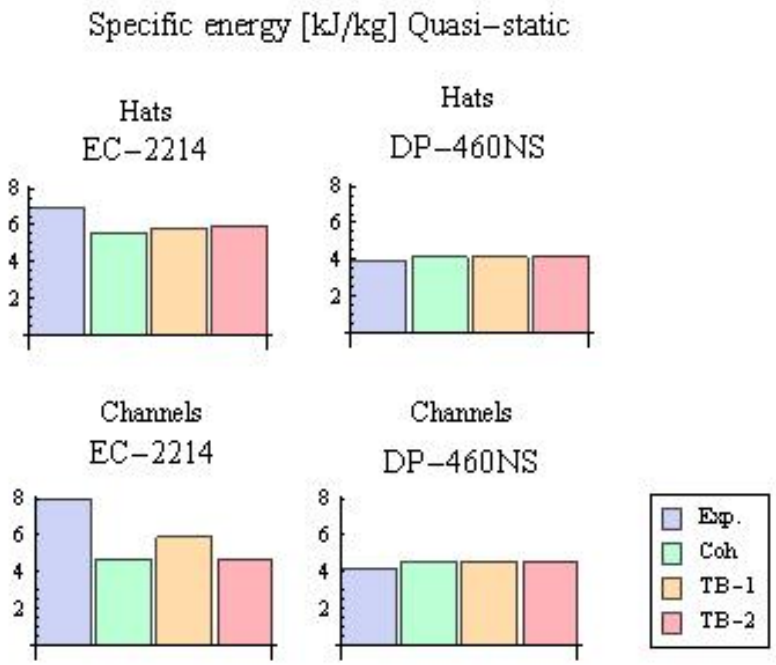

Figure 101: Specific energy absorption, experiments vs. simulations

A good metric of the performance of the tubes is the specific energy, bar charts (Figure 101) of these values were used to compare between simulations and experiments. It is clear from the previous tables, the load-displacement diagrams and the bar charts that the simulations were in good agreement with the experiments. There was some unexpected variation in the results for the simulations using EC-2214 that was not present in the ones that used DP-460NS as the adhesive.

5.3 Dynamic impact simulation results and validation

Models were developed to represent the IFWI machine during numerical analysis of dynamic impact events by mimicking the boundary conditions and impact conditions of the event. Again, a rigid plane was used to represent the impactor, with the provision that the plane's mass and velocity match the impact cart in the IFWI machine at the striking moment. However, the material model was modified to include strain rates effects by adding the necessary true stress- strain data at different strain rates as described in section 4.2.

Energy losses during the actual event, such as friction between the rails and the impactor cart, energy lost to the sound of the impact, deformation and rebound in the impactor and/or the small amount of heat generated in the crush tube during the deformation process, were considered as neglectable and were not replicated by the simulation.

5.3.1 Double hat section results

Figure 101and Figure 102 show the axial deformation behavior of adhesively bonded hat sections tested under dynamic loads. The load-displacement histories predicted by the numerical model are in good agreement with the dynamic impact test. However, the model predicts a higher plateau force after the first yield and lower final deformation (stroke of the striker). In the case of the experimental hats, the geometry of the cross section was highly sensitive to deformation during the indentation process. This introduced changes in the material and geometry that were not fully captured in the model; hence the model prediction was slightly different than the one by the experiments.

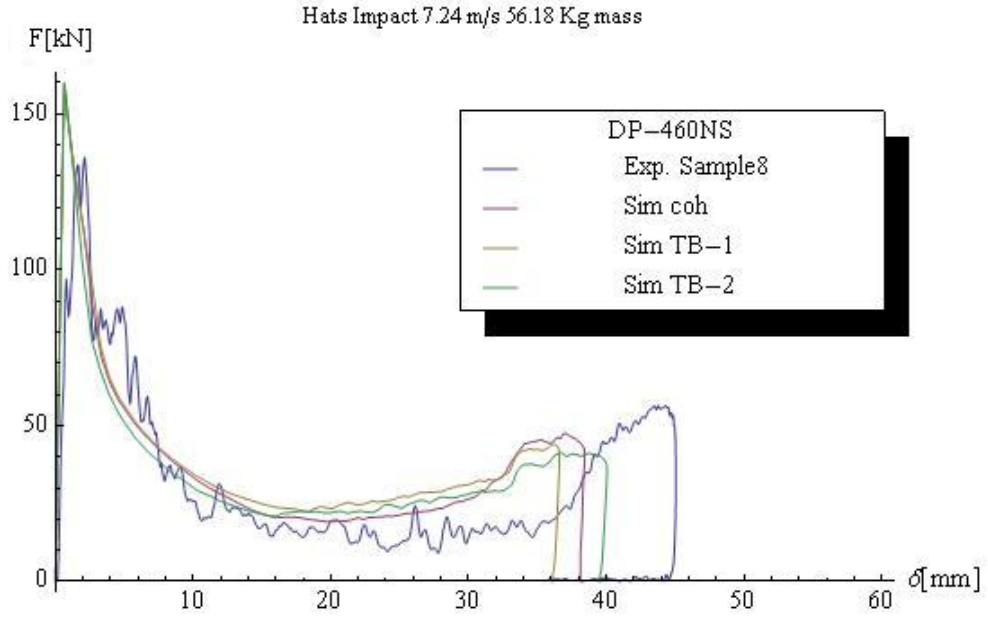

Figure 102: Hat sections bonded using DP-460NS, dynamic load

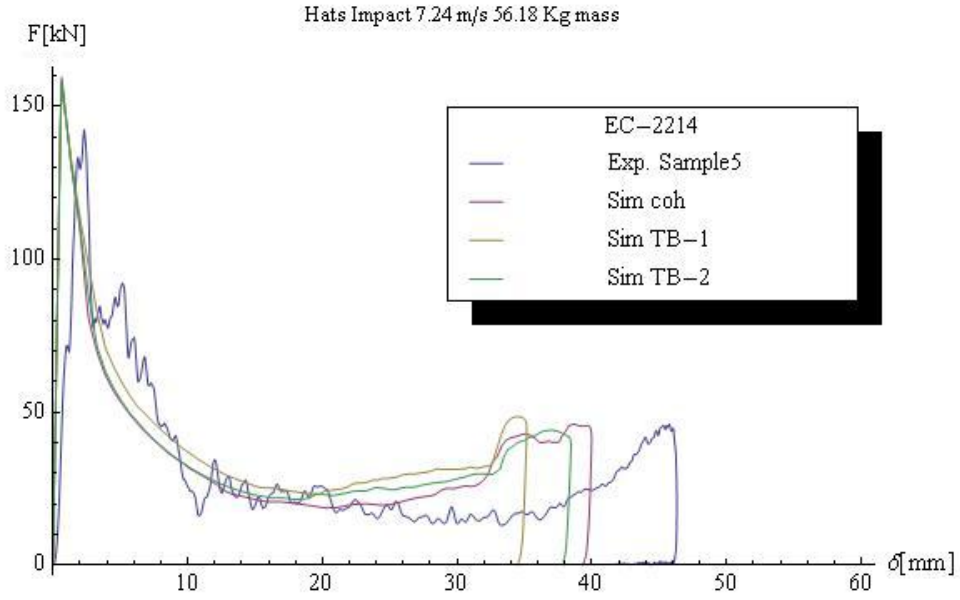

Figure 103: Hat sections bonded using EC-2214, dynamic load

5.3.2 Double channel section results

Figure 104 and Figure 105 show the load-displacement history of adhesively bonded channel sections tested under dynamic loads. The response predicted by the numerical models are in good agreement with the dynamic impact test although there is a significant lower plateau force value after first yield predicted by the models with a higher level of deformation by the end of the stroke. In this case, both of these values depended on the used properties for the steel material. By having a weaker material on place in the simulation, the required load to deform the tube is lower hence less energy is dissipated and a larger stroke of the impactor can be expected.

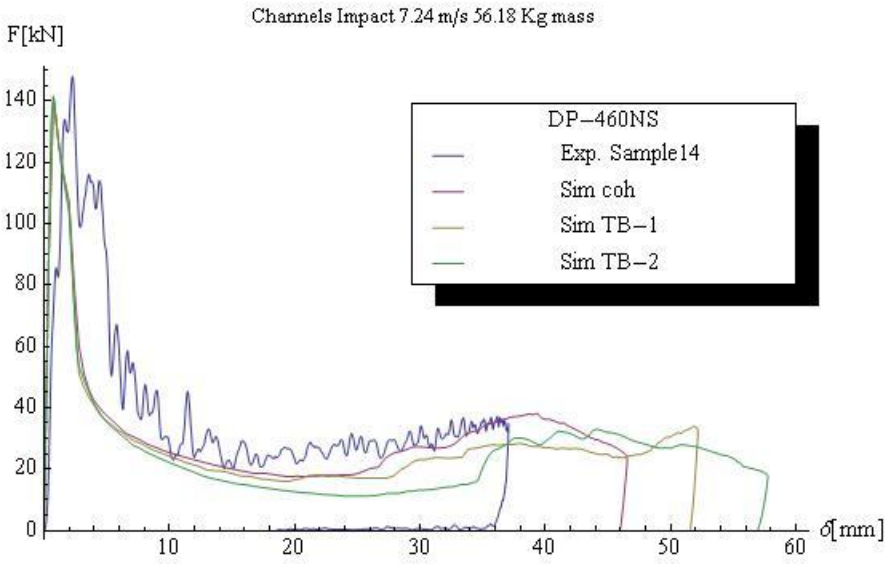

Figure 104: Channel sections bonded using DP-460NS, dynamic load

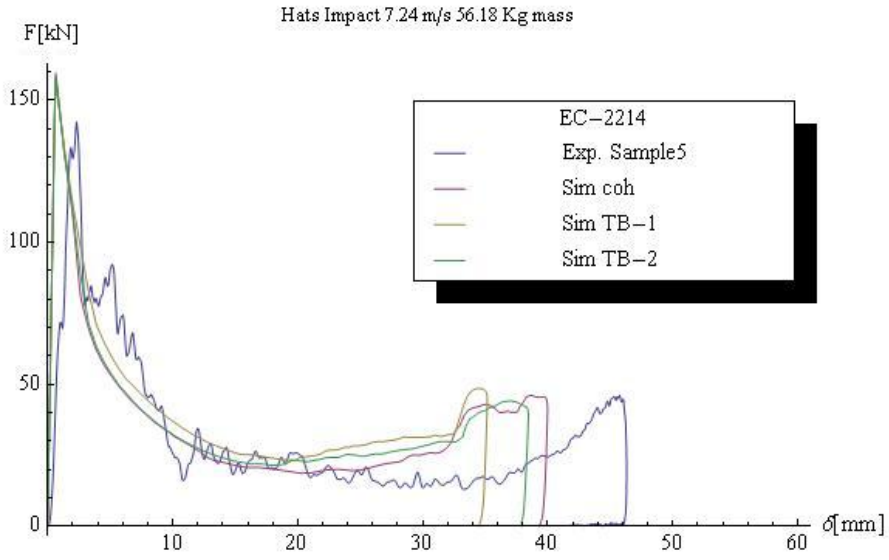

Figure 105: Channel sections bonded using EC-2214, dynamic load

5.3.3 Analysis

Although, the force-displacement curves are in good agreement, they are not a good metric to evaluate failure mode in the member. To elaborate: even though the tube can be absorbing energy as shown in the force-displacement diagram, a mode of failure that is not favorable to the structure, e.g. mode I opening in the adhesive joint, could have started and this is not being reflected by the force-displacement diagram. Also the experiments did not have enough energy to cause more deformation; hence the predictions in terms of performance are very limited.

Dynamic experiment testing results are presented in Table 13 and Table 14 to compare absorbed energy, specific energy, mean force, and peak force across the mean value of the samples and simulation results for the different models use to represent the adhesive layer.

The specific energy values were used again to compare between simulations and experiments (Figure 106). In the case of dynamic events, there were no distinguishable differences for the different geometries when one uses cohesive elements, or the two proposed Tie-Break formulations.

Measurement	**DP-460NS**				**EC-2214**			
	Exp	Coh	TB1	TB2	Exp	Coh	TB1	TB2
Energy absorb [kJ]	1.48	1.45	1.46	1.46	1.48	1.46	1.46	1.46
Specific energy abs [kJ/kg]	3.37	3.30	3.32	3.32	3.36	3.32	3.32	3.32
Mean force [kN]	33.10	37.96	39.92	36.54	32.93	36.63	41.51	38
Peak force [kN]	136.22	159.75	156.59	160.06	137.84	159.53	156.34	157.87

Table 13: Simulation vs. experiment summary Dynamic impact for hat sections

Measurement	DP-460NS				EC-2214			
	Exp	Coh	TB1	TB2	Exp	Coh	TB1	TB2
Energy absorb [kJ]	1.46	1.46	1.46	1.48	1.47	1.46	1.46	1.48
Specific energy abs [kJ/kg]	3.61	3.61	3.61	3.65	3.66	3.66	3.66	3.71
Mean force [kN]	36.94	31.37	27.98	25.67	34.90	28.65	32.18	24.77
Peak force [kN]	146.05	141.27	141.27	141.54	144.55	137.98	141.28	141.82

Table 14: Simulation vs. experiment summary Dynamic impact for channel sections

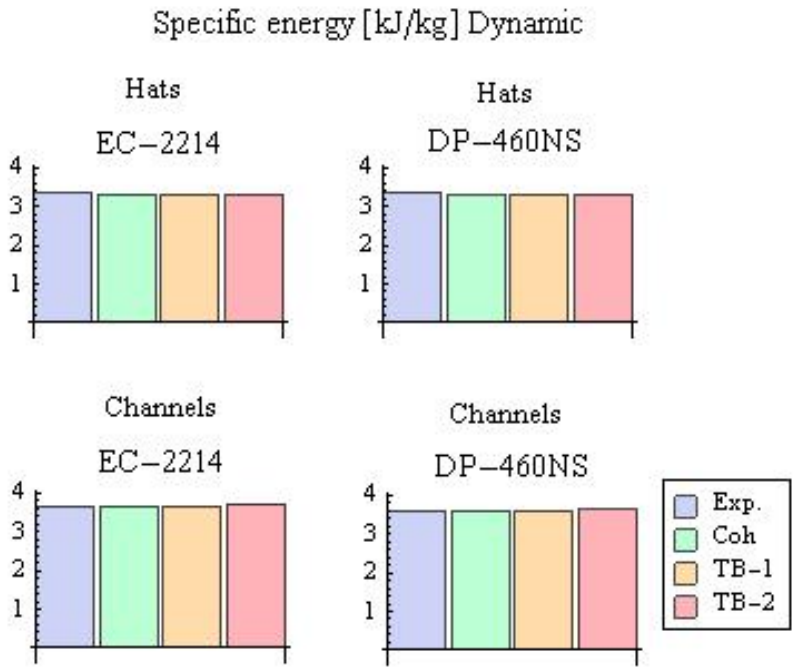

Figure 106: Specific energy absorption, simulations vs. experiment

5.4 Stress in the joints

One advantage of using numerical simulations is the ability to obtain more information that can be generally obtained out of a given experiment. By example, with the LS-DYNA post-processors it is possible to track the stress in a specific location by selecting one element, this will be almost impossible to do in a real setup using strain gages. In general, this information can be used to better understand the physical behavior of joints or structural elements. In the case of the crush tubes bonded by adhesives, the software package permits us to look at stress distributions or stresses at a given point. To obtain this type of information one must fall back to the use of solid elements. Tie-breaks and cohesive elements were design to keep track of the force in a particular direction and when the failure point is reach it would fail the element; these elements implementation was not gear towards keeping track of stresses.

5.4.1 Joints in hat sections

The joints, in the case of the hats, were presumed to be mostly loaded in mode I. In this failure mode, the load tries to open the joint by pulling away each face of the steel lip. Indeed this is how the joint fails and it may imply that the adhesive failure is due only to pure normal stresses. This was disproof by observing the contour plots for shear stresses (Figure 107) for the duration of the event in the totality of the adhesive joint. If one were to think of the joint as it is a beam that is bending to represent the fold, one must conclude that the presence of shear is unavoidable; the question then is how significant these shear stresses are. It is clear that the adhesive layer was loaded with a high shear stress, mostly in YZ direction (Figure 108), besides the expected normal stress in the Y direction (mode I), and this combine state of stress must contribute to the failure of the adhesive.

The stress values depicted in Figure 108 can be explained as:

1. Z stress: Stress develop due to the axial compression of the member
2. Y-stress: Stress develop due to folding process plus the natural tendency of the joint for failure mode I
3. Any others: Stresses develop due to the interaction between deformation of parts and mismatch in material properties between adherents and adhesive

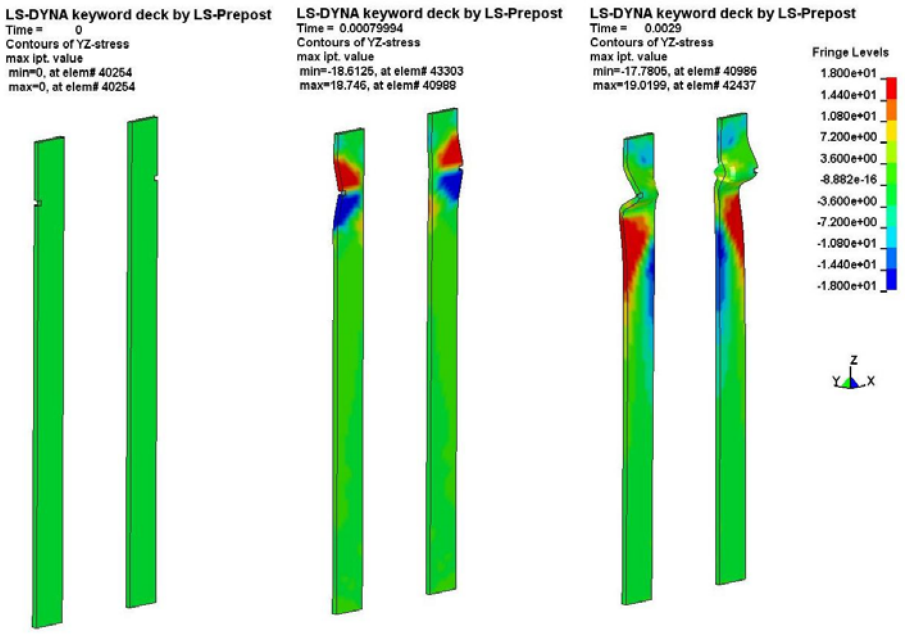

Figure 107: YZ-Adhesive joint stress distributions in crush tubes built using hat sections

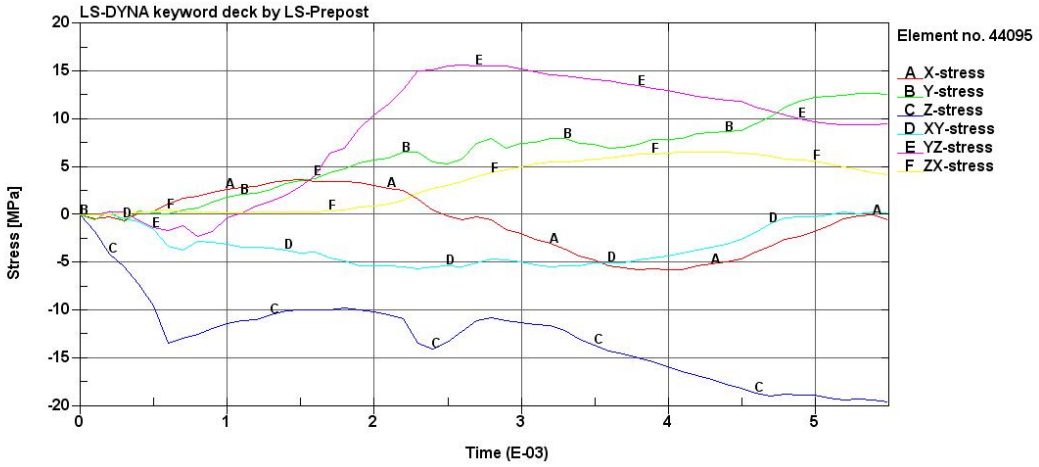

Figure 108: Stresses for element in the adhesive joint of crush tubes built using hat sections

From the theoretical point of view, it is interesting to verify the prediction of the theoretical equation for normal stresses (Equation 19). This is a quite forward expression that relates the normal stress in the adherent with the one in the adhesive. This expression was calculated using steel as adherents and DP-460NS as the bonding agent. Equation 19 can be simplified to:

$$\sigma^* = 0.41 \left[1 - \left(\frac{2.18 \times 0.3}{207 \times 0.41}\right)\right]\sigma$$
$$\sigma^* = 0.4068\,\sigma$$

For illustration elements inside the joint were selected and their stress history plotted (Figure 109). As it can be seen in the figure, the external elements that represent the steel were loaded along the principal Y axis but the developed normal stress in the joint do not match the one predicted by multiplying these values by a factor of 0.41 as predicted by the equation for normal stress in joints. From the point of view of design it could be used to obtain a quick number on the order of magnitude of normal stress in the joint, but this could be a misleading number due to the high value of the shear component.

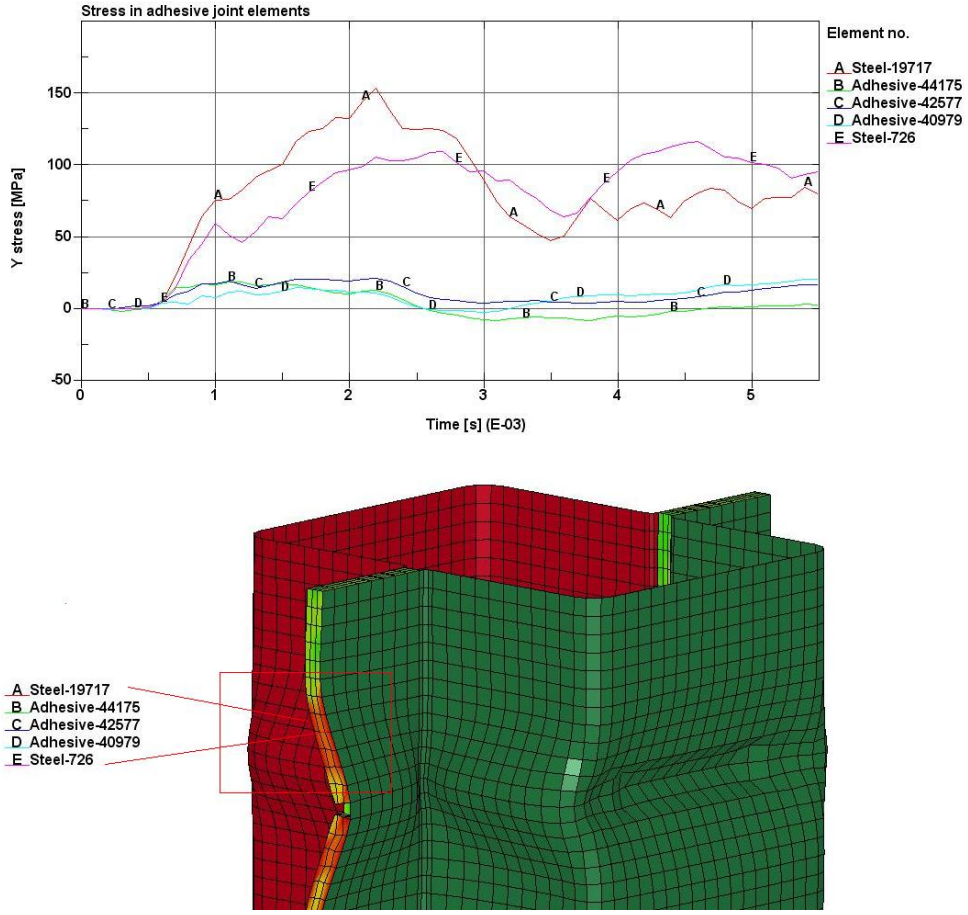

Figure 109: Stress in Y-axis, element in the adhesive joint vs. adjacent elements

5.4.2 Joints in channels

In the case of the crush tubes build by using channels sections, the joint should be loaded in mode II, where the adhesive layer develops high shear loads. For this type of structure this assumption holds true for most of the joint. There are small regions of high normal stresses associated with the folds (Figure 110) and high stress concentration at the corners of the folds (Figure 111), but the rest of the joint gets mostly loaded in shear (Figure 112).

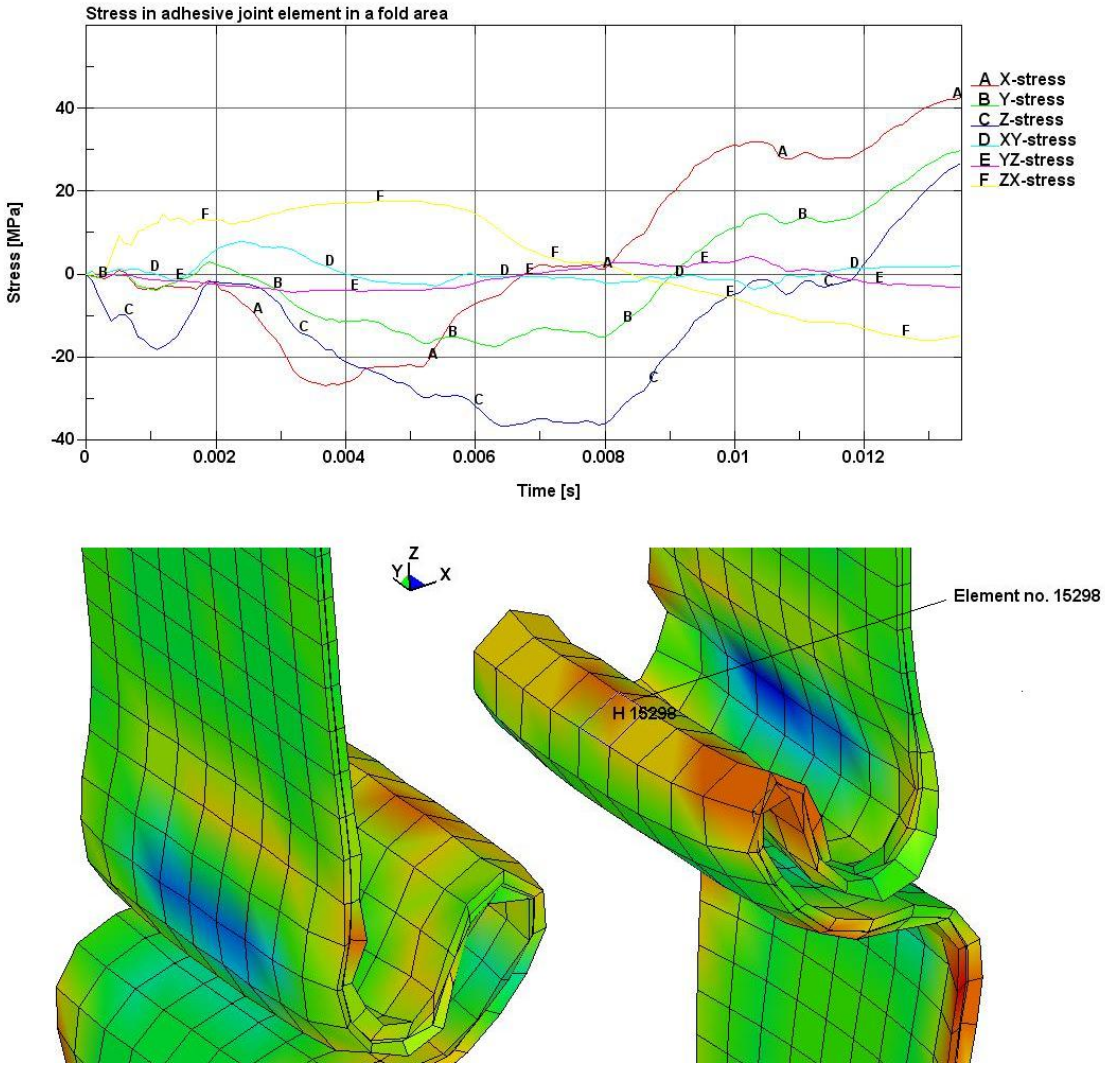

Figure 110: Element stresses in an adhesive joint for a crush tube built using channel sections

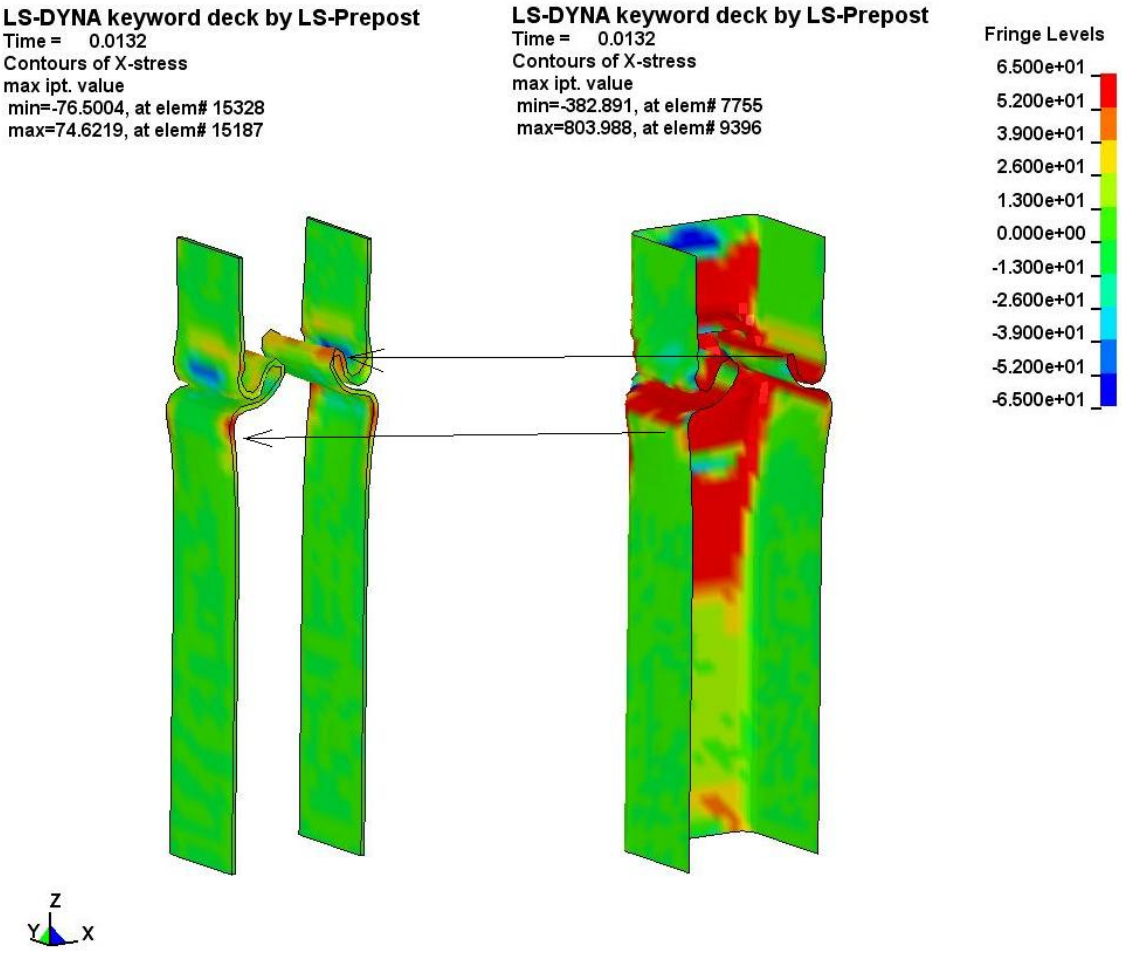

Figure 111: Regions of high normal stress in joints of tubes built using channel sections

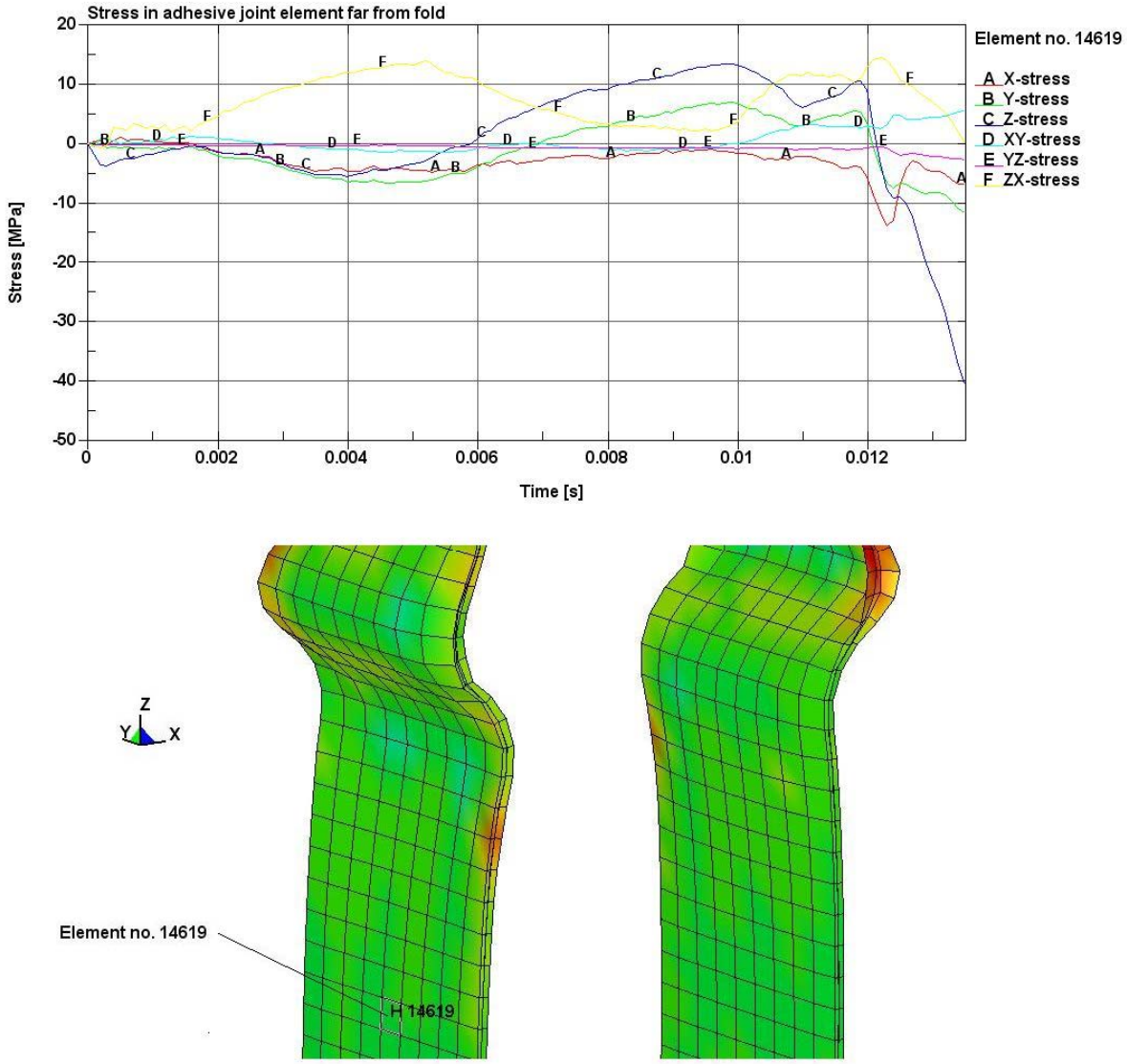

Figure 112: Element stresses in an adhesive joint for a crush tube built using channel sections

In this case the theoretical prediction for a stress distribution in a joint loaded in shear (Equation 18) is not applicable due to the nature of the loading direction. Notice that the direction of the highest shear stress (mark as F in Figure 112) does not coincide with the direction of loading proposed in the equation. Also, the ZX direction of the highest shear stress coincides with the expected shear direction in a beam subjected to bending.

Chapter 6
Discussion

6.1 Crush tube experiments

A series of test were conducted under quasi-static and dynamic loading, however, the extent to which these experiments truly replicated crash-equivalent loading was limited by the available equipment. Although evaluation of structural performance under dynamic conditions is critically important for the intended application, the energy generated during the dynamic experiments was not high enough to produce an event comparable to an automotive crash but was able to achieve one complete fold in the crush tubes. Generalizations and conclusions from this analysis have to be considered in this light and extrapolation of results is not encouraged.

The use of sub-size samples has been explored and validated. This was of significant importance for the experimental work, since it allowed reducing the size of the samples and equipments. Historically the use of scaled models during dynamic events has proved to be problematic with distortion effects due to the non-scalability of strain rate effects in the tested materials [21]; however, with the procedure described here the previous inaccuracy problems can be addressed in the case of testing single material structures. The introduction of a second material poses some new challenges and the accuracy of the scaling method is definitely impacted. Given the growing interest in the development of multi-material structures to optimize weight reduction and crash performance, it will be critically important to address issues that currently prevent accurate scaling of multi-material testing in the near term.

Under quasi-static testing; energy was absorbed through progressive collapse (folding) of the structure and only in very few cases did catastrophic debonding of the joint occur. In such cases, failure was caused by imperfections in the structure such as deformations in the cross section, which introduced additional stresses that likely would not be present in a production component.

Under dynamic loads, there was only enough energy present to initiate the first fold. This was consistent for all structures. In addition to the fold initiation indent, a notch was added to the tested hats. In all cases, this geometry demonstrated, premature debonding at the top and crack propagation in the joint. It was determined that the deformations induced in the hats during the notching process had a significant impact in how the structure responded during dynamic events.

Due to the manufacturing process, it is possible that excess adhesive in the joints could create stress concentration areas. Also, it was not possible to practically tell if there were any defects inside the joint that bonded the two sections together. While ultrasound could have been a feasible solution to this problem, the presence of multiple materials would likely impact the accuracy of results.
There was an unexpected difference in material mechanical properties between the hats and the channels, but one has to consider that the mechanical properties of both sections may be in the range of a normal distribution for a single material. More than the micro hardness test as done in this work, heat analysis and fractography may be required to thoroughly differentiate the steel material for each section. One has to keep this fact in mind for any comparisons between crush tubes; and this difference may preclude direct comparisons between geometries.

6.2 Numerical models

Numerical methods used to define adhesive materials have been investigated by comparing results from computer models against experimental results of the same event. The limitations for the numerical representation methods are discussed below.

6.2.1 Cohesive elements

The use of a single layer of cohesive elements to represent the adhesive joint of built up sections had permitted to accurately describe the crushing behavior of these sections under quasi-static and dynamic scenarios..

But the numerical implementation used in the present work for cohesive elements failed to capture the following behaviors:

1. Strain rate effects. While irrelevant for quasi-static testing, these effects can be significant under dynamic loads.
2. Stress induced by bending. Since there is only a single solid element, stress induced by bending effects will not be captured accurately, although the adhesive layer was located in the neutral axis, precluding this effect; in other cases this may be an issue.
3. Pre-stress in the joint.
4. Stress concentrations due to imperfections, such as voids or cracks and spills in the joint. It was assumed that the bond was a perfect continuum.

Mode II failure data was approximated for this study and is a limitation of the cohesive element implementation.

6.2.2 Adhesive Tie-break model

Although the following discussions brings to attention important facts about the implementation of Tie-break elements, during practical use the proposed implementations prove to be quite robust, and the results were remarkably close to the ones obtained by using cohesive elements.

6.2.2.1 Implementation 1, spring with failure (TB1)

The accurate selection of the failure parameter is critical; because this will change the amount of energy the joint dissipates during failure. Because there is no definition of a force-displacement curve and the modulus of elasticity of the spring depends on the materials being joined and the discretization, the calculated forces and the stresses in adjacent elements to the joint can be artificial.

6.2.2.2 Implementation 2, discrete crack model (TB2)

The failure behavior of this type of element is defined by two options that aim to mathematically describe the failure behavior of the adhesive material. The equations presented in the LS-DYNA manual [29] to determine the displacement at failure seem quite general and capable of representing a wide variety of materials; although both of them use the energy release rate to determine when the failure occurs; the selected model need to be tailored to the particular adhesive materials used. For this work the simple power law with and exponent equal to one was used and generated good results for the crush tubes, but this may explain why this type of Tie-Break did not do as well in the DCB simulation.

6.2.3 Crush tubes

6.2.3.1 Quasi-static model

A notch had to be introduced in the models to avoid numerical instability and force the solution to converge; this notch was not present during experimental testing, which may have introduced discrepancies in peak load values between simulation and experiment. At very low load rates the simulation times do not need to be excessively long, since mass and time scaling can be used to reduce the simulation time. This was implemented without introducing significant error since numerical simulation and experimental results were in good agreement.

6.2.3.2 Dynamic model

The use of a rigid wall to simulate the impact car of the IFWI machine may have introduced artificially high peak loads due to lack of compliance in the numerical model. The stress state in the structure may not accurately represent the true values since interaction between the impact car and the crush tube structure has to be affected by the lack of energy dissipation in the model and the boundary conditions. Both conditions are generated by the use of a rigid wall. Since the force trace of the model was in good agreement with the experiments the error introduce by the use of a rigid wall instead of a compliant one in minimal and the use of a rigid wall was maintain for numerical efficiency.

The results of the model were highly dependent on the accurate representation of the geometry in the case of the hat geometry. During the indentation process of the buckle initiator, changes in the cross section of the tube were introduced through permanent deformation. The first numerical models did not consider these features but once this was introduced there was a better agreement between models and experimental results. This same feature introduced changes in the mechanical properties of the material due to straining and cold work; such effects were disregarded in the models. Another consideration is the definition of the constitutive model for the steel material: the strain rates measured in the model in the folding areas were around 400 1/s. Although the model included information for strain rates of 1000 1/s, this information was extrapolated from the testing data. The software will interpolate between n the 100 1/s data and the 1000 1/s extrapolated information to obtain information for the material properties at the required 400 1/s. This will also contribute to the differences between numerical model and experiments.

Chapter 7
Summary and recommendations

Two structural epoxy materials (3M, Canada), were investigated as bonding agents for built up energy absorption structures, and were represented in a numerical code using cohesive elements and Tie-Breaks. Responses predicted by numerical models using both types of elements were compared against experiments under quasi-static and dynamic conditions using representative sub-size crush tubes. Two geometries were explored: sections made out of hats, which is a cross section typically used due to ease of manufacturing when spot welding is desired, and sections made out of channels, which may be a dedicated solution for the use of adhesives.

7.1 Sub-size structures

Historically, scaled down models have been important tools for advancing engineering knowledge in a broad range of fields, from aerodynamics to city planning. In cases where structures are subjected to impact events under dynamic loading conditions, scaling has proved to be problematic due to strain rate effects. A solution proposed by Oshiro and Alves [34] was explored using crush tubes. For a structure made out of a single material the scaling method yielded accurate results; however, the introduction of a second material, namely the adhesive joint, caused divergence between model and prototype in terms of predicted deformation and failure path of the adhesive joint. Notwithstanding the differences in deformed shapes, the prediction of the stress levels was in good agreement between both structures. The calculation between model and prototype in terms of absorbed energy and mean force using non-dimensional numbers was affected too, rendering the use of Pi numbers as non useful.. Certainly an additional correction is required due to the effect of the second material. A reasonable approach could be to consider the effect of the different materials by modifying Equation 22 to include the effects of each material as a product between them as shown in Equation 29.

$$\beta_{V0} = \sqrt{\frac{f(\beta_{Vo}\dot{\varepsilon}_m^{nc})}{f(\beta\dot{\varepsilon}_m^{nc})}} \rightarrow \beta_{V0} = \sqrt{\prod_{i=1}^{n} \frac{f_{mi}(\beta_{Vo}\dot{\varepsilon}_{mi}^{nc})}{f_{mi}(\beta\dot{\varepsilon}_{mi}^{nc})}}$$

Equation 29: Propose modification for multi-material scaling

This is an empirical approach and has not been subjected to the required rigorous mathematical analysis as was done by the original authors.

7.2 Experimental testing

Experimental testing is reasonable way to obtain certainty in design performance or for verification of models; however, in some instances it may not be economical and in certain cases completely impractical. This study conducted a series of tests under quasi-static and dynamic loading to verify the response of numerical models against theoretical predictions, compare performance between a traditional welded structure and one constructed using adhesives, and gain understanding of the failure modes of adhesively bonded structures.

In general, there was good agreement between predicted theoretical mean loads and the recorded loads for structures tested under quasi-static conditions. However, under dynamic loading the theory predictions were off from the measured results in the case of the hats. For this particular section the theory over predicted the mean load during a dynamic event (53.67 kN vs. 23 to 33 kN); but one has to consider that this calculation is highly sensitive to the model one selects to modify the static mean load to turn it into a dynamic value. In this particular case the Cowper-Symonds expression generated from curve fit#1 was used. In this curve fit the data used was bias towards the higher yield hence the higher calculated load. In the case of the channels both quasi-static and dynamic conditions were in good agreement.

Traditional thinking can be misleading; because of higher energy absorption and higher mean force developed by the hat sections during both the quasi-static and dynamic events one would expect better performance in general, but based on the specific energy the channel sections outperformed the sections built with hats in both cases. Certainly this could be solely due to the better mechanical properties in the steel and lower weight of the channel sections; but one must recognize that the performance of crush tubes structures can be highly dependent on the failure of the joint. As was seen in the experiments, as long as the joint did not fail, or at least not catastrophically, the integrity of the cross section was maintained and the energy absorption process carried on through fold formation. If the joint failed, instabilities were prone to appear causing changes in the folding pattern and even leading on one occasion to Euler buckling causing a drastic decrease in energy absorption. Due to the nature of the different geometries, the hat sections were more susceptible to failure in the joint than the channel sections. To elaborate in the last sentence:

1. A failure of the joint in the hat sections made the structure prone to opening with a possible separation of the flanges therefore reducing the effective inertia of the cross section and reducing the chance of fold formation which is the mean mechanism of energy absorption.
2. Although a failure of the joint in the channel sections was possible due to the high state of stress in the adhesive material, the channel webs locked into each other once the folding pattern initiated maintaining the integrity of the cross section.

The state of stress in crush tube joints was briefly analyzed and was correlated with the geometry used for the construction. Crush tubes constructed from hats were suspected of failure in pure mode I. After looking at the stresses in the joint it was clear that although the crack propagation of the joint corresponded indeed with mode I, the adhesive material was subjected to a stress of state that involved high shear forces and not pure normal stresses as one would expect for a mode I failure. When the crush tubes were build out of channels, mode II failure was expected, since it is believed that the adhesive joint would be predominantly loaded in shear. Indeed the load was mostly shear, but in corner regions like the endings of the joint, there could be a high normal stress induced by the sections trying to open up, and these zones could trigger the failure point.
Under both load cases (quasi-static and dynamic), the bonded structures performed similar to the welded ones, proving that the alternate use of adhesives was possible, although bonded structures seem to have a high degree of variability in the results. This must be due to the nature of the adhesive material itself. It is possible that micro-voids in the adhesive joint incited damage at different locations causing slight changes in the structure response; although the differences in the load-displacement diagrams in many cases seem minimal. The variability can be more clearly seen in the Box-whisker plots presented in Chapter 5.

7.3 Numerical representation of adhesives

This study also investigated the applicability of numerical methods to represent adhesive bonds by using cohesive elements and tie-breaks. Three different methods were proposed to define the parameters of adhesive materials using cohesive elements. Of these, the use of results from simple mechanical testing, such as a tensile coupon or a lap shear test, proved to be the simplest and most efficient method to obtain parameters for an accurate numerical representation of the bond.

7.3.1 DCB test

A Double Cantilever Beam test (DCB) was implemented as a computer model using the LS-DYNA code, and cohesive elements were used to describe the adhesive layer. Three different methods were used to develop the traction-separation curve which defines a cohesive element. The results from each one were compared against experimental data to determine the accuracy of the model's predictions. Of the three methods proposed, the bilinear formulation and the curve fitting from lap-shear experiments produced good results when compared against the experimental results of the same test using EC-2214 epoxy material as the bonding agent. Although there was a significant difference in stiffness between the models as seen in the load-displacement curve (Figure 31), the plateau load was almost indistinguishable between one model and the other.

The results of the DCB test can be used as a verification procedure for the constructed numerical method; conversely, the numerical model of the same test can be used as verification of the experiment. For verification the load responses between experiment and numerical model have to be in agreement. In cases where the actual DCB test cannot be implemented, the numerical representation using cohesive elements constructed from available information out of lap shear or tensile coupons is robust enough to be used to predict fracture toughness with confidence. In this regards, although no experimental data were available for the DP-460NS material, the predicted K_{IC} from the model was in good agreement with the values for the adhesive material when the model was constructed using the curve fitting from the lap shear test.

By comparison with cohesive elements, Tie-breaks were faster for computational analysis but were a compromise in the quality of the results. Tie-breaks have many advantages in terms of computational efficiency but their use must be approached cautiously. Even when using the correct property values for the mechanical characteristics of the material, the results from a model using tie-breaks can be erroneous (Figure 33). In this particular scenario it was identify that the criteria used to define the failure point may had been the problem. Tie-Breaks can be tailored to represent the adhesive in a particular scenario but that does not guarantee that they will represent the material behavior accurately under different circumstances.

Cohesive elements; although more computationally expensive (Figure 34); produced a result that was closer to the actual response, at least in the case of the DCB model. Besides the time penalty in the solution time, more information was required to build the model.

7.3.2 Adhesives in crush tubes

It has been shown that the use of numerical models to accurately represent a structure subjected to impact loads is certainly within the capability of current software codes. Numerical codes provide designers with a high level of flexibility, allowing them to explore many different aspects of an impact event without the need for expensive experimental set ups. For example, one can look at the stress distributions at a particular instant or make cross sections to better understand a particular region of the solid just by inputting a few commands in the software. Achieving this level of detail in the experimental realm can be quite impractical; the amount of instrumentation and the number of experiments required to reach statistical relevance will be both cost- and time-prohibitive.

During this study the results between simulation and experiment were in good agreement, although a few differences were noticed. It is important that the selected material model can accurately capture the behavior of the materials in the structure and that the geometries and loads depicted by the model are as close as possible to the actual experiment. In some cases, high sensitivity to small geometric differences was noted.

The introduction of adhesive materials, although increases the level of complexity for simulation implementation, is not an impossible hurdle. Many different numerical representations for these materials are available, cohesive elements and different Tie-Break options, the ones explored provided accurate prediction for structural performance at the macro level. It should be understood that the load-displacement diagram generated by the model is in good agreement to the one generated by the actual structure under the same circumstances in an actual experiment.
One major advantage with the use of Tie-Breaks is the reduction in computational times to obtain a solution. This is important from the design point of view, where the designer wants to reduce design time cycles. Tie-breaks proved to be capable of representing an adhesive material and provided good result in terms of overall deformation and measured forces in crush tubes with the added advantage of reducing the computational time. Tie-breaks are a simplification and if one were to look at crack propagation or absorbed energy in the bond during the event using this type of elements, results can be misleading (DCB results).

Neither of the numerical implementations used, cohesive elements or tie-breaks, allowed consideration for strain rate effects. While this is a moot point for quasi-static events, strain rate

effects figure prominently under dynamic conditions. That being said, although the model did not account for strain rates in the adhesive material, strain rates generated in the dynamic test were low enough that it made no significant difference between the experiments and the simulations. At higher velocities, however, strain rates could have a more significant impact. As was previously shown (Figure 22), the material properties of both adhesives are strongly affected by strain rate, which suggests that models must include provisions for strain rate effects.

This limitation can potentially be bypassed by building the model base on the mechanical properties that can be expected at the required strain rate. In order to build appropriate traction-separation curves using this method, one requires knowledge of expected strain rate values for particular events and material property data that corresponds to these same strain rates.

Given the growing interest in multi-material structures, it is recommended to explore the effect of joining dissimilar materials.

To obtain better insight into joint stresses, crack propagation and bond failure, a more complex model is required, ideally a series of solid elements with the proper material model. At this level of detail, the material description will require properties that are join dependent, such as the appropriate traction separation curve, besides the intrinsic properties of the material itself such as yield stress and energy release rate.

In global terms, either cohesive elements or tie-breaks can accurately predict crush tube structure responses, and capture the behavior of the adhesive joint, but cannot provide a more detailed description of the failure process inside the material. Behaviors like crazing and shear bands which are typical of epoxy materials during loading need to be characterized and understood before more detailed modeling can be implemented. Unfortunately, models assembled in the manner described in this work do not produce any insights about the damage mechanism that triggers ultimate failure. At this point, further research is required to characterize damage in epoxy materials and to understand how these failure modes would be affected by changes in dynamic load rates and by the interaction of different materials in the joint.

Appendix A

Crush tubes specifications and manufacturing

A.1 Mechanical drawings

Mechanical drawings of commercial roll form sections purchased from Custom Roll Form Inc to build up the crush tubes.

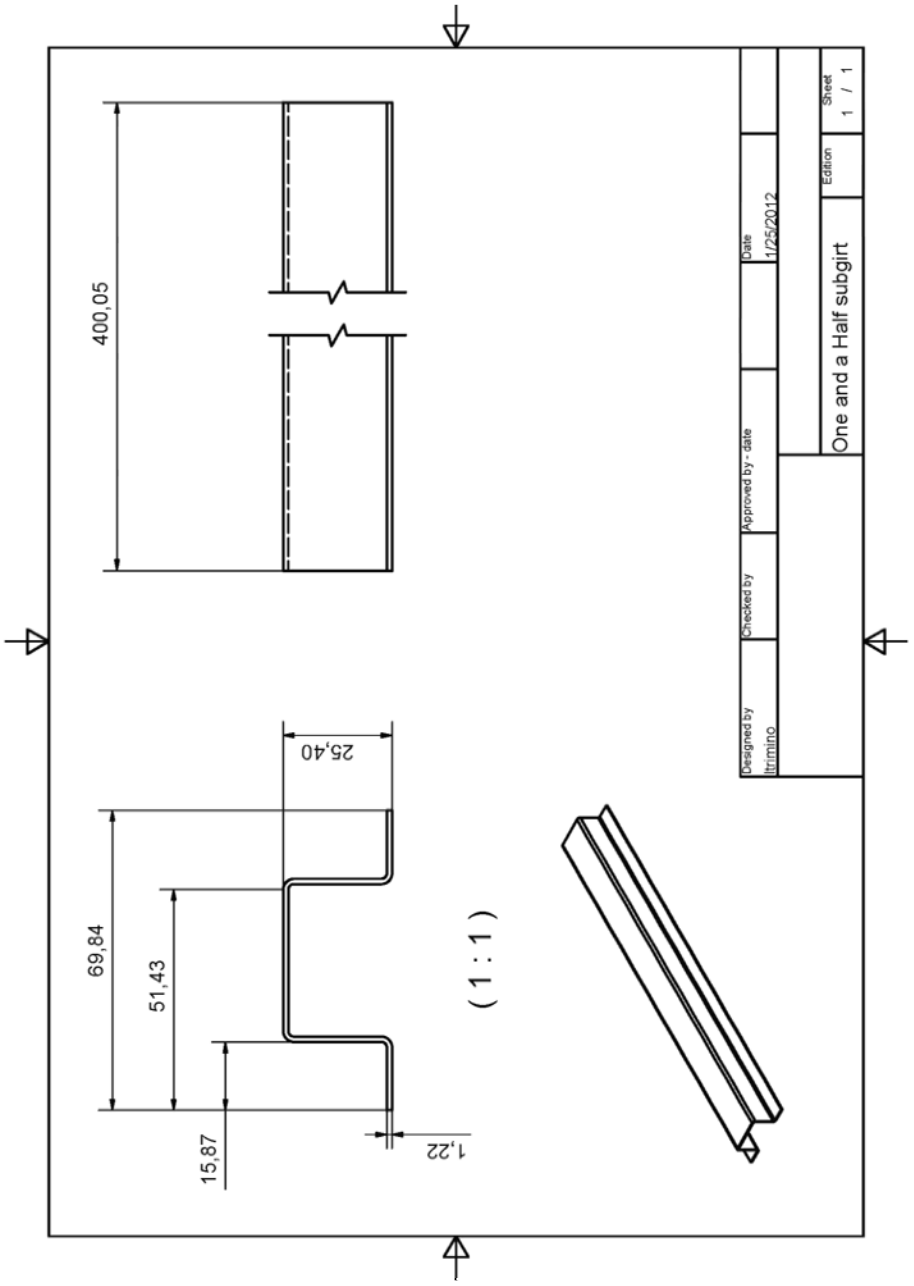

51,80
24,18
1,00
A
A
Prior to bonding:
Prepare mating surfaces by sand blasting
Clean surfaces with MEK
A-A (1 : 1)
Designed by
ltrimino
Checked by
Approved by - date
Date
3/5/2012
Hats-assembly
Edition
Sheet
1 / 1

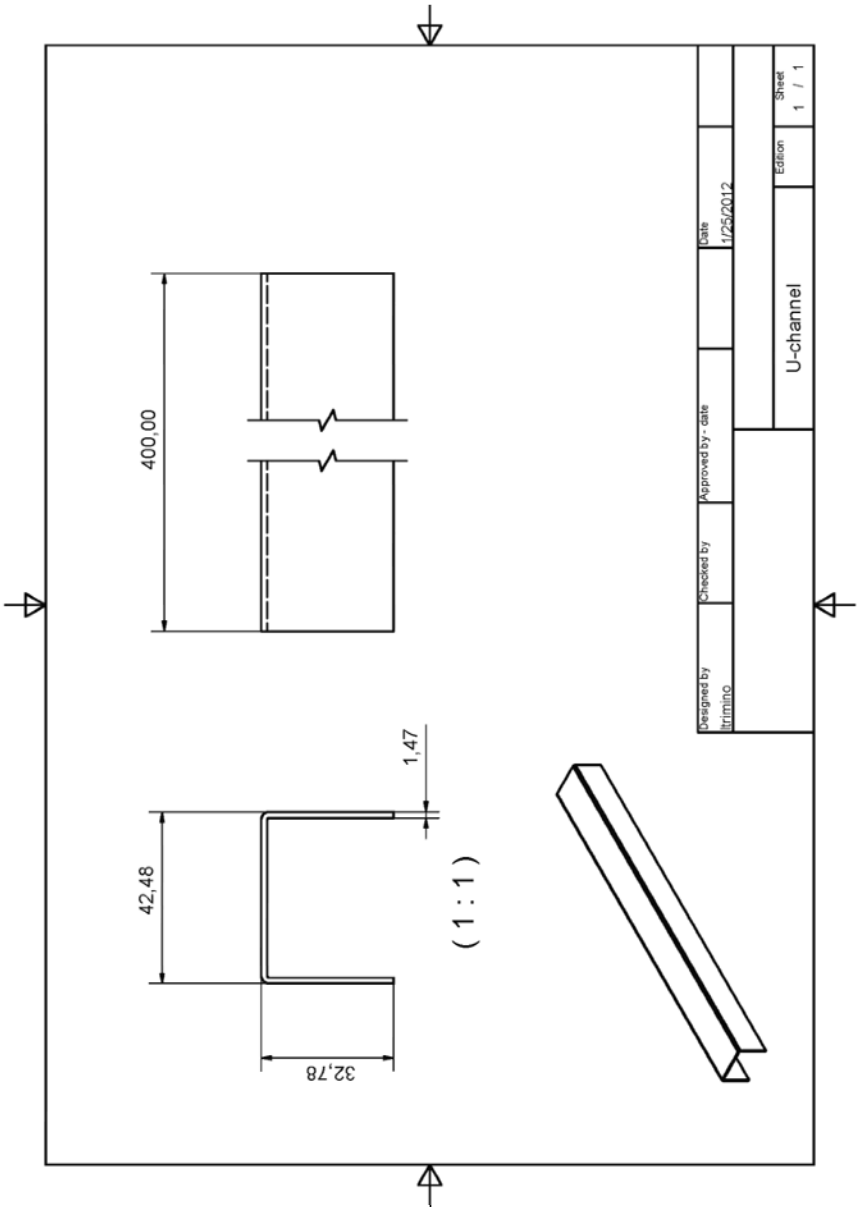
400,00
1,47
42,48
32,78
(1 : 1)
Designed by
ltrimino
Checked by
Approved by - date
Date
1/26/2012
U-channel
Edition
Sheet
1 / 1

Prior to bonding:
Prepare mating surfaces by
sand blasting and cleaning with MEK
A-A (3 : 4)
A
A
44,95
1,00
3,00
35,78
Designed by
ltrimino
Checked by
Approved by - date
Date
3/5/2012
channels-assembly
Edition
Sheet
1 / 1

A.2 Manufacturing process for crush tubes

The roll form sections were used to build close up crush tubes for testing. The procedure involves:

1. Preparation of the raw material surfaces for bonding: typically the surfaces to be bonded are sandblasted to remove the galvanization coat on the lips, and then cleaned with a chemical solvent Methil-Ethil-Ketone (MEK) to remove any dirt and oils detrimental to the bond. Specifically:

    a. Make a few passes with the sand blaster; the entire galvanized coat should be removed from intended bonding surfaces resulting in a dark matte color. Compare between the left and right hand pictures in Figure A1. Only joining surfaces need to be stripped of the galvanized coat.

    b. Chemical degreasing after sandblasting:

        i. Clean the sandblasted joining surfaces with paper towel

        ii. Make one or two passes with scotch-brite impregnated with MEK.

        iii. Clean with paper towel impregnated with MEK. Generally a few passes will do - notice that as you go, less and less residual will appear in the paper towel.

        iv. Dry with clean paper towel, and let it air out. If the paper towel does not come away clean at this stage, a few more passes as in iii may be required.

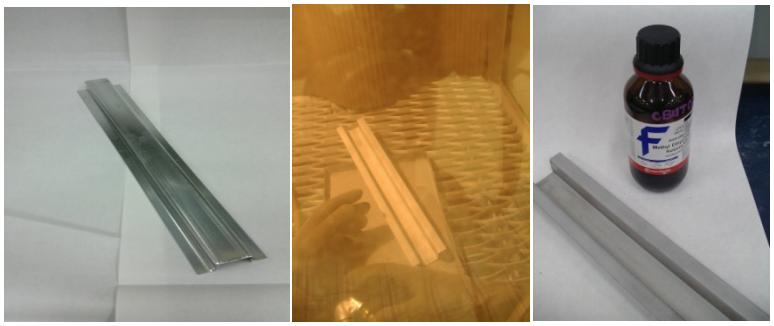

Figure A 1: Sample preparation

2. Application of the adhesive:

    Spacers made out of thin gage sheet steel are used to ensure uniformity of the bond thickness. One spacer is laid across the top end of each hat, such that it spanned the

mating surfaces (Figure A2). A second spacer is installed, running perpendicular to the surface on the inside of the hats. Both sets are required to avoid spills and obtain consistent bonds in the tube.

a. Install spacers, and apply adhesive to one of the surfaces

b. Join the two sections and press together. Clean away any extra material that spills out following compression.

c. Use butterfly clips to secure the two sections together

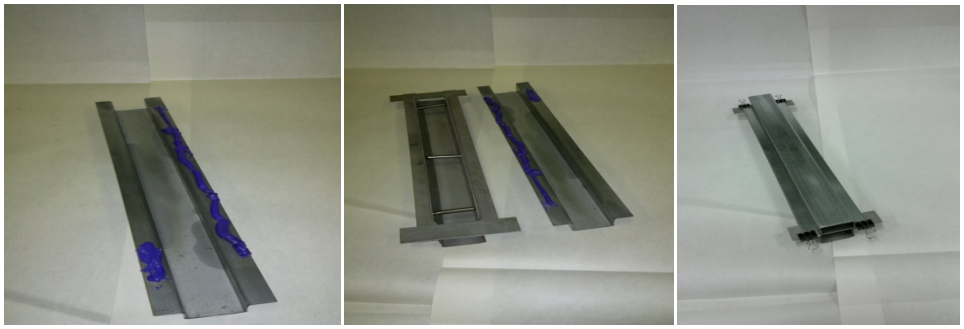

Figure A 2: Adhesive application and joining

3. Cure the assembly in an oven, setting the temperature according to the requirements of the specific adhesive used.

    a. Preheat the oven prior to introducing the sections (takes roughly 2 hours).

    b. Some adhesive materials will leak from the section. To avoid damaging the oven, wrap the sections in heavy aluminum foil (barbeque or heavy bake commercial aluminum foil available in any supermarket or grocery store) and place them on a tray.

    c. Remove from oven and allow sections to cool at ambient temperature, leaving sections wrapped in aluminum foil.

Figure A 3: Oven curing

4. Cutting and indenting:

    a. Once at room temperature, the bonded section can be cut to length and indented with a buckle initiator, as shown in Figure A4.

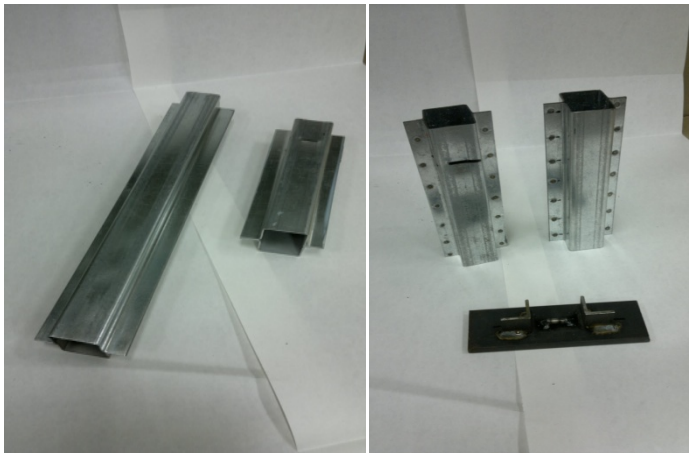

Figure A 4: Sample cutting and indenting

5. Paint samples if required. Samples used in the drop tower were painted with a speckle pattern, as shown in Figure A5, to allow strain analysis of the video footage using digital image correlation (DIC) software.

Figure A 5: Paint job for DIC system

Appendix B

Damage initiation (τ) curve fitting

In order to determine the strength of an adhesive joint constrained by two identical materials, a non linear model was used to fit the DCB test data presented by Kafkalidis [22] to a suitable expression derived by using principles of non-dimensional analysis. Kafkalidis' data is presented in Table B1.

Adhesive layer thickness [mm]	Adherent layer thickness [mm]	Adhesive E[GPa]	Adherent E [GPA]	Adhesive Yield stress [MPa]	Peak stress [MPa]
0.14	3	3.1	70	50	140
0.14	1.3	3.1	70	50	115
0.25	3	3.1	70	50	100
0.25	2	3.1	70	50	95
1	1.3	3.1	70	50	85
0.25	3	3.1	70	50	85
0.25	1.4	3.1	210	50	105
0.25	0.9	3.1	210	50	90
0.25	0.7	3.1	210	50	85
0.14	3	1.45	70	25	120
0.14	2	1.45	70	25	115
0.25	3	1.45	70	25	95
0.25	2	1.45	70	25	80

Table B 1: Kafkalidis data for DCB test of adhesive joints

As it was just mention, the form of the function selected to fit the data was generated using dimensional analysis, this approach allows true physical relationships to be incorporated among the variables. The data was described in terms of the following variables:

$$\tau = f(\sigma_y, E_1, E_2, t_1, t_2)$$

where t represents the thickness of the materials and E is the modulus of elasticity. The numbers 1 and 2 refer to the adherents and adhesive, respectively. For this problem, the data is described in terms of 6 variables, so 3 Π numbers are possible.

$$\frac{\tau}{\sigma_y} = f\left(\frac{E_1}{\sigma_y}, \frac{E_2}{\sigma_y}, \frac{t_1}{t_2}\right)$$

Using Mathematica numerical code, a non-linear fit to the data was performed with the following result:

$$\tau = \frac{7.95\text{x}10^{-11}\left(\frac{E_l}{\sigma_y}\right)^{0.069}\sigma_y}{\left(\frac{t_l}{t_{ad}}\right)^{0.21}\left(\frac{E_{ad}}{\sigma_y}\right)^{8.45}}$$

For the previous non-linear fit an ANOVA table (Table B-2) was created to verify the quality of the fit.

	DF	SS	MS
Model	4	133955	33488.8
Error	9	1744.83	193.87
Uncorrected total	13	135700	
Corrected total	12	3692.31	

Table B 2:Non-linear model ANOVA table

The model response shown in Figure B 1 follows Kafkalidis' data very closely. It should also be noted that the standardized residuals, shown in Figure B2, do not show noticeable trends, but rather seem to be random.

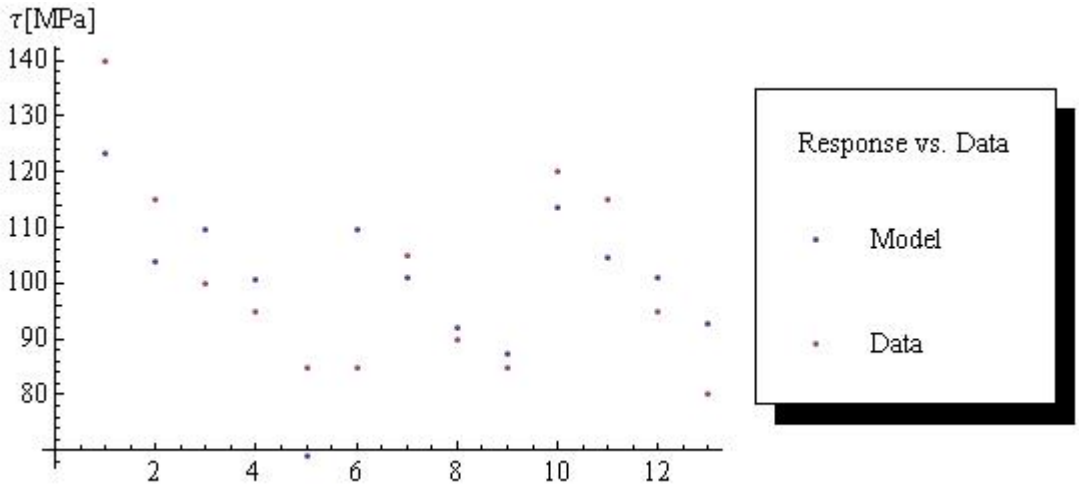

Figure B 1: Model response

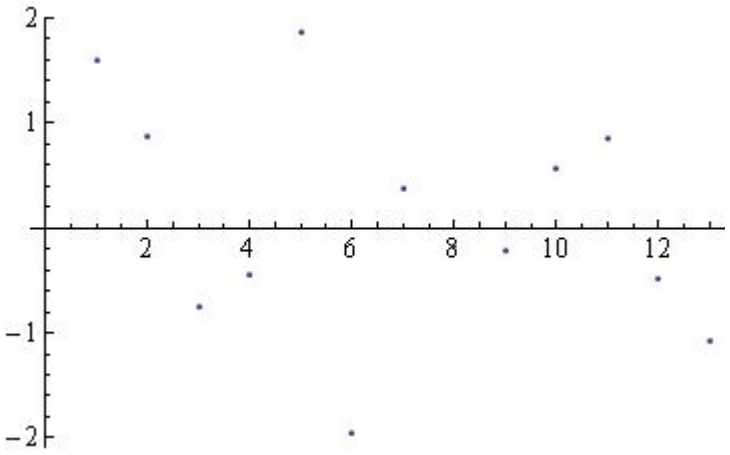

Figure B 2: Model standardized residuals

Although there is good agreement between the data and the proposed model, an F-test was used to determine the relevance of the model.

$$F_{obs} = \frac{MS_{model}}{MS_{error}}$$

$If\ F_{4,9,0.05} > F_{obs}$, the model is not relevant

$$3.63 > 172.73$$

The model is highly significant according to this test.

Appendix C
Convergence analysis

In order to use numerical analysis as a predictive tool, one has to be sure that the model used to describe the intended problem can provide accurate and reliable answers under the required load conditions. A typical procedure for computer models is to determine if the discretization of the problem, i.e. mesh size, is adequate and provides accurate answers; this is typically done using convergence analysis, where the mesh size for a given problem is varied and an output parameter of the simulation is monitored. Once the solution is stable, the problem is thought to have converged and the mesh size selected is considered adequate enough to describe the problem. Both the DCB model and the crush tube model were subjected to convergence analysis.

C.1 DCB model

The DCB model, as described in Section 2.5 in the main body of this work, was subjected to a convergence analysis by varying the element size that described both the adhesive material and the body of the beam. To identify convergence, two parameters were monitored against element size. Four different cohesive element sizes were considered, 15, 6.5, 2.5 and 1mm. The thickness of the element representing the adhesive material was kept constant at 1mm.

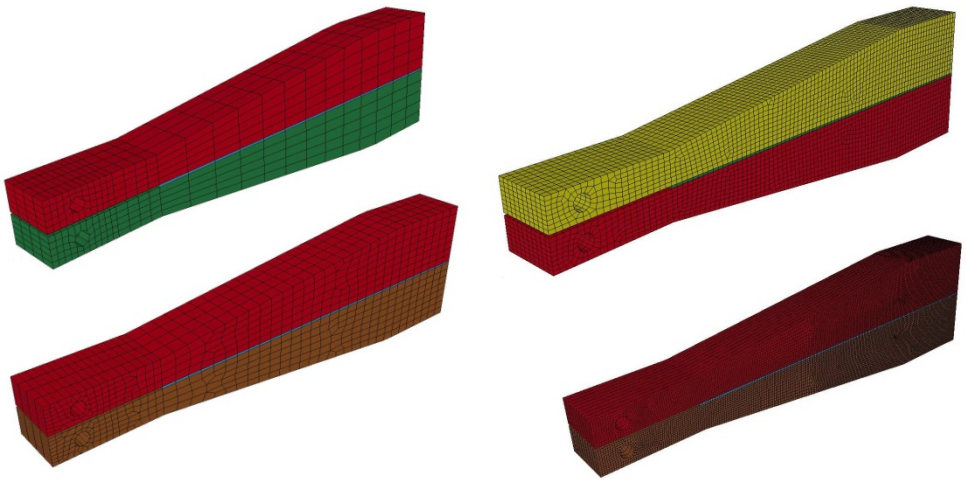

Figure C 1: Mesh discretization for DCB model: 15 mm (top left), 6.5 mm (bottom left), 2 mm (top right), and 1mm (bottom right)

First, the resultant load displacement diagrams were compared.

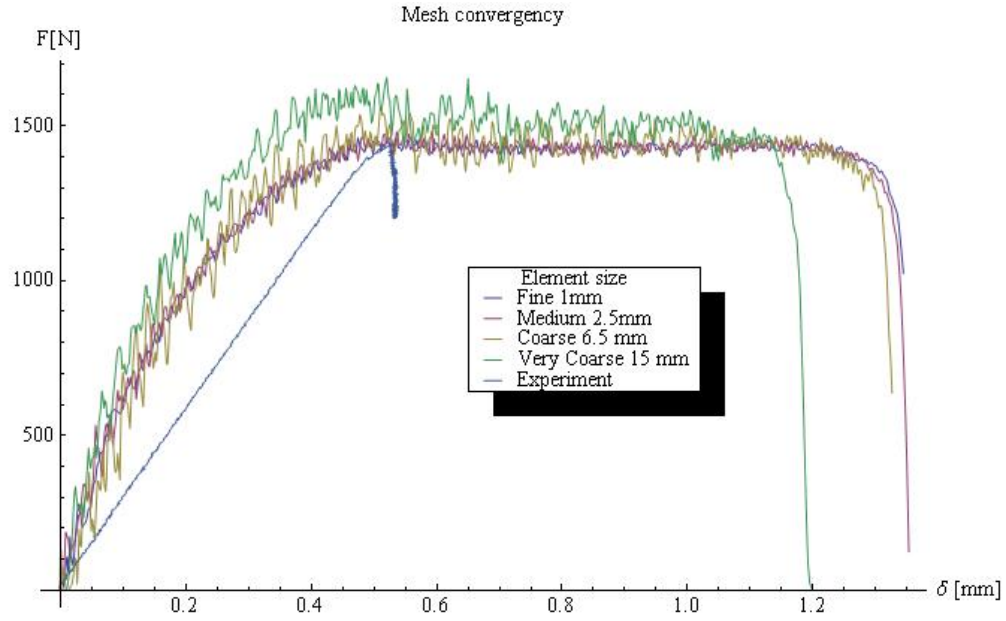

Figure C 2: Load-displacement dependency with element size

Second, the fracture toughness of the adhesive material (K_{IC}) was calculated from the load-displacement results, and the results plotted against element size. The experimental data was used for verification.

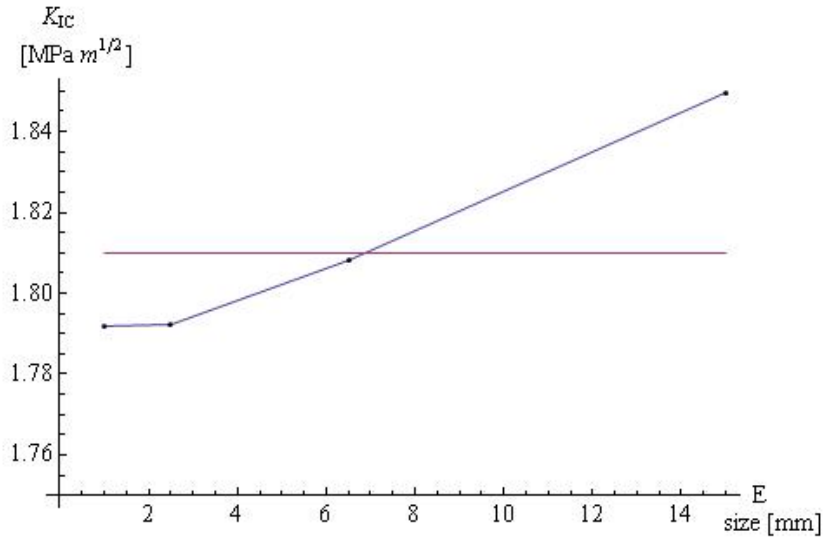

Figure C 3: Calculated K_{IC} from DCB model with mesh size dependency

C.2 Crush tubes

Other authors have previously studied crush tubes under axial impact load. For example, Langseth [27, 28]and Tarigopula [40] studied square and welded top hat sections made out of aluminum or steel, and Williams [46] analyzed the numerical model response for hydro-formed aluminum round tubing.

For this work, a square section experiment was first used to determine the main mesh size necessary to accurately describe the problem. This knowledge was then applied to the analysis of adhesively bonded structures.

The present analysis explored the effects of mesh size and the number of integration points used in the shell element on the numerical simulation response. Furthermore, a standard material model available in the LS-DYNA code was selected to describe the properties of the base material – as opposed to using a custom material code.

This experiment is analogous to work already done by Tarigopula [40]; thus his results, both experimental and numerical, were used for validation.

C.2.1 Experiment description

A square tube, 60 mm (width) x 1.18 mm (thickness) x 410 mm (length), was subjected to an axial impact of a 600 kg mass moving at 15 m/s. The lower 100 mm of the tube is fully constrained except for the longitudinal translation to match the experimental set-up described in [40]. The striking hammer was not described in this work, so a plane rigid surface was used as the striker.

C.2.1.1 Material and material model

The material model used to simulate this experiment is described in Section 3.2.2.

C.2.2 Numerical convergence

For numerical efficiency, automotive mesh sizes typically stay within the order of 3mm square elements; however, Langseth [28] and Tarigopula [40] have shown good agreement between experimental and numerical simulation results using squares as small as 3 mm. Therefore, a comparison is required to establish the effect of mesh size on the quality of the results.

The mesh size was varied, starting from a very coarse mesh of 10mm. In descending order, 10, 8, 5, 4, 3, 2, and 1 mm squares were used.

For this set of simulations all elements had 5 integration points across the shell thickness for the solution. Any effect the number of integration points may have had on the simulation response was also explored.

The convergence analysis is presented as a series of diagrams showing the results obtained for each mesh size compared to both the experimental data and equivalent simulation results presented by Tarigopula et al[40] .

C.2.2.1 Effects of filtering

The impact of the filtering frequency was analyzed using simulation results based on a 3mm mesh size. A sampling of 500 Hz was compared to a 2500 Hz filter using the SAE option available in the LS-DYNA pre-post software.

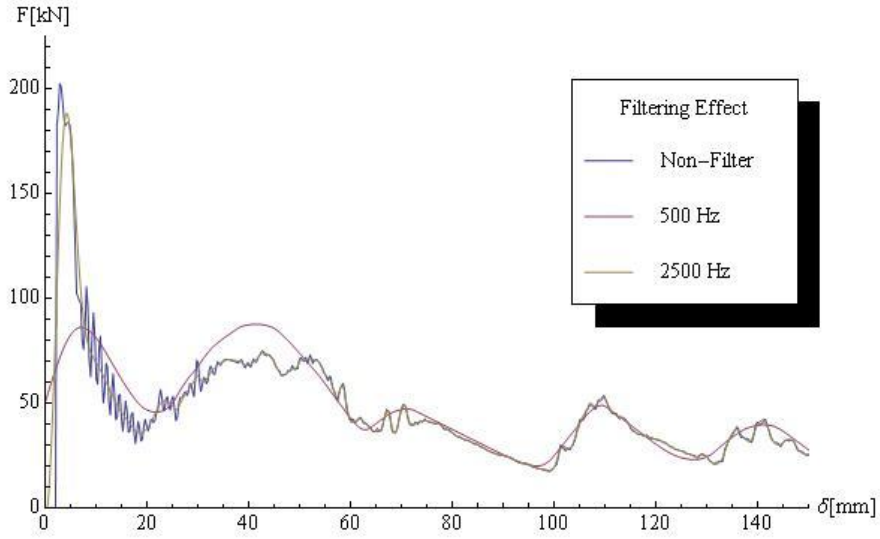

Figure C 4: Effects of filtering

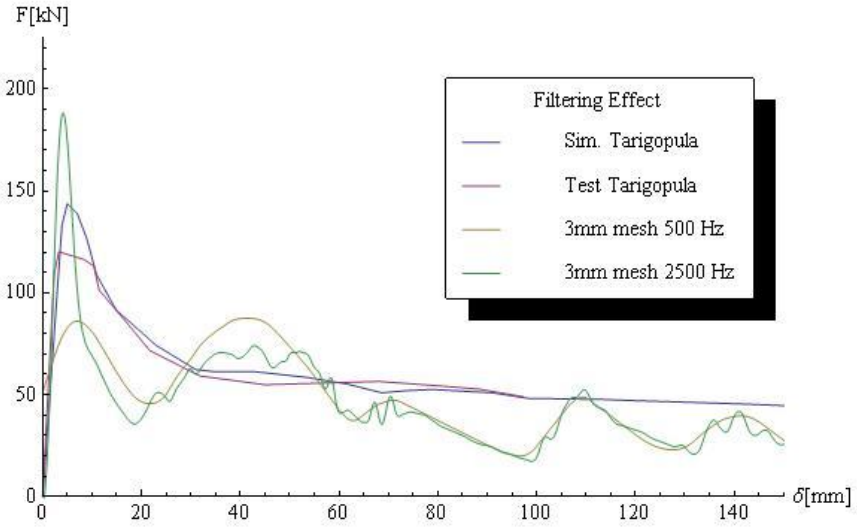

Figure C 5: Filtered response vs. literature results

The effect filtering may have had on the calculated absorbed energy was also explored, shown in Figure C6.

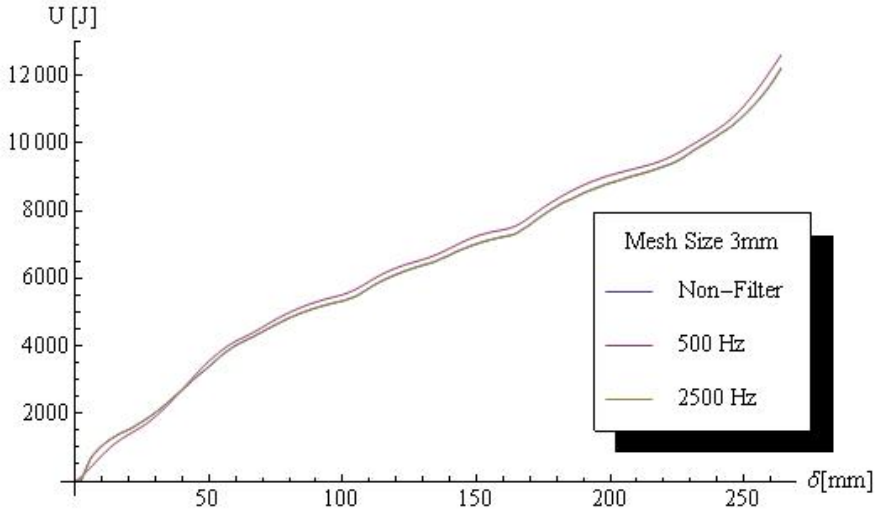

Figure C 6: Effects of filtering in absorbed energy results

If results from LS-DYNA simulations for this type of events were to be filtered; the2500 Hz using the SAE option available in the LS-DYNA pre-post software is the best option sincethis frequency substantially reduced the noise without omitting the maximum peak force.

C.2.2.2 The effects of mesh size

The size of the element selected to discretize the domain has a big impact in the quality of the results. In order to explore such effects a series of studies were done by changing the element size for a given geometry, loads and boundary conditions. Load vs. axial displacement and energy vs. displacement diagrams are presented for each case of element size. Further analysis was carried out to explore energy absorption, specific energy absorption and mean force for each condition. Results from numerical simulation were compared against the data presented by Tarigopula.[40]

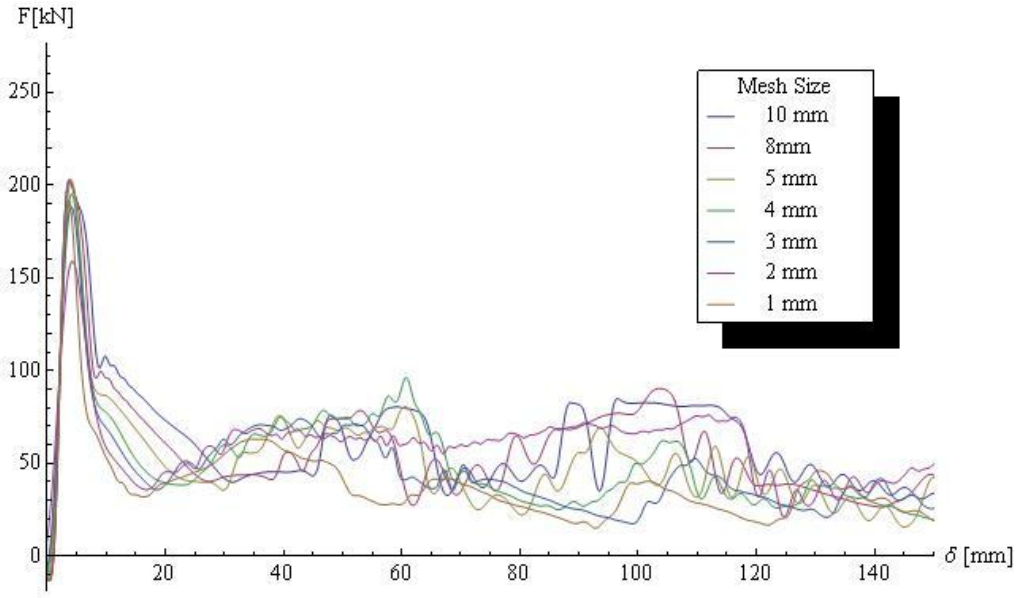

Figure C 7: Simulation response with different mesh sizes

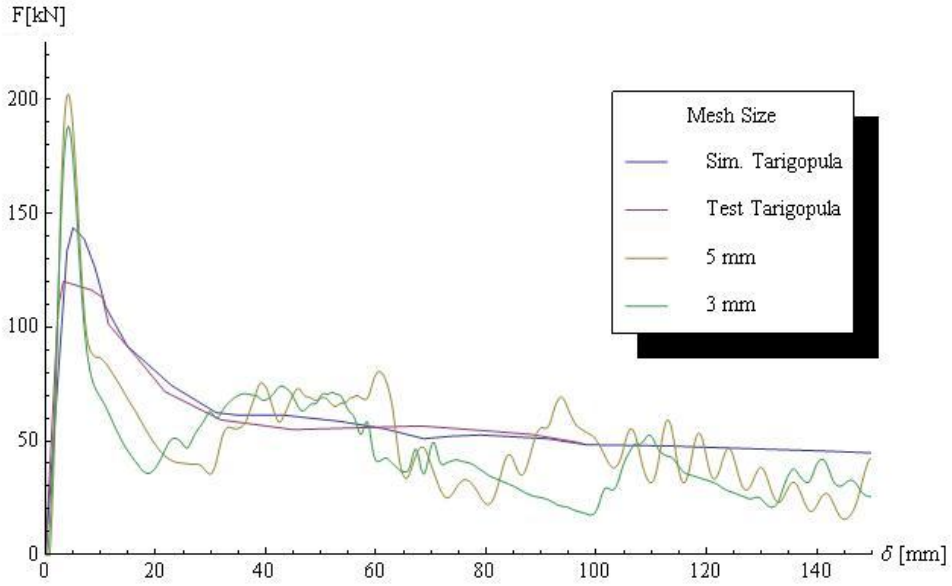

Figure C 8: Simulation mesh effects vs. author results

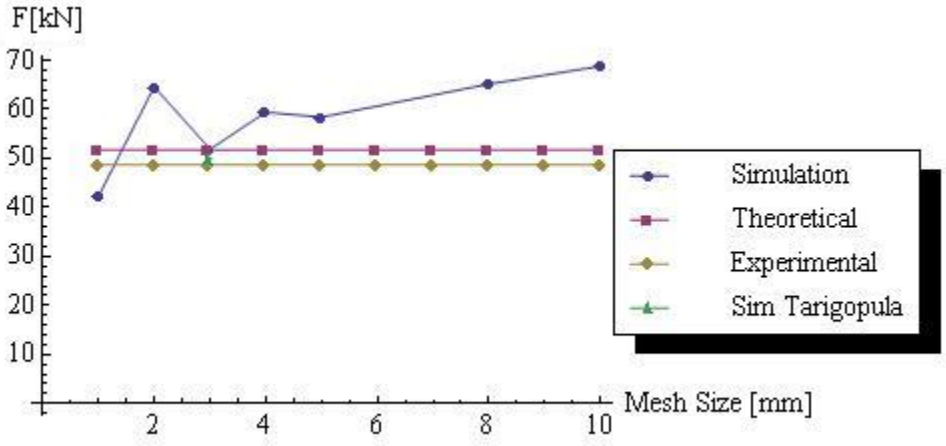

Figure C 9: Mesh size vs. mean force

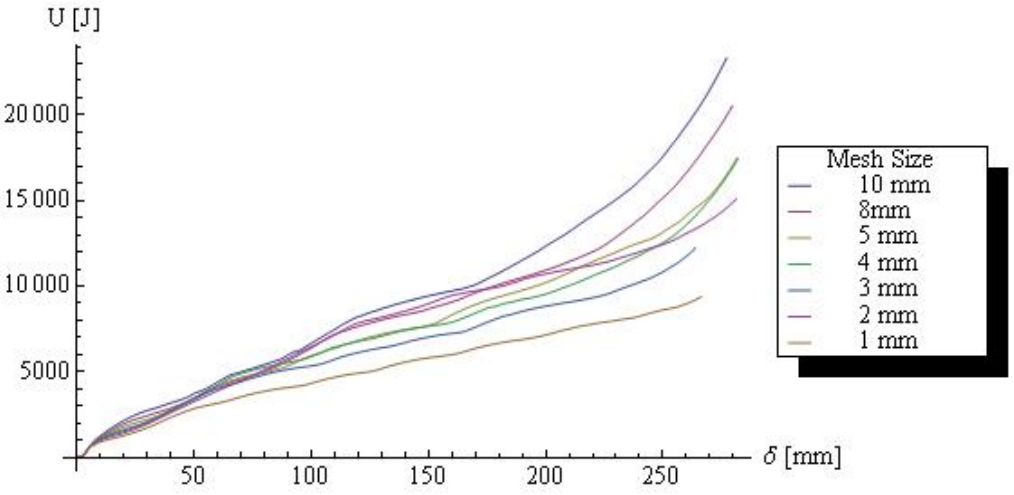

Figure C 10: Mesh size effects on the energy absorption

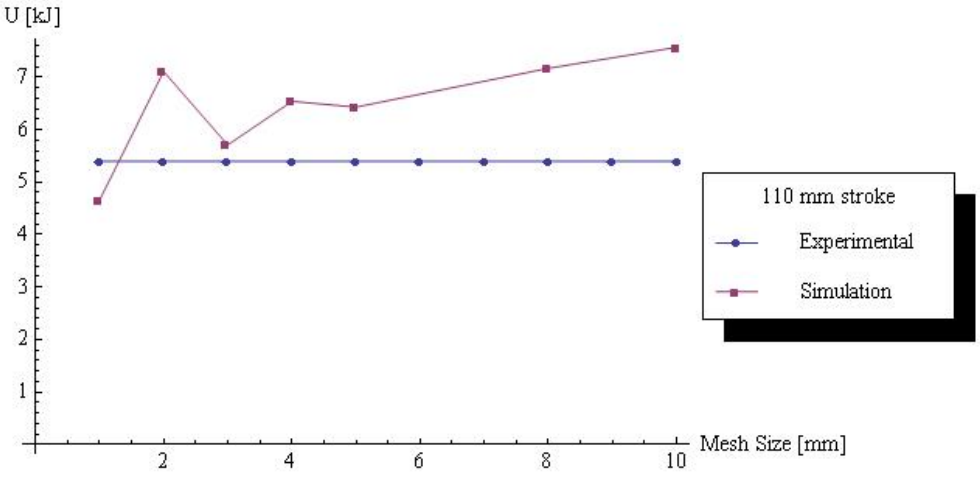

Figure C 11: Energy absorbed vs. mesh size

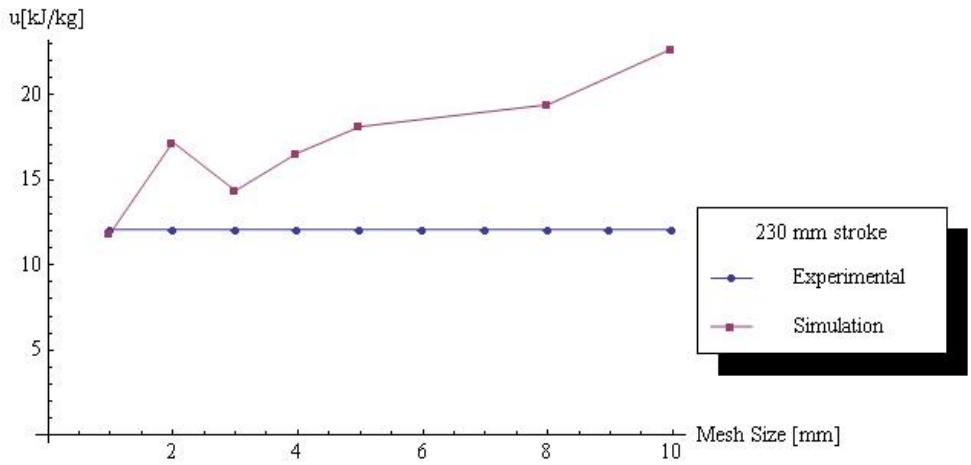

Figure C 12: Specific energy absorbed vs. mesh size

C.2.2.3 The effects of number of integration points

The number of integration points defines the quality of the results in the case of shell elements; more points translate into a better capability of the element to capture the gradient of stresses across the thickness. The impact of number of integration points across the shell element was investigated using a model with a fixed mesh size of 3 mm.

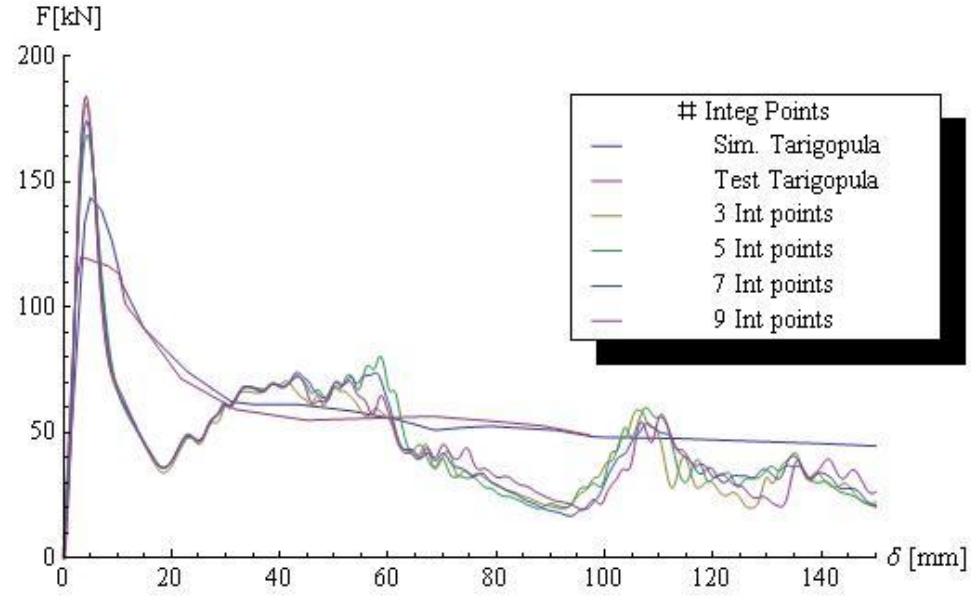

Figure C 13: Effect of number of integration points on the response

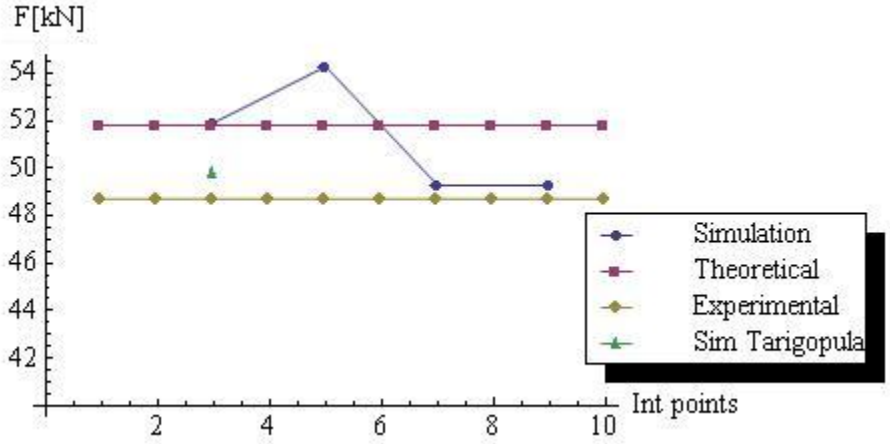

Figure C 14: Number of integration points vs. mean force

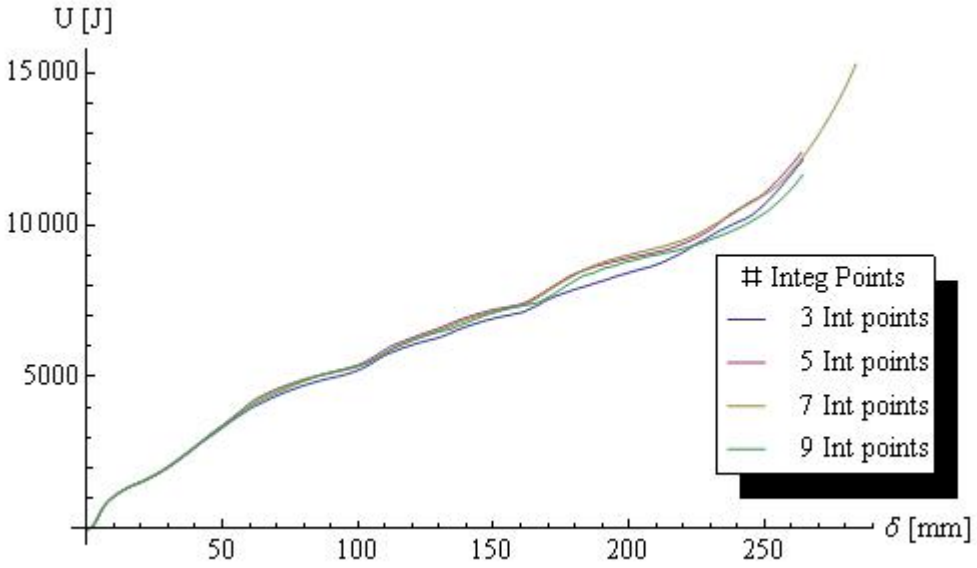

Figure C 15: Number of integration points effects on the energy absorption

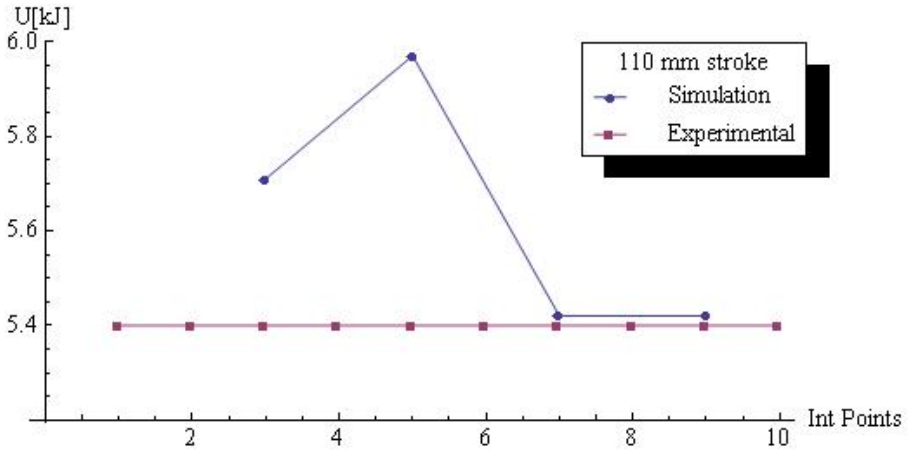

Figure C 16: Number of integration points effects vs. energy absorption

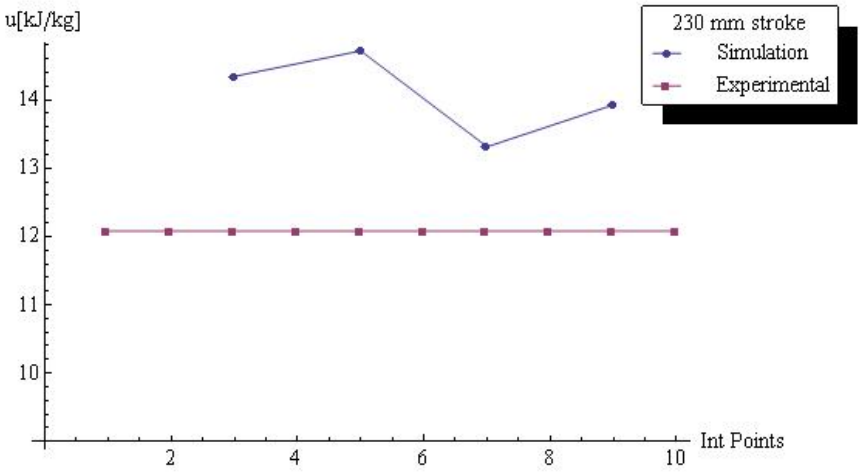

Figure C 17: Number of integration points effects vs. specific energy

C.2.2.4 Computational time

Solution time is critically important. Results presented here reflect parallel computation times using 4 CPUs.

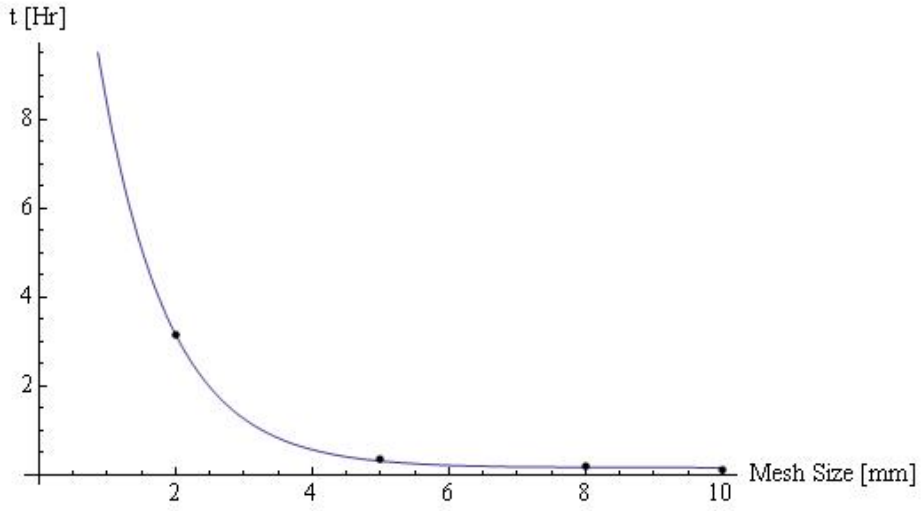

Figure C 18: Effect on computational time due to mesh size

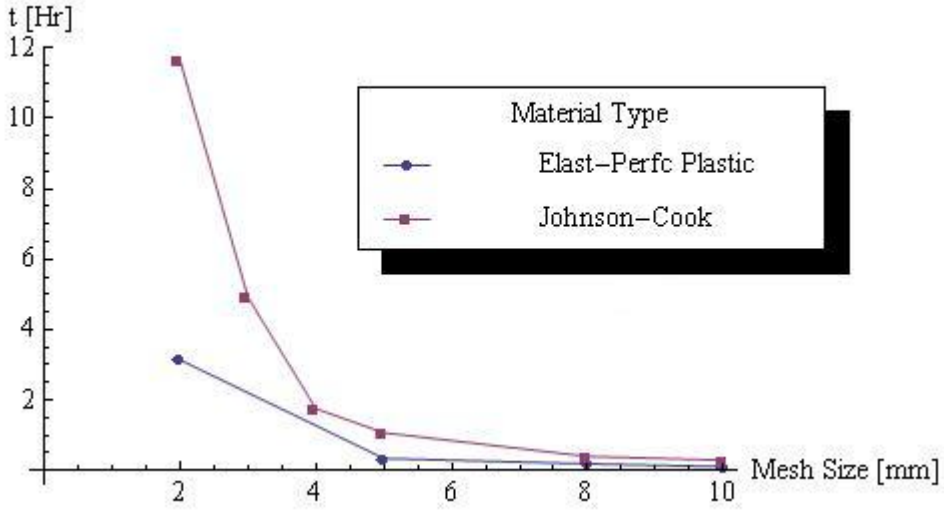

Figure C 19: Effect on computational time due to material model and mesh size

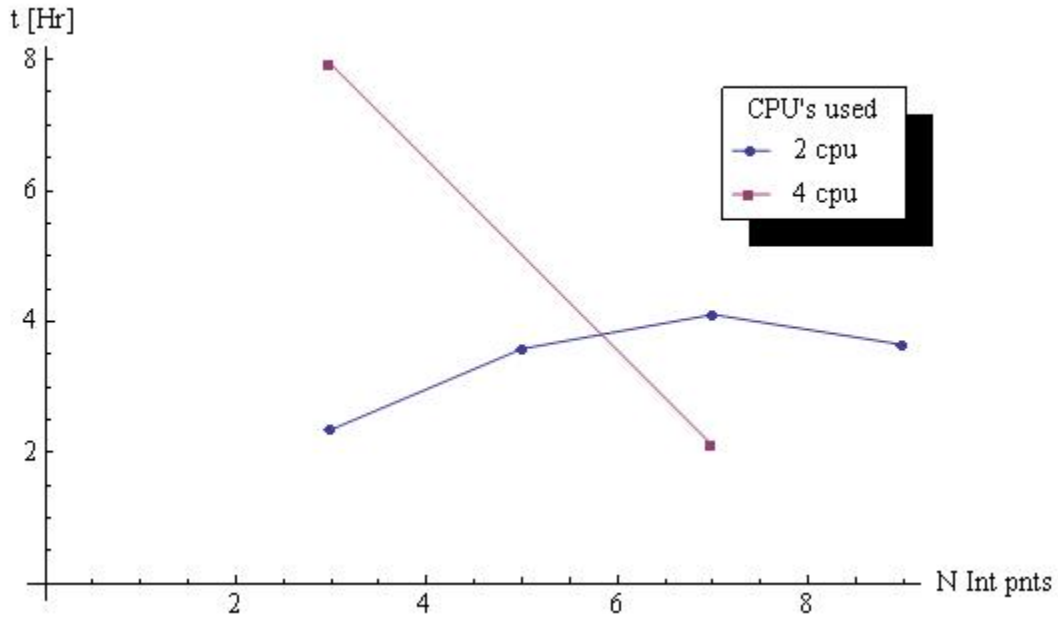

Figure C 20: Effect of number of processors on the solution time

Appendix D

LS-DYNA cards

D.1 Cohesive material cards

The following provides the cohesive element card definition for the LS-DYNA software used for epoxy materials

D.1.1 DP-460NS

```
*KEYWORD
$ Units
$mm/s/tonne/N
*MAT_COHESIVE_GENERAL
$MID, RO, ROFLG, INTFAIL ,TES, TSLC, GIC, GIIC
2, 1.250E-9,   0,      1,     0, 1000, 2.82061, 3.133205
$XMU, T, S, STFSF
1, 37.57, 20.67, 0
*DEFINE_CURVE
$
1000, ,2.2
$ Use a 2.2 correction factor to account for difference in thickness of adhesive bond between
$ experiment and simulation
$
0.00,0.00
0.03,0.73
0.05,0.87
0.07,0.93
0.09,0.97
0.11,0.98
0.22,1.00
0.35,1.00
0.47,0.98
0.55,0.96
```

0.58,0.92

0.61,0.85

0.64,0.73

0.66,0.62

1.00,0.00

*END

D.1.2 EC-2214

*KEYWORD

$ Units

$mm/s/tonne/N

*MAT_COHESIVE_GENERAL

$MID, RO, ROFLG, INTFAIL ,TES, TSLC, GIC, GIIC

2, 1.540E-9, 0, 1, 0, 1000, 0.65, 2.56

$XMU, T, S, STFSF

1, 10, 5, 0

*DEFINE_CURVE

1000

0, 0

0.017, 1

1, 0

*END

D.2 Tie break material cards

Tie-break card definition for the LS-DYNA software for DP-460NS epoxy material.

D.2.1 Tie-break formulation #1

Uses the option 8 to define the tie-break

*KEYWORD

$ Units

$mm/s/tonne/N

$Using DP-460NS, Sy= 36 MPA, shear stress defined as half of that value

```
$
*CONTACT_AUTOMATIC_ONE_WAY_SURFACE_TO_SURFACE_TIEBREAK
1,3,3,3,

8,36,18,0.1
$
*END
```

D.2.2 Tie-break formulation #2

Uses the option 9 to define the tie-breaks

```
*KEYWORD
$ Units
$mm/s/tonne/N
$
$Using DP-460NS
$
*CONTACT_AUTOMATIC_ONE_WAY_SURFACE_TO_SURFACE_TIEBREAK
1, 3, 3, 3
$ FS     FD       DC       VC       VDC
0.2, 0.2, , , 20
$ SFS    SFM              SST

$Option          NFLS   SFLS   param   eraten   erates   ct2cn    cn
9, 37.57, 20.67, 1, 2.82, 3.13
$ Optional Card A
$          Soft
$1
*END
```

D.3 Steel Material

D.3.1 Curve fit #1

```
*KEYWORD
```

```
$ Units
$mm/s/tonne/N
*MAT_PIECEWISE_LINEAR_PLASTICITY
$  mid  ro    E   pr    sigy   ETAN  FAIL TDEL
1,7.850E-9,207.0e3, 0.3, 367.2,
$
$
$ C   P  LCSS  lCSR  VP
$ curve fit using only peaks fo uniaxial testing for yield points
306.313,3.61,0,0,1 $
$ EPS1, EPS2, ...
0.0, 0.01234, 0.0248, 0.04966, 0.06208, 0.07650, 0.13859, 0.23376
$ ES1, ES2, ...
361.82, 359.31, 365.88, 392.58, 412.13, 430.71, 488.20, 547.14
*END
```

D.3.2 Curve fit #2

```
*KEYWORD
*MAT_PIECEWISE_LINEAR_PLASTICITY
$  mid  ro    E   pr    sigy   ETAN  FAIL TDEL
1,7.850E-9,207.0e3, 0.3, 367.2,
$
$
$ C   P  LCSS  lCSR  VP
$ curve fit values using all data and disregarding the peaks
77241, 4.9, 1,0,1
$ EPS1, EPS2, ...
0.0, 0.01234, 0.0248, 0.04966, 0.06208, 0.07650, 0.13859, 0.23376
$ ES1, ES2, ...
361.82, 359.31, 365.88, 392.58, 412.13, 430.71, 488.20, 547.14
$
*END
```

D.3.3 Curve fit #3

```
*KEYWORD
*MAT_PIECEWISE_LINEAR_PLASTICITY
$  mid  ro    E   pr   sigy   ETAN  FAIL TDEL
1,7.850E-9,207.0e3, 0.3, 367.2,
$
$
$ C   P  LCSS  lCSR  VP

$ EPS1, EPS2, ...

$ ES1, ES2, ...

$
$tables build using the plastic data
*DEFINE_TABLE
1
$ card 2
0.0016
10
100
1000
$ Curve QS
*DEFINE_CURVE
2
$ data from QS test specimen # 1
0.0, 361.82
0.01234, 359.31
0.0248, 365.88
0.04966, 392.58
0.06208, 412.13
0.07650, 430.71
```

0.13859, 488.20
0.23376, 547.14
$Curve 10 1/s
*DEFINE_CURVE
3
$ data from specimen # 1 Jan 18 2011
0.0, 496.2
0.0119, 446.79
0.024728, 504.03
0.04917, 481.68
0.06165, 482.18
0.0760552, 499.13
0.13795, 565.61
0.2329, 625.29
$curve 100 1/s
*DEFINE_CURVE
4
$ data from specimen # 1 jan 28-2011
0.0, 627.13
0.01113, 618.03
0.0240623, 520.94
0.04902, 517.82
0.06143, 529.76
0.07582, 546.77
0.137801, 598.65
0.2328, 644.53
$curve 10001/s extrapolation from base curve using curve fit disregarding peaks
*DEFINE_CURVE
5
0.0, 885.61
0.05147, 960.904
0.063956, 1008.74

0.078432, 1054.24

0.140652, 1194.94

0.235878, 1339.21

$

$

*END

Bibliography

[1] Anonymous ESC Report
History of Adhesives (1991).

[2] Anonymous Metals handbook, Mechanical testing, American Society for Metals, Metals Park, Ohio, 1989.

[3] W. Abramowicz and N. Jones, Transition from initial global bending to progressive buckling of tubes loaded statically and dynamically, Int. J. Impact Eng. 5-6 (1997), 415-437.

[4] W. Abramowicz and N. Jones, Dynamic axial crushing of square tubes, Int. J. Impact Eng. 2 (1984), 179-208.

[5] M. Alves, Material constitutive law for large strains and strain rates, J. Eng. Mech. 2 (2000), 215-218.

[6] Anonymous, Lotus Elise wikipedia webpage.

[7] G. Belingardi, L. Goglio and M. Rossetto, Impact behaviour of bonded built-up beams: experimental results, Int J Adhes Adhes 2 (2005), 173-180.

[8] M.L. Benzeggagh and M. Kenane, Measurement of mixed-mode delamination fracture toughness of unidirectional glass/epoxy composites with mixed-mode bending apparatus, Composites Sci. Technol. 4 (1996), 439-449.

[9] T.Z. Blazynski, Materials at high strain rates, Elsevier Applied Science, London, 1987.

[10] D.M. Bruce , D.K. Matlock , J.G. Speer and A.K. De , Assessment of the Strain-Rate Dependent Tensile Properties of Automotive Sheet Steels.

[11] K.D. Clarke, R.J. Comstock, M.C. Mataya, C.J. Tyne and D.K. Matlock, Effect of strain rate on the yield stress of ferritic stainless steels, Metall Mat Trans A Phys Metall Mat Sci 4 (2008), 752-762.

[12] R. Collingridge, Lotus Elise enthusiast webpage.

[13] G.R. Cowper and P.S. Symonds, Strain hardening and strain-rate effects in the impact loading of cantilever beams, Brown University Division of Applied Mathematics (1957).

[14] A.D. Crocombe, D.A. Bigwood and G. Richardson, Analysing structural adhesive joints for failure, Int J Adhes Adhes 3 (1990), 167-178.

[15] D.A. Dillard and A.V. Pocius, eds., Adhesion science and engineering, The mechanics of adhesion, Elsevier, Amsterdam ; Boston, 2002.

[16] P.A. Fay and G.D. Suthurst, Redesign of adhesively bonded box beam sections for improved impact performance, Int J Adhes Adhes 3 (1990), 128-138.

[17] W. Goldsmith, Impact, the theory and physical behaviour of colliding solids, Dober publications, New York, 2001.

[18] J.A. Harris and R.D. Adams, Strength prediction of bonded single lap joints by non-linear finite element methods, Int J Adhes Adhes 2 (1984), 65-78.

[19] M. Itabashi and K. Kawata, Carbon content effect on high-strain-rate tensile properties for carbon steels, Int. J. Impact Eng. 2 (2000), 117-131.

[20] G.R. Johnson and W.H. Cook, Fracture characteristics of three metals subjected to various strains, strain rates, temperatures and pressures, Eng. Fract. Mech. 1 (1985), 31-48.

[21] N. Jones, Structural impact, Cambridge University Press, Cambridge, 1989.

[22] M.S. Kafkalidis, M.D. Thouless, Q.D. Yang and S.M. Ward, Deformation and fracture of adhesive layers constrained by plastically-deforming adherends, J. Adhes. Sci. Technol. 13 (2000), 1593-1607.

[23] D. Karagiozova and M. Alves, Dynamic elastic-plastic buckling of structural elements: a review, Applied Mechanics Review 4 (2008), 040803-1.

[24] A.J. Kinloch, Fracture behaviour of polymers, Applied Science Publishers, London, 1983.

[25] A. Kochan, Lotus: aluminium extrusions and adhesives, Assem. Autom. 4 (1996), 19-21.

[26] S. Krenk, Mechanics and analysis of beams, columns and cables : a modern introduction to the classic theories, Springer, Berlin ; New York, 2001.

[27] M. Langseth and O.S. Hopperstad, Static and dynamic axial crushing of square thin-walled aluminium extrusions, Int. J. Impact Eng. 7-8 (1996), 949-968.

[28] M. Langseth, O.S. Hopperstad and T. Berstad, Crashworthiness of aluminum extrusions: Validation of numerical simulation, effect of mass ratio and impact velocity, Int. J. Impact Eng. 9 (1999), 829-854.

[29] Livermore software technology corporation (LSTC), LS-DYNA Keyword user manual Material Models
Version 971, Livermore software technology corporation (LSTC), 2007.

[30] Livermore software technology corporation (LSTC), LS-DYNA Keyword user manual Version 971, Livermore software technology corporation (LSTC), 2007.

[31] J. Marsolek and H.-. Reimerdes, Energy absorption of metallic cylindrical shells with induced non-axisymmetric folding patterns 8-9 (2004), 1209-1223.

[32] Martins da Silva, L. F. and A. Ochsner, eds., Modleing of adhesively bonded joints, Springer, Berlin, 2008.

[33] I.U. Ojalvo and H.L. Eidinoff, Bond thickness effects upon stresses in a single-lap adhesive joints, AIAA J. 3 (1978), 204-211.

[34] R.E. Oshiro and M. Alves, Scaling impacted structures, Arch Appl Mech 1-2 (2004), 130-45.

[35] R.E. Oshiro and M. Alves, Scaling of structures subject to impact loads when using a power law constitutive equation, Int. J. Solids Structures 18-19 (2009), 3412-3421.

[36] R.E. Oshiro and M. Alves, Scaling of cylindrical shells under axial impact, Int. J. Impact Eng. 1 (2007), 89-103.

[37] L. Peroni and M. Avalle, Experimental investigation of the energy absorption capability of bonded crash boxes (2006), 445-454.

[38] P. Prasad and J.E. Belwafa, eds., Vehicle crashworthiness and occupant protection, American Iron and steel institute, Michigan, 2004.

[39] N.M. Rahman, A. Mian and G.M. Newaz, Analysis and characterization of adhesively bonded Mg-steel lap joints (2004), 129-135.

[40] V. Tarigopula, M. Langseth, O.S. Hopperstad and A.H. Clausen, Axial crushing of thin-walled high-strength steel sections, International Journal of Impact Engineering 5 (2006), 847-882.

[41] A. Turon, C.G. Davila, P.P. Camanho and J. Costa, An engineering solution for mesh size effects in the simulation of delamination using cohesive zone models, Eng. Fract. Mech. 10 (2007), 1665-1682.

[42] V. Tvergaard and J.W. Hutchinson, Relation between crack growth resistance and fracture process parameters in elastic-plastic solids, J. Mech. Phys. Solids 6 (1992), 1377-1377.

[43] V. Tvergaard and J.W. Hutchinson, Toughness of ductile adhesive joints, J. Mech. Phys. Solids 5 (1996), 789-800.

[44] M.D. White and N. Jones, A theoretical analysis for the dynamic axial crushing of top-hat and double-hat thin-walled sections, Proceedings of the Institution of Mechanical Engineers.Part D, Journal of Automobile Engineering D4 (1999), 307-325.

[45] T. Wierzbicki and W. Abramowicz, On the crushing mechanics of thin-walled structures, Transactions of the ASME. Journal of Applied Mechanics 4 (1983), 727-34.

[46] B.W. Williams, A Study of the Axial Crush Response of Hydroformed Aluminum Alloy Tubes (2007).

[47] Q.D. Yang, M.D. Thouless and S.M. Ward, Numerical simulations of adhesively-bonded beams failing with extensive plastic deformation, J. Mech. Phys. Solids 6 (1999), 1337-1353.